MEDICAL IMAGING EQUIPMENT THEORY

Richard Aston

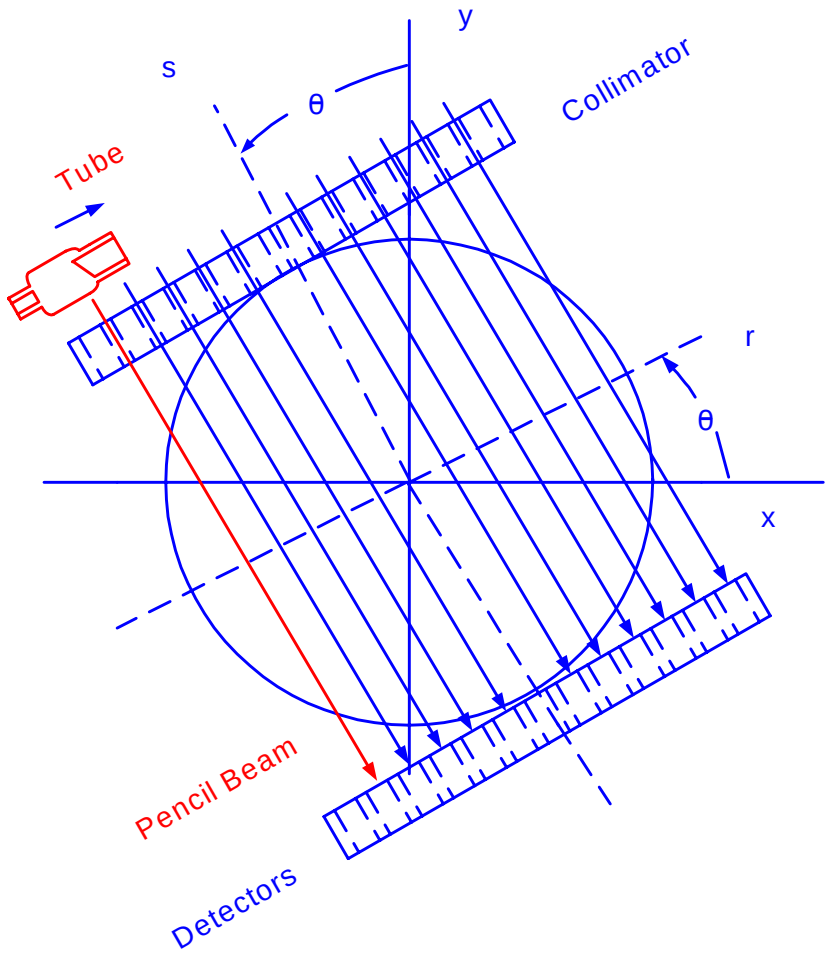

MEDICAL IMAGING EQUIPMENT THEORY

Richard Aston

ABC engineering research

33 Barney Street
Wilkes-Barre
Pennsylvania, U.S.A. 18702
(570)829-3163
E-mail: astonrj@yahoo.com
Web Site: <www.epix.net/~astonr>
or
<www.epix.net/~astonr/index.htm>

Copyright © 2004 by Richard Aston. All rights reserved. May not be copied or distributed without signed written permission of the author.
DISCLAIMER: This material is derived from the literature as indicated in the references. It is meant for educational purposes only. The author regrets any omissions, misunderstandings or errors and disclaims any liability for them, and disclaims responsibility for any implications these ideas might have for existing equipment, its design, use, or maintenance.

PREFACE

This book is meant to serve as educational materials for clinical and biomedical engineering and biomedical engineering technology students interested in understanding medical imaging equipment. It is directed at the senior/graduate level.

One basic question at the center of the work is, how is it that one can take a picture of a slice through the body with out opening the skin? A clear and systematic answer is given with the help of Fourier Transform mathematics, along with discussions of the physical principles of the hardware involved. This approach has great educational value because it is straight forward logic and gives the student a basis for designing and maintaining this equipment. However the Fourier Transform approach is not always used, and is often replaced with computer iteration and statistical techniques. A study of these computer algorithms is beyond the scope of the present work. Thus our focus here is more on the hardware than on the software of system analysis.

Classroom presentation materials such a slide show of the figures in the text along with concise explainations is provided on the author's web site:<www.epix.net/~astonr> or <www.epix.net/~astonr/index.htm>. Student end-of-chapter exercises and a solutions manual for instructors are available at ABC engineering research, 33 Barney St. Wilkes-Barre, PA, U.S.A. 18702. (astonrj@yahoo.com).

MEDICAL IMAGING EQUIPMENT THEORY

Richard Aston
June, 2005

TABLE OF CONTENTS

Chapter 1 **Magnetic Resonance Imaging (MRI) Equipment Theory** 1
Introduction 1
Nuclear Magnetic Resonance 2
RF Radiation 3
Inducing NMR 4
FID 6
Spin Echo 6
Magnetic Resonance Imaging 7
The DC Magnetic Coil 8
Field Shaping Coil in the Z-direction 9
Field Shaping in the X- and Y-directions 9
The Gantry 12
The Fourier Transform 13
The MRI Block Diagram 14
Signal Processing 18
Receiver Processing 19
Image Resolution 19
Signal-to-noise Ratio 20
Mathematical Model for Image Calculation 21
Hardware Data 22
RF Coils 25
Fast-Scan Techniques 26
References 29
Engineering Data from Vlaardingerbroek 31
Further Information on MRI from the WEB 31
Exercises

Chapter 2 **X-ray: Basic Theory** 34
X-ray Production 35
X-ray Tube Current 35
X-ray Characteristics 37

	Planar X-ray	39
	Image Production	40
	Mass Attenuation Coefficient	41
	X-ray Hardware	43
	X-ray Tube	44
	Beam Shaping Parts	47
	X-ray Detection	48
	The Power Supply	49
	References	50
	Exercises	50
Chapter 3	**CT Scanner Theory**	51
	CT Scanner	51
	CT Image Calculation	51
	Improving Scan Speed	55
	X-ray Detectors	56
	Gantry Hardware	57
	Fifth Generation CT Scanner	58
	Image Properties	58
	CT Scanner Calibration	60
	Resolution	60
	Patient Dose	61
	Spiral Scanners	63
	References	64
	More Information on CT Scanners from the WEB	64
	Exercises	66
Chapter 4	**Nuclear Medical Equipment: Part 1. Planar Imaging**	67
	Hydrogen and its Isotopes	67
	The Cyclotron	68
	Radioactivity	70
	Radio Nuclides	71
	Tracking Radio Pharmaceuticals	72
	Well Counter	72
	Anger Camera	73
	References	74
	Exercises	75
Chapter 5	**SPECT and PET Scanners**	76
	The SPECT Scanner	77
	The SPECT Algorithm	78

Advances in SPECT Scanning 80
Scintillating Crystals for Gamma Radiation 82
Attenuation Correction 83
The Positron Emission Tomography (PET) Scanner 83
Electronic Collimation 85
Collimation Errors 87
Axial Collimation 88
Detectors 89
Overview, Advances and Comparison of SPECT and PET Scanners 90
SPECT Scanner Advances 91
PET Scanner Advances 93
Troubleshooting 94
References 95
Exercises 96

Chapter 6 **Ultrasonic Imaging Equipment Theory** 97
Ultrasonic Waves 97
The Wave Equation 97
Solutions to the Wave Equation 100
Characteristic Impedance 103
Ultrasonic Wave Reflections 105
Power Reflection Coefficient 107
Power Transmission Coefficient 108
Power Attenuation 109
Power Relations at a Boundary 111
Ultrasonic Transducers 114
Impedance Matching 116
A-Scope Ultrasound Imaging 117
B-Scope Imaging 119
M-mode Display 119
Phased Array 120
References 121
Exercise 121

Appendix
Appendix A Magnetic Field of a Current Loop 122
Magnetic Field of a Solenoid 123
References 124
Appendix B Fourier Transform 125
Fourier Transform of a Pulse 126

	Inverse Fourier Transform of a Pulse	127
	Three Dimensional Fourier Transform	128
	References	129
Appendix C	Phase Shift Circuit	130
Appendix D	MRI fast scan technique	131
	References	134
Appendix E	Fan Beam Projection	135
About the Author		138

CHAPTER 1
MAGNETIC RESONANCE IMAGING EQUIPMENT THEORY

NOTE: This material is for educational purposes only. See the disclaimer above.

Introduction

Magnetic Resonance Imaging (MRI) equipment provides high quality two or three dimensional pictures of internal anatomical structures of the body without the need for performing surgery. It is comparable with Computer Tomography (CT) x-ray scans. It differs fundamentally from x-ray in its physics; it does not require ionizing radiation that presents a cancer risk, as does x-ray.

The MRI is based on the nuclear magnetic resonance (NMR) procedure, invented in 1946 by Felix Bloch, Edward Purcell, and coworkers, and used in the second half of the twentieth century to chemically analyze substances. In this procedure, a substance is placed in a strong DC magnetic field, then radiated with radio waves, often in the television band. The chemist can then identify the substance by measuring the frequency at which it absorbs the radio waves. In 1972, Raymond Damadian was issued a US Patent for showing how to detect cancer with NMR. The next year, Paul C. Lauterbur, a chemistry professor at the State University of New York at Stony Brook demonstrated that one could make a cross sectional image of the body using NMR [1.1]. It was immediately obvious that this

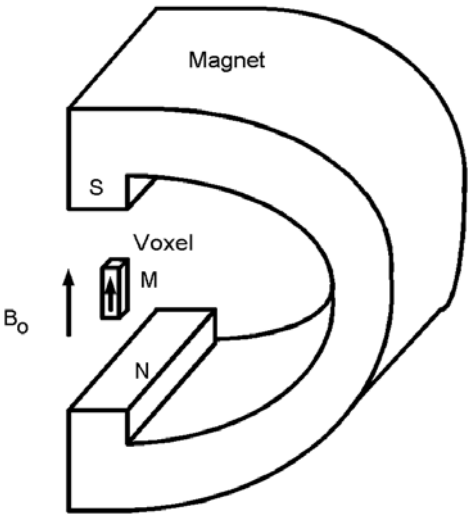

FIGURE 1.1. Voxel in a magnetic field.

technique was potentially valuable as a diagnostic tool in medicine. This no doubt produced the funding necessary to rapidly do the engineering development necessary to make this into a clinical tool.

Nuclear Magnetic Resonance

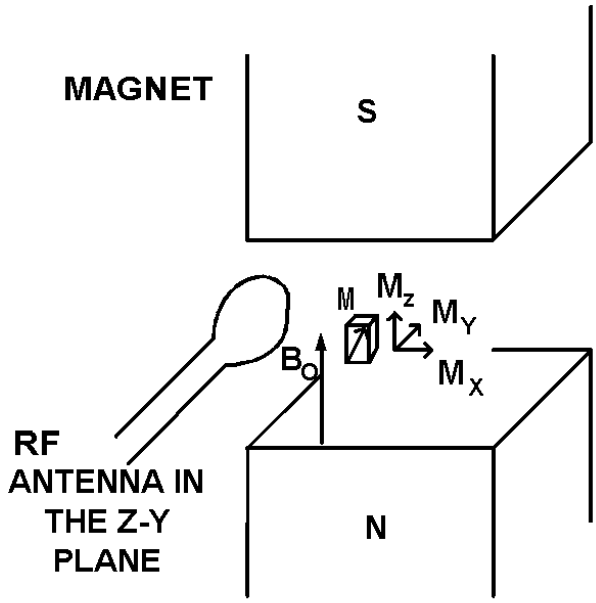

FIGURE 1.2. INDUCED PERTUBATION

Most atoms may be visualized as a spinning magnet. These magnets often have their north and south poles oriented randomly, yielding zero net magnetization. However when placed under a DC magnetic field, the magnets tend to orient so that a vector leaving their north pole lines up with the applied field lines, B_0, as shown in Figure 1.1, spinning on their axes, producing a magnetization, M, in a volume element (voxel).

Nuclear magnetic resonance occurs in each atom when radio frequency (RF) radiation, polarized perpendicular to B_0, is applied to the aligned atoms. Under the influence of both B_0 and RF, the axis of the magnetic moments of the aligned atoms shifts at an angle with B_0. It precesses around the direction of B_o like a gyroscope, as shown in Figure 1.2.

The frequency of the applied radiation, f, must be the value given by the Larmor equation

$$f = \gamma B_0 \qquad (1.1)$$

in order to cause precession of the atoms in the Figure 1.2 voxel, stimulated by RF. Here γ, the gyromagnetic ratio, is a measured quantity characterizing each atom and has units of hertz per Tesla

TABLE 1.1. Gyromagnetic Ratio Values.

Element	$\gamma^{(2)}$ (MHz/T)
1 H	42.58
31 P	17.25
23 Na	11.27
14 N	3.08
13 C	10.71

(Hz/T), f is in hertz, and B_0 in Tesla. The frequency of the RF depends on the type of atom. For the one most important in clinical MRI, hydrogen, the RF must be 42.58 MHz/Tesla. Thus if B_0 is 1.5 Tesla (T), the RF must be 63.87 MHz to cause precession of hydrogen atoms. Other gyromagnetic ratio values of clinical interest are [1.2] given in Table 1.1.

In practice, the RF is radiated by an antenna and polarized at right angles (orthogonal) to the direction of the DC magnetic field which is taken to be in the z-direction in a Cartesian coordinate system (x, y, z). The duration and magnitude of the RF is usually sufficient to orient the magnetic dipoles of the precessing atoms into the x-y plane, reducing the M_z component to zero.

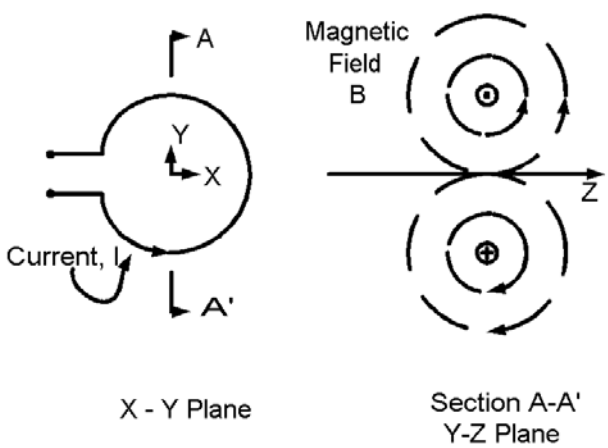

Figure 1.3. Fields of a loop antenna.

RF Radiation

One of the simplest antennas for radiating the RF is a single loop wire shown in Figure 1.3. Notice in the plane of the loop, the x - y plane in this case, the magnetic field generated by the loop is in the z-direction, designated B_z. The z-component of the field along a line through the center of the coil is derived in Appendix A as Equation (1.A4), and is given by, [1.3]

$$B_z = \frac{\mu_0 R^2 I}{2(R^2+Z^2)^{3/2}} \qquad (1.2)$$

Here μ_0 is the permeability of free space (1.257 X 10^{-6} henry/meter), I is the current in amps in the wire, R, the radius in meters of the wire, and Z the distance in meters from the center of the loop in the z-direction. The magnetic field also has components in the x-direction and the y-direction. In the plane of the wire, Z becomes zero and Equation (1.2) reduces to

$$B_z = \frac{\mu_0 I}{2R} \tag{1.3}$$

and in this case the other components of the magnetic field are zero. Here it is obvious that when the loop is smaller, the magnetic field is stronger for a given current in the coil. The operator should choose an antenna as small as possible, but large enough to radiate the entire sample of interest.

Inducing NMR

In order to create an MRI image it is necessary to stimulate a nuclear magnetic resonance in the target. The body is placed in the DC magnetic field. The RF pulse is polarized at 90 degrees with the DC magnetic field. The angle of precession that occurs depends upon the magnitude and duration of the pulse shown at the top of Figure 1.4. The magnetization angle of precession with the DC magnetic field, θ, may be calculated from,[1.4]

$$\theta = 2\pi\gamma B_1\tau \tag{1.4}$$

where γ is the gyromagnetic ratio, B_1, the magnetic field from the RF pulse and τ is the duration of the pulse. Thus, by adjusting the duration and/or the intensity of the RF pulse one can set θ to different angles. In practice the angles $\pi/2$ and π radians are often used. When $\pi/2$ is chosen, we produce a 90 degree precession, and the magnetization vector lodges in the x - y plane. After the RF pulse is turned off, the magnetization vector continues to precess, but it falls off exponentially with a time constant T1. This produces a continuation of the RF radiation, illustrated in Figure 1.4, as a free induction decay (FID) signal. That is, the

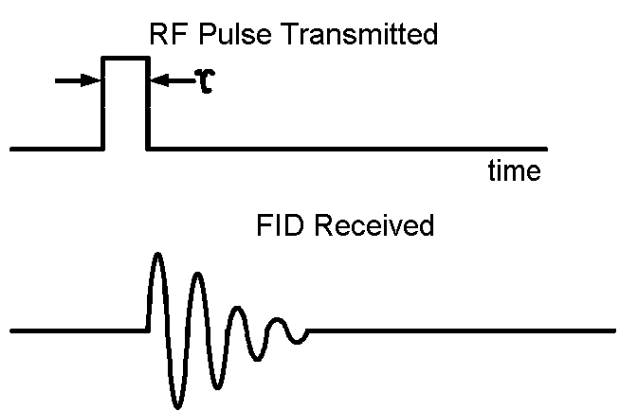

FIGURE 1.4. Free induction decay

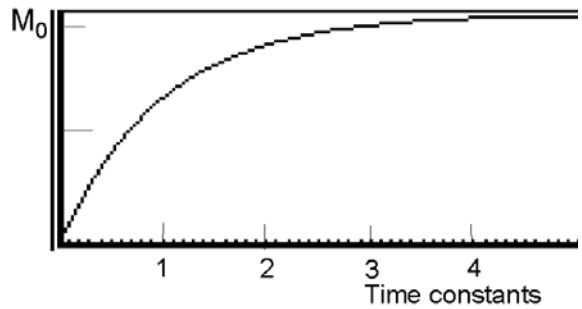

FIGURE 1.5. Magnetization, M_Z

magnetization M_Z returns to its original value M_0 according to the equation

$$M_Z = M_0(1 - e^{-t/T1}) \tag{1.5}$$

where M_Z is the atomic magnetization in the z-direction, M_0 is the value after the effect of the RF pulse has transpired, and T1 is the time constant. This equation is plotted in Figure 1.5. At t = 0 M_Z is zero, and after 5 time constants it rises to M_0, and the magnetic dipoles are realigned with the applied DC magnetic field.

The value of the time constant T1 varies from .2 to 2 seconds in the brain. Some example values appear in Table 1.2 [1.5]. The time constant of decay for the Thalmus is 703 ms. This means the magnetization will recover 63.21% of its original value in 703 ms after the RF is shut off, and in five time constants it will be essentially zero. The difference in the T1 values is used in the MRI to distinguish between these tissue types.

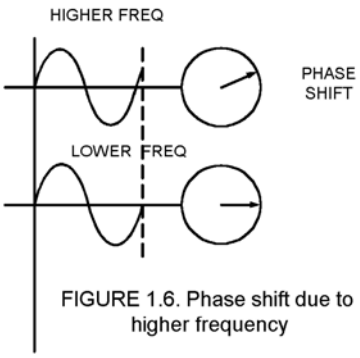

FIGURE 1.6. Phase shift due to higher frequency

The magnetization, M_{XY}, in the x-y plane is influenced by a dephasing process. The individual atoms in a particular pixel are oscillating at slightly different frequencies. Therefore as time passes they fall out of phase with each other, and their magnetizations sum to a value less than that if they remained in phase. This causes M_{XY} to decrease. Dephasing due to frequency differences is illustrated in Figure 1.6. Notice the two waves begin in phase, but by the end of the cycle, the higher frequency wave is leading in phase.

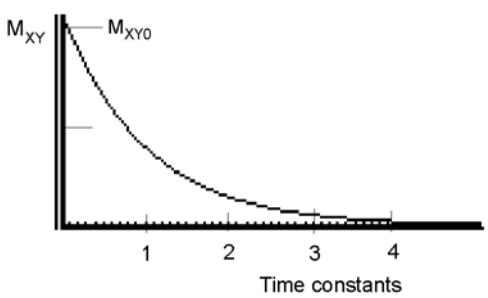

FIGURE 1.7. X-Y Plane magnetization.

Magnetization in the x-y plane after the RF stimulus is turned off follows the formula

$$M_{XY} = M_{XY0} e^{-t/T2} \tag{1.6}$$

where M_{XY} is the atomic magnetization in the x-y plane, M_{XY0} is the value the instant after the RF pulse has transpired (t = 0), and T2 is the time constant. This equation is plotted in Figure 1.7. After 5 time constants the value of M_{XY} diminishes nearly to zero. Notice in Table 1.2 that the time constant T2 is much less than T1. Therefore the M_{XY} fades

Table 1.2 Brain tissue relaxation times

ORGAN	T1(ms)	T2 (ms)
Thalamus	703 +/- 33	75 +/- 4
Cortical gray matter	871 +/- 73	87 +/- 2
Superficial white matter	515 +/- 27	74 +/- 5
Cerebrospinal fluid	1900 +/- 353	250 +/- 3

away before M_Z has re-aligned. This fact is important in the Spin-echo RF stimulus technique discussed below.

FID

During the time T1, the magnetic dipoles are precessing around their respective atoms, and they radiate RF energy, shown in the lower part of Figure 1.4. Its magnitude diminishes exponentially with the time constant T1, and the dephasing process. The signal, called the field induction decay (FID), can be picked up by the same antenna, as shown in Figure 1.2, that transmitted the stimulus RF pulse. This time the antenna is switched to the receiver. In the nuclear magnetic resonance (NMR) procedure, the sample is radiated by a band of frequencies; the one which equals the Larmor frequency, given by Equation (1.1), will stimulate the sample. It precesses at its Larmor frequency when the RF is shut off. By measuring the frequency of the received FID and using Equation (1.1), one can calculate the gyromagnetic ratio γ, of the sample, provided the DC magnetic field strength is known.

EXAMPLE 1.1. A sample is placed in a DC magnetic field of 1.5 T. It is radiated by a short RF pulse, whose magnetic field is perpendicular to the DC field. An antenna connected to a radio receiver and oriented as in Figure 1.1 is used to pick up the field induction decay. The frequency of the FID is measured as 63.87 Hz.

a. Compute the gyromagnetic ratio of the sample.

b. Use Table 1.1 to identify the sample.

SOLUTION

Part a. From Equation (1) we compute

$$\gamma = \frac{f}{B_0} = \frac{63.887Hz}{1.5T} = 42.58\frac{Hz}{T}$$

Part b. The atom with this geomagnetic ratio is seen in Table 1 to be hydrogen (1H).

Spin Echo

Spin Echo is a technique for stimulating NMR that helps compensate for signal loss due to slight differences of the DC magnetic field as a function of position. Such differences, or inhomgenaities, cause atoms to precess at different frequencies according to the Larmor equation. They therefore spread further and further in phase as time progresses. The individual atom magnetic vectors will therefore add up to less than they would if they were all in phase, resulting in a loss of signal. To counter this the spin-echo RF pulse sequence is applied as shown in Figure 1.8. At a time t = 0, when the 90º pulse ends, and FID begins as shown in Figure 1.8, some magnetization vectors lead others in phase. At time TE/2, a 180º pulse of RF is applied which causes the leading magnetization vectors to lag. But since they are at a higher frequency, at time TE, they catch up and all magnetization vectors are in phase again. (This process can be compared to a noncompetitive race in which the runners start at the gun together. The faster ones lead, but the gun is fired again, signaling all the runners to turn around and head back to the starting line. They all finish at the starting line together because the faster ones run further.) This gives an increased signal, called the echo. Thus the spin-echo technique improves the FID signal.

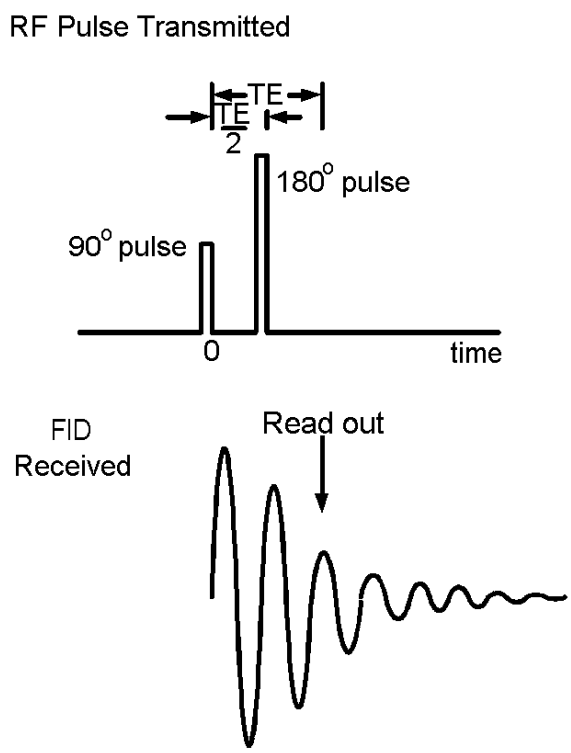

FIGURE 1.8.The Spin-echo Excitation.

Magnetic Resonance Imaging

NMR evolved into a medical imaging technique when Paul Lauterbur investigated the Larmor Equation (1.1) and realized that a change in applied magnetic field changes the frequency of precession of any particular atom. Thus if the applied magnetic field intensity is shaped as a function of position, a measurement of the frequency of resonance of known atom types can be correlated to their position. The human body is

more than 60 percent water, therefore it is convenient to detect hydrogen, 1H, listed in Table 1.1. The other important factor is the relaxation times T1 and T2, some of which are listed in Table 1.2. These values differ among the tissues the hydrogen appears in and can be used to identify the type of tissue. In summary:

- Frequency of the FID measures tissue position
- Relaxation times of the FID identify tissue type

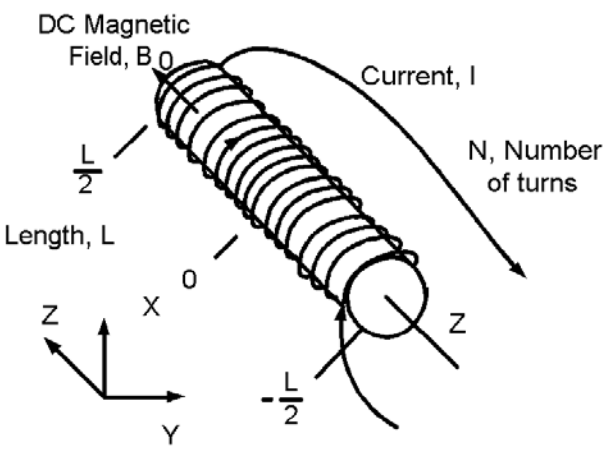

FIGURE 1.9. DC Magnetic Field Coil.

The first alternation of the NMR apparatus needed to make it into an MRI is to shape the magnetic field as a function of position under the DC magnet. This is done with coils which cause a variation of the field in the x-direction, G_x, the y-direction, G_y, and the z-direction, G_z, written as:

$$G_x = \frac{\partial B_x}{\partial x} \tag{1.7a}$$

$$G_y = \frac{\partial B_y}{\partial y} \tag{1.7b}$$

$$G_z = \frac{\partial B_z}{\partial z} \tag{1.7c}$$

where B_x, B_y, and B_Z are the magnetic fields created by the x-direction, y-direction and z-direction coils respectively.

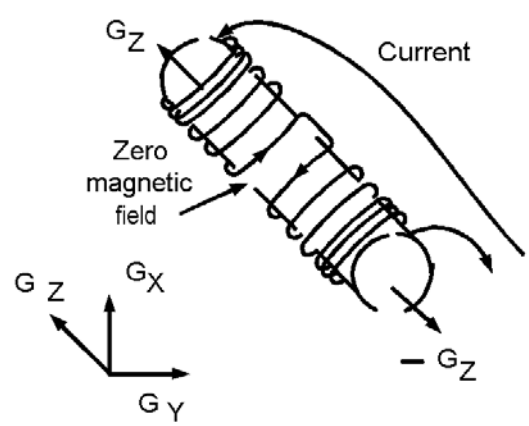

FIGURE 1.10 Z-DIRECTION MAGNETIC FIELD COIL

The DC Magnetic Coil

The DC magnetic field may be produced by a permanent magnet, illustrated in Figure 1.1 when small samples are being imaged. But for most medical applications an electromagnetic magnet is used, as illustrated in Figure 1.9. The DC magnetic field in this case is produced by a solenoid, a wire wrapped around a cylindrical core, large enough to allow one to insert a prone human body for imaging. The magnetic field in core, whose radius is much smaller than its length, at its center, is given approximately by [1.6]

$$B_0 = \frac{\mu NI}{l} \qquad (1.8)$$

Where μ is the permeability in Henry per meter (H/m) (1.257×10^{-6} H/m in free space), N is the number of turns, I is the current in amperes, and l is the length in meters, and B_0 is the magnetic field in the direction of the axis of the coil in Tesla (T) units.

EXAMPLE 1.2. How many amps are required to produce a 1.5 T magnetic field at the center of a solenoid which is 4 meters long, having 10,000 turns of wire?

SOLUTION. Solving Equation 1.7 for I, and substituting the numbers gives,

$$I = \frac{1.5Tx4m}{1.25x10^{-6}(H/m)x10000} = 480 \text{ amps}$$

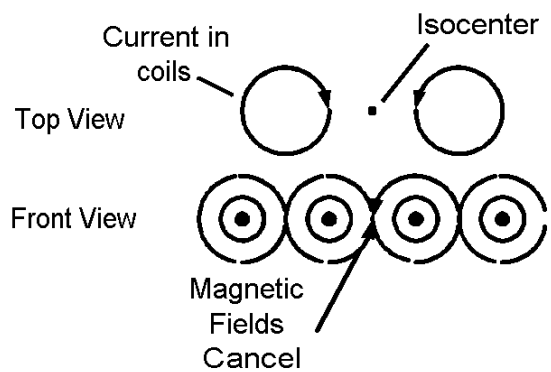

Figure 1.11

Field Shaping Coil in the Z-direction

The field shaping coil which produces G_Z, Equation (1.7c), the variation in the field in the z-direction, is illustrated in Figure 1.10. Notice at the top end of the coil, a current entering in the direction of the arrow produces a positive magnetic field gradient, G_Z. Then as you proceed down the coil, the spacing between turns increases, causing a smaller magnetic field. In the middle of the coil, the magnetic field reduces to zero. Going further, the turns direction is reversed, G_Z become negative, and continues such to the end of the coil. The spacing between the coils is varied so that the magnetic field varies linearly from $+G_Z$ to $-G_Z$.

Field Shaping Coil in the X- and Y-directions

To understand how field is caused to vary in the x-direction, consider two coils side-by-side as shown in the top-view of Figure 1.11. The magnetic fields caused by these currents are shown in the front view. Notice the currents are going in opposite directions, and therefore, by the “right hand rule” produce opposing magnetic fields at the isocenter, which cancel to zero.

Now four coils are arranged as shown at the top of Figure 1.12. Looking at section A-A' we see that the magnetic fields produced by the currents in the directions shown, cancel at the center of the four-coil structure. Thus an isocenter appears as shown in the lower part of the figure. As you travel in the positive x-direction, the magnetic field increases positive, and in the negative x-direction goes negative.

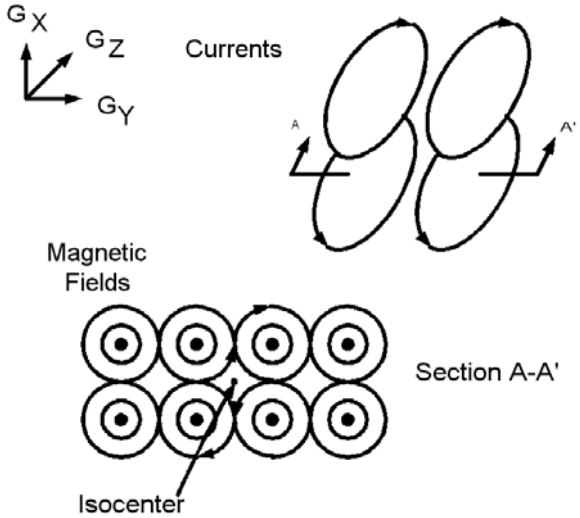

Figure 1.12. Magnetic field gradient in the x-direction.

A set of coils turned at right angles to the ones in Figure 1.12, would likewise produce a magnetic field which varies in the same way in the y-direction.

In the MRI, these coils must fit in the cylindrical hole in the gantry, that the body of subject being imaged must fit. Therefore the coils are bent into a saddle shape as illustrated in Figure 1.13. Here coils 1 and 3 are on the top, and coils 2 and 4 are on the bottom. The coils are arranged so that the fields vary approximately linearly in the space of interest, as shown in Figure 1.14.

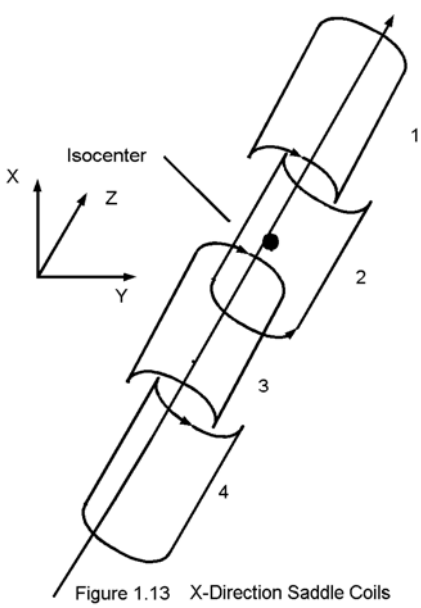

Figure 1.13 X-Direction Saddle Coils

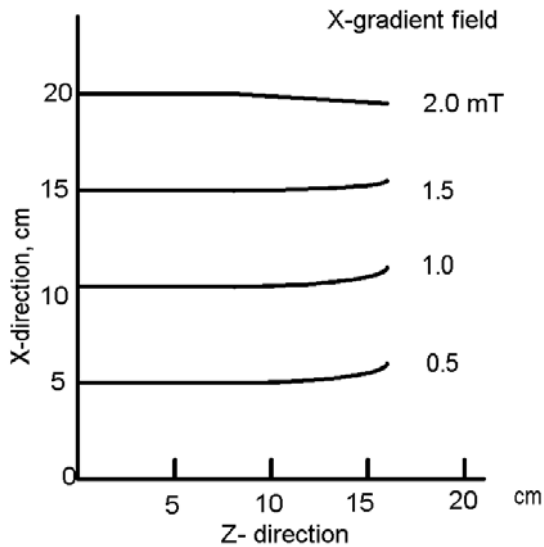

Figure 1.14 X-gradient field near the isocenter
(Vlaardingerbroek, p 27)

In this figure, empirical data from saddle coils oriented to produce a linear field variation in the x-direction is shown [1.7]. The range of linearity is approximately 10 cm in the z-direction, and at least 20 cm in the x-direction. The steeper the gradient of the magnetic field the better the resolution of the image, because differences in field strength translate into differences in frequency, which in turn measure position in the image. The coil sensitivity, C, is measured in terms of the amount of current required to produce a given magnetic field gradient. A typical value for C is 30 A/mT/m, according to Vlaardingerbroek.[1.8] In operation, this current must be delivered by a short pulse. The pulse rise time, τ_R, is an important design parameter. In terms of the inductance L and resistance R of the coil this is given as,

$$\tau_R = \frac{L}{R} \tag{1.9}$$

Vlaardingerbroek gives a typical value of L as 200 μH. He also cites the field gradient as 12 mT/m, rise time 0.6 ms, and the peak power 43 kW .

EXAMPLE 1.3. A saddle coil used to shape the magnetic field in the y-direction has an inductance of 200 μH and a rise time of 0.6 ms. What is the resistance of the coil?
SOLUTION:
From Equation (1.9) we calculate

$$R = \frac{L}{\tau_R} = \frac{200x10^{-6}}{0.6x10^{-3}} = 0.33\Omega$$

EXAMPLE 1.4. A saddle coil draws 30 A peak current and 43 kW of power. What is the peak voltage, V?

SOLUTION:

$$V = \frac{43000}{30} = 1433.3 \text{ V}$$

EXAMPLE 1.5. If the magnetic field gradient in the y-direction is 12 mT/m in a DC magnetic field of 1.5 Tesla, what is the corresponding frequency gradient of the precessing hydrogen atoms?

SOLUTION: From Table 1.1, the gyromagnetic ratio of 1H in the 1.5 T field is 42.58. Thus

$$\Delta f = 1.5x42.58\frac{MHz}{T}x12x10^{-3}\frac{T}{m}$$
$$= 0.766\frac{MHz}{m}$$

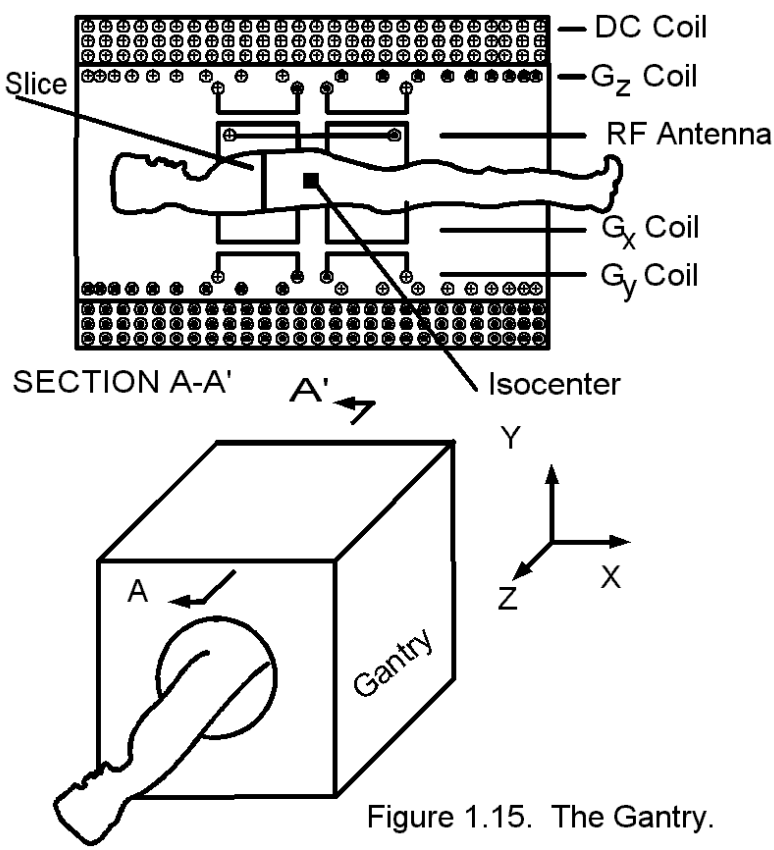

Figure 1.15. The Gantry.

The Gantry

The Gantry, shown in the bottom of Figure 1.15, is a structure that insures a proper orientation of the subject being imaged, the magnetic coils and RF antenna coil. In top of the figure the coils described above are shown, giving the direction of the currents. The plus sign, +, indicates the current is going into the page, and the dot, •, indicates a current coming out. The patient rests on a pallet and is positioned in the hole in the gantry, as shown.

The DC coil in Figure 1.15 causes a constant magnetic field, B_Z, in the z-direction which is always on. The effect of the other coils is to shape the magnetic field so that the atoms being imaged are under different magnetic fields, and according to the Lamor equation, will emit different frequencies, according to their position. Energizing the G_Z coil causes variation of the magnetic field along the z-axis, G_Y along the y-axis, and G_X along the x-axis. Energizing the RF coil makes the atoms precess. We will now discuss how and when this magnetic field shaping takes place, and how an MRI image is developed. A knowledge of the Fourier Transform is basic to our understanding this process.

The Fourier Transform

As we discuss in Appendix B, the Fourier Transform is an extension of the fourier series. A fourier transform pair is given by two integral equations, (B2) and (B3) in Appendix B, as:

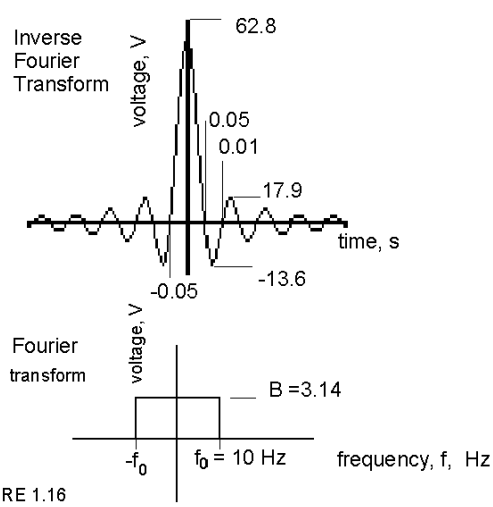

FIGURE 1.16

$$f(t) = \frac{1}{2\pi} \int_{-\infty}^{\infty} F(\omega) e^{j\omega t} d\omega \tag{1.10}$$

$$F(\omega) = \int_{-\infty}^{\infty} f(t) e^{-j\omega t} dt \tag{1.11}$$

Here $F(\omega)$ is the fourier transform of f(t). Equation (1.10) is a function of time alone, since the radian frequency, ω, is a running variable. We therefore say the function f(t) is in the time domain, while $F(\omega)$ is in the frequency domain. Equation (1.11) expresses that function in the frequency domain, since it is a function of frequency alone. Equations (1.10) and (1.11) form a fourier transform pair, (1.11) being the fourier transform, and (1.10) being the inverse fourier transform.

An example fourier transform pair, shown in Figure 1.16 and calculated in Appendix B, is very important to the operation of the MRI. A voltage pulse shown in the top of Figure 1.16 is a function of time, v(t). Its fourier transform, calculated from Equation (1.11) has the form V(f) shown in the lower part of the figure, as calculated in Example B2 in Appendix B. The practical significance of this in the MRI is that a pulse of RF applied to the antenna coil of the shape shown in the top of the figure has frequency components given in the lower part of the figure. Furthermore the value of the frequency components is adjusted by changing the voltage waveform in the time domain. Because each of these frequency components causes atoms to precess, or be illuminated, at different positions in the subject, this gives the operator a means of selectively illuminating different parts of the body with the RF antenna coil.

The MRI Block Diagram

The block diagram of the MRI appears in Figure 1.17 which is used to show how the parts described above are interrelated to produce an image.

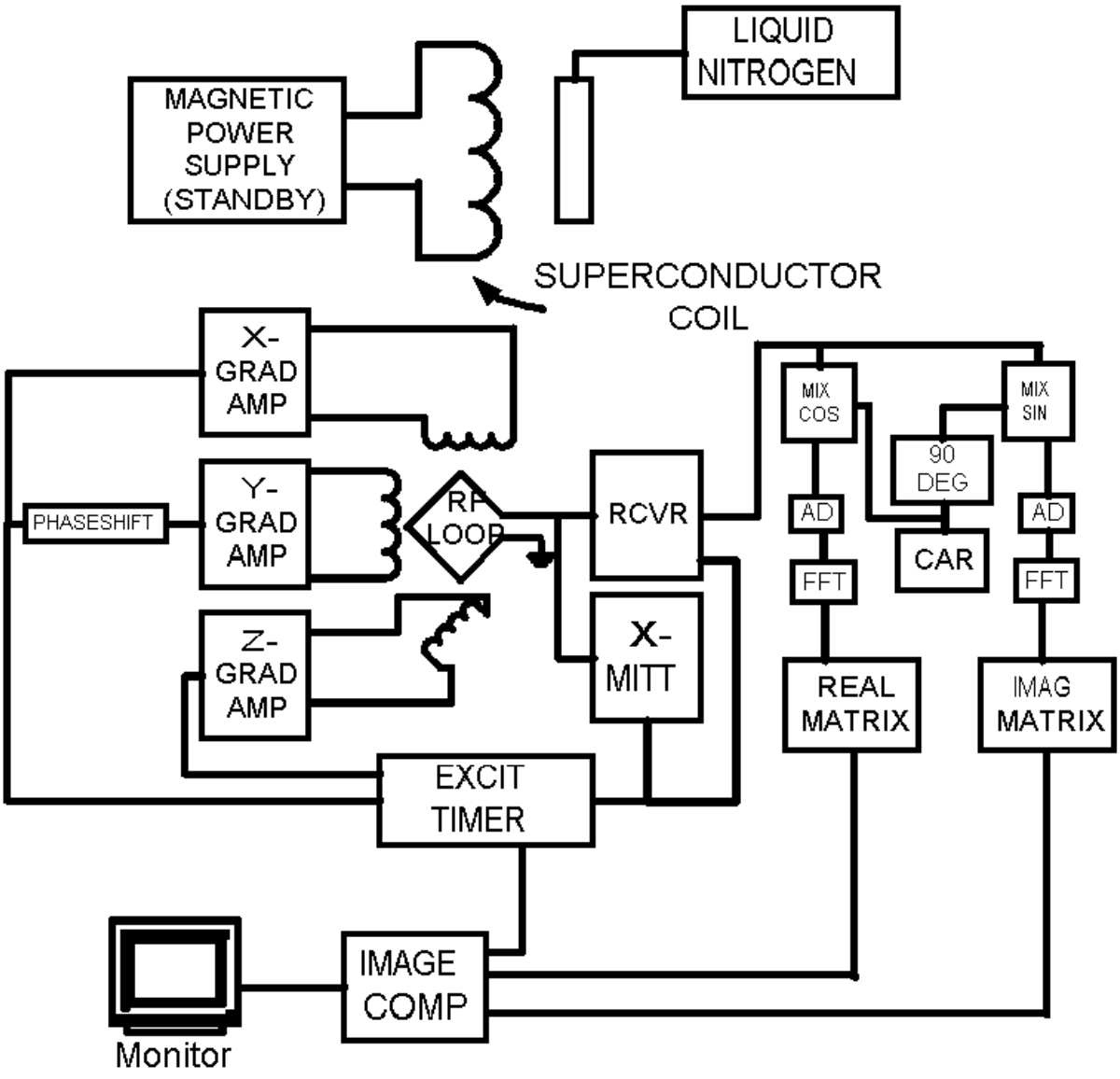

FIGURE 1.17. MRI BLOCK DIAGRAM.

The subject being imaged is under the RF loop antenna and through the gradient coils as shown in Figure 1.15. The transmitter in Figure 1.17 energizes the RF loop antenna in order to cause the hydrogen atoms in the subject to precess. The x, y and z-gradient amplifiers create the magnetic field gradients by driving currents into the appropriate gradient coils. When the transmitted RF is turned off, the receiver is turned on to pick up the signal from the subject and process it into an image. The details of this process follow:

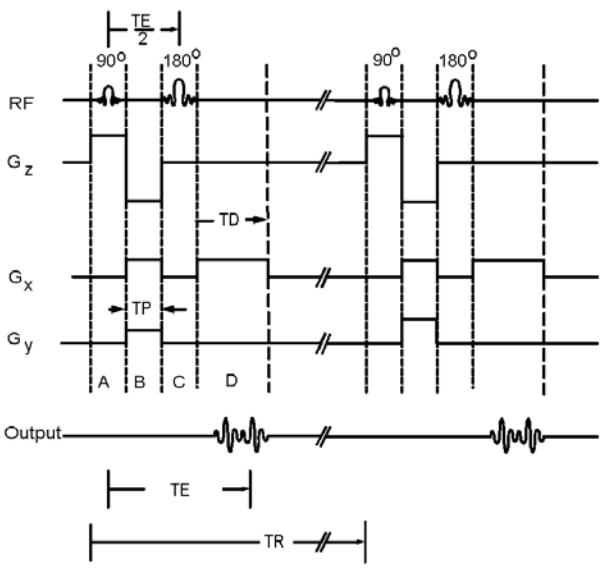

FIGURE 1.18 EXCITATION PULSE SEQUENCE (Wehrli, p.11)

The signals controlled by the MRI electronics are illustrated in Figure 1.18 which follows Wehrli.[1.9] Here the time sequence of the pulses which excite the RF antenna coil and the magnetic field shaping coils is shown. The sequence of pulses shown is repeated, for example, 256 times to acquire the data needed to make one slice through the subject imaged, shown in Figure 1.15. The data from each voxel in the slice is recorded in a matrix representing the x-y plane as illustrated in Figure 1.19. One way to understand how the pulses in Figure 1.18 create an image is to imagine yourself on one of the voxels in the slice. The RF pulse creates a spin-echo sequence as described above. The waveshape is “sine x over x” (sinc x), the fourier transform of which is a band of frequencies. Simultaneous with the first 90° RF pulse in time period A, the z-direction coils are energized so that the magnetic field in one of the slices would cause spins in its voxels corresponding to those in the RF pulse, as demanded by the Lamor equation. Thus the RF pulse and magnetic field gradient G_Z work together to select or illuminate one slice. The voxels in that slice precess at frequencies determined by the Lamor equation and the gyromagnetic ratio of the tissue in the voxel after the 90^0 pulse is turned off. The phase of the precession in the slice differs from what it would be if it were at the isocenter of the magnetic field because the frequency is different, as illustrated in Figure 1.6. To compensate for this the next pulse in time-period B from the z-direction gradient is in the opposite direction, making a frequency shift of opposite sign from the

isocenter. Thus all slices will have the same phase due to the z-direction magnetic field as that at the isocenter.

In time-period B, G_X and G_Y gradients are energized so that the magnetic fields across the slice of Figure 1.19 vary linearly in the x and y directions. Thus the voxels in the slice each take on different frequencies as determined by the Lamor equation and the differing magnetic fields, and by the end of the time-period, B acquire different phases.

In time-period C, all magnetic field gradients are shut down so the Lamor equation and the magnetic field B_0 alone determine the frequency of resonance, but the phase differences will remain as set in time-period B. The 180° RF pulse is applied to cause cancellation to dephasing according to the spin-echo method described above.

In time-period D, the gradient G_X is applied. This causes frequencies of precession to vary linearly as a function of x in the slice, but the phases in the y-direction will remain as set in time-period B. In period D, the receiver in the block diagram, Figure 1.17, is turned on. The summation of all the radiations from the voxels in the slice are picked up by the antenna coil. The received signal is in the time domain. The signal contains a set of frequencies, magnitudes and phases of each of the 256^2 voxels in the slice which can be analyzed by fourier transform techniques as discussed below.

The time periods discussed are in the order of 10 to 30 ms. The voxels in the slice will continue to resonate up to 1 or 2 seconds, as shown in Table 1.2. After these resonances have ceased, the time TR, another sequence of pulses in figure is applied. They are all identical to the first set, except the magnetic field gradient G_Y is set to another value. Thus the 256^2 voxels will precess as before, except the phase shifts in the y direction will differ. This process is repeated 256 times, in order to give enough data characterize all 256^2 voxels in the slice. Typical times required to image one slice by this method is 256/60 = 4.3 minutes to 8 minutes. Since the echo time TE is in the order of 10 milliseconds, computer time-sharing can be used to make many slices in this 4 to 8 minutes.

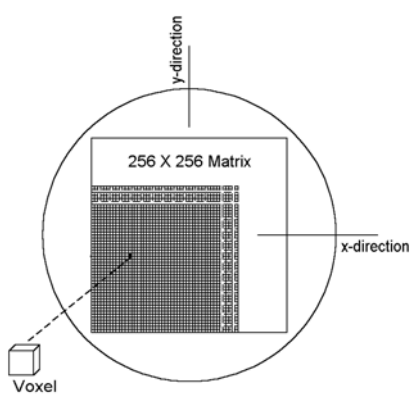

FIGURE 1.19 SLICE IN THE X-Y PLANE

Signal Processing

To understand how the signal emitted from the voxels in the patient produces an image in an MRI, it is useful to consider an analogy of what happens when we hear a cord struck on a piano. In both cases fourier transforms operate.

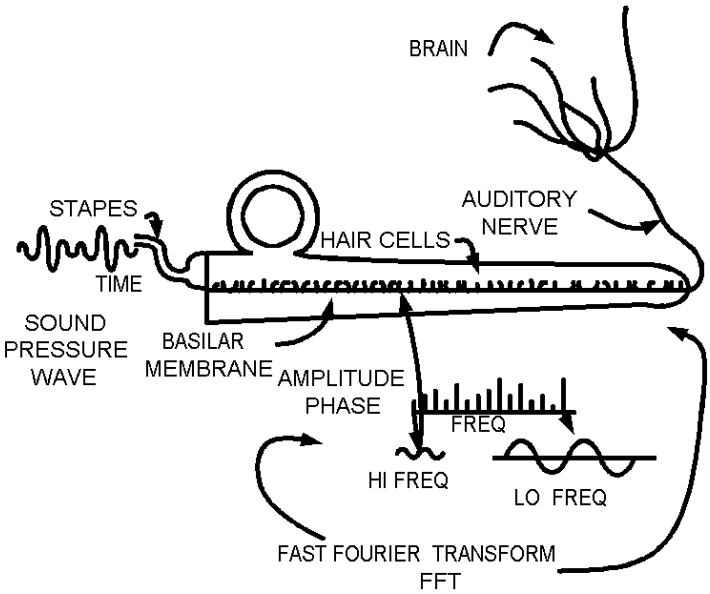

FIGURE 1.20. The Inner Ear as a Fast Fourier Transform.

When we strike a cord on the keys of a piano, the individual strings vibrate at their own resonant frequencies, much as voxels do in the slice of the patient in the MRI. The strings are spatially arranged in the piano as are the voxels in the slice. The set of vibrating piano strings form a fourier transform. The sounds from the individual strings add in the air and become a pressure wave that varies as a function of time which is applied to the ear as shown in Figure 1.20. Likewise, the RF vibrations of the voxels in the slice in the MRI add in air and become a function of time applied to the receiver antenna loop.

In Figure 1.20, the sound pressure wave enters the inner ear through the stapes bones that set up a standing pressure wave in the cochlea. Low frequency sounds cause stronger vibrations deep in the ear, to the right, and high frequency sounds cause stronger vibrations to the left. The hair cells on the basilar membrane pick up these vibrations and transmit the signal to particular locations in the brain by way of the auditory nerve. Thus the ear serves to transform a sound pressure wave shown in Figure 1.20 into frequency components located as a function of position along the cochlea. This transformation in mathematics is called a Fourier Transform. Furthermore, because the process occurs fast enough that one speech sound after the other can be individually analyzed

into its frequency components and presented to the brain in real time, the process is called a Fast Fourier Transform(FFT).

The frequency components of the sound are then transmitted along individual nerve fibers to spatially distinct places in the brain, and the listener interprets the sound as music. In the MRI the radio wave picked up by the antenna loop is operated on by an FFT and the individual frequency components are placed in spatially distinct memory locations in the computer which create an image on a display unit. Thus the computer in the MRI functions in an analogous manner to the brain.

Receiver Processing

The output of a slice on the patient from the sequence of excitations depicted in Figure 1.18 is an electromagnetic wave having a frequency usually between 40 and 100 MHz. It is picked up by the RF loop antenna and applied to two mixers [(1.10)] which amplitude modulate it with a carrier, one being 90 degrees phase shifted from the other. That is, one mixes with cosine functions and the other with sine functions [(1.11)]. After analog to digital conversion (ADC) on the block diagram, a fast fourier transform (FFT) is performed on these outputs to produce the magnitudes and phases of one row of a matrix for each presentation of the excitation sequence of Figure 1.18. The real part of the complex number comes out of the Mixer (cos) and the imaginary part from the Mixer (sin) in Figure 1.17. After 256 repeats of this excitation, in the example we are considering, two matrices are formed, one for the real part and one for the imaginary part, from which the magnitudes of the radiations of one slice of voxels can be calculated by algorithms in the computer and placed in their correct positions to create a visual image.

Image Resolution

The image resolution, Δx, in the x-direction and Δy in the y-direction, is the minimum size object that can be distinguished. A measure of this can be derived from the Lamor Equation (1.1). Differentiating this equation,

$$\frac{df}{dx} = \gamma \frac{dB_x}{dx} = \gamma G_x = \frac{\Delta f}{\Delta x} \qquad (1.12)$$

where we replace the differentials df and dx with discrete differences Δf and Δx. So

$$\Delta x = \frac{1}{\gamma G_x}\Delta f \qquad (1.13)$$

Here Δf represents the difference in frequencies between a voxel and its adjacent one in a slice shown in Figure 1.19. The number of voxels in the x-direction we call N_x. The duration of the output pulse we call TD in Figure 1.18. Thus the bandwidth, BW, of the output RF applied to the antenna coil is

$$BW = N_x \Delta f \qquad (1.14)$$

Equation (1.13) shows that to achieve better spatial resolution it is necessary to select between closer frequency spacings. One can visualize tuning across the bandwidth with a more narrow band receiver for better resolution. The time to scan the entire band should be longer for better resolution. . S Wright [1.12] shows that

$$\Delta x = \frac{2\pi}{\gamma G_x TD} \qquad (1.15)$$

Thus the best resolution occurs for a large magnetic field gradient, G_x, and for a long duration RF output pulse.[1.13]

EXAMPLE 1.6 A typical MRI has a magnetic field gradient, G_X = 12 mT/m, the DC magnetic Field is 1.5 T and an RF output duration, TD = 20 ms . What is the resolution in the x-direction.
SOLUTION: The gyromagnetic factor, γ = 1.5x42.6 from Table 1.1. Thus Equation (1.14) yields,

$$\Delta x = \frac{2\pi}{1.5x42.6x10^6 x12x10^{-3} x20x10^{-3}} = 0.41mm$$

Thus we can theoretically resolve an object larger than 0.41 mm in width in this case.

Signal to Noise Ratio

The signal to noise ratio, SNR, is increased by factors that make the RF signal larger. These are the DC magnetic field, the voxel volume, V_V, and the output duration, TD. Conolly [1.14] gives the value as proportional to

$$SNR \propto B_0 \sqrt{TD} \frac{V_V}{V_n} \tag{1.16}$$

where V_n is the noise volume. V_n increases with the total volume being imaged, and the SNR is degraded when larger volumes are imaged. Thus the SNR is degraded when one attempts to use a smaller DC magnet, improve the resolution with smaller voxel volumes, and to create images faster by decreasing TD.

Mathematical Model for Image Creation

A Mathematical model that can be programed on the computer to create an image begins with the individual voxel. During the readout of the magnetization resonance, TD, in Figure 1.18, each voxel emits a magnitude due to its tissue type and depending on its position, ρ(x,y,z), and a phase that is generated by the magnetic field gradients given by

$$e^{-i\gamma \int_0^t \overrightarrow{G(\tau)} \cdot \vec{r}\, d\tau}$$

where γ is the magnetization coefficient in units of MHz/T, G, the magnetization gradient is a vector

$$G = \hat{x}G_x + \hat{y}G_y + \hat{z}G_z \tag{1.16}$$

which forms a dot product with a position vector

$$r = \hat{x}x + \hat{y}y + \hat{z}z \tag{1.17}$$

All of these radiations reach the receiver antenna and add to form a signal, s(t) as a function of time given as[1.5]

$$s(t) = \int_{-\infty}^{\infty} \int_{-\infty}^{\infty} \int_{-\infty}^{\infty} \rho(x, y, z) e^{-i\gamma \int_0^t \overrightarrow{G(\tau)} \cdot \vec{r}\, d\tau} dx\, dy\, dz \tag{1.18}$$

k-space is defined by the quantity

$$\vec{k}(t) = \frac{\gamma}{2\pi}\int_0^t \vec{G}(\tau)\,d\tau \qquad (1.19)$$

which has the units per meter (m^{-1}), and is a quantity depending on the magnetic field gradients chosen in the MRI as well as the γ values of the different tissues in the slice. This forms the k-space vector

$$k = \hat{x}k_x + \hat{y}k_y + \hat{z}k_z \qquad (1.20)$$

so Equation (1.18) becomes this

$$s(t) = \int_{-\infty}^{\infty}\int_{-\infty}^{\infty}\int_{-\infty}^{\infty} \rho(x,y,z)e^{-i2\pi\vec{k}\cdot\vec{r}}\,dx\,dy\,dz$$

$$= S(\vec{k})$$

(1.21)

This has the form of a three dimensional Fourier transform. As stated in Appendix B, Fourier has shown that it has an inverse equality given by

$$\rho(x,y,z) = \int_{-\infty}^{\infty}\int_{-\infty}^{\infty}\int_{-\infty}^{\infty} S(\vec{k})e^{+i\gamma 2\pi\vec{k}\cdot\vec{r}}\,d\vec{k}$$

(1.22)

This equation is calculated by the computer for each of approximately 256 times the pulse sequence of Figure 1.18 is applied, and a gray-scale image is formed.

Hardware Data

Progress in the development of the MRI is limited, in large measure, to the size of the DC magnetic field. The higher this field is, the better the image is. It has a higher signal to noise ratio and more elements can be imaged other than hydrogen, such as phosphorous and sodium. However the magnetic field is limited by the physical size of the magnet. Three types of magnets have been used: permanent, electromagnets, and superconductor electromagnets. A Permanent magnet is illustrated in Figure 1.21. The DC magnetic field must be as uniform as possible to prevent signal loss due to dephasing, as discussed above. The soft iron shims shown in Figure 1.21 provide a standard way of calibrating the field. The metal alters the magnetic field pattern in a controlled fashion, and can be conveniently adjusted . MRIs use fields between .02 to 8 Tesla (1 Tesla = 10,000 Gauss) and more. The higher the DC magnetic field, in many cases, the better because

- Larger fields yield better contrast and intensity of images
- Larger fields glean scans of more types of elements

It is easy to achieve a multitesla field if the gap in magnet is small. But it becomes difficult if the gap must be large enough to pass a person. Smaller gap MRIs may be used to image the head, or knee alone for example. Permanent magnets may be used in low field applications of less than 0.3Tesla (T). They have the advantage of low maintenance and operating costs. However they are heavy, in the order of 20 tons at the 0.2 T level if iron is used in a magnet capable of imaging a patient. With neodymium alloy, the weight reduces to 4½ tons.

A second alternative, resistive magnets are electromagnets in which the magnetic field is produced by a coil of ordinary conductive wire, usually copper, wrapped around an iron core, such as illustrated in Figure 1.9. They are usually used only in small field applications of 0.02 to 0.06 T. For high field applications they require high current and present

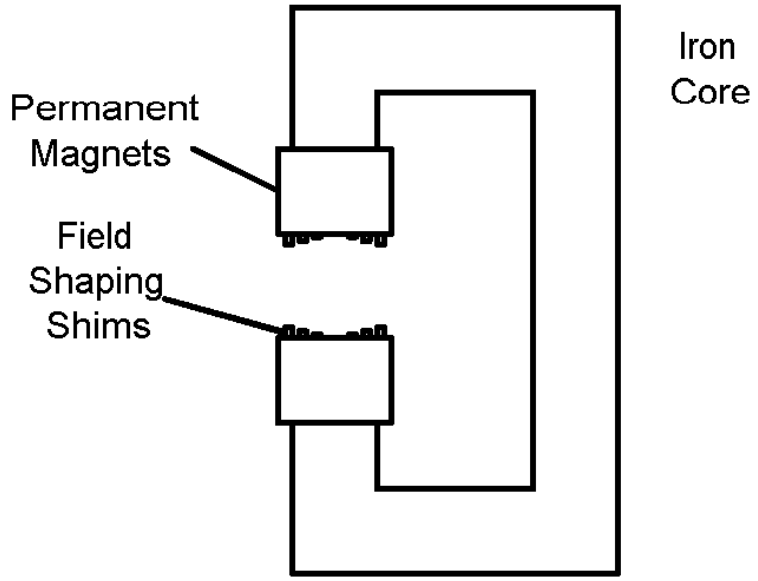

FIGURE 1.21. Permanent Magnet Cross Section.

cooling problems. For example, a 0.3 T magnet capable of imaging a patient requires 100 kilowatts (kW) of power. [1.16] A third alternative, superconductor magnets, were developed in the 1980s, and have made 8 Tesla DC magnets practical. Superconducting wire must be cooled to a very low temperature. For example niobium-titanium wire becomes a superconductor below 10 degrees Kelvin (K) above absolute zero. Figure 1.22 shows a superconducting coil magnet for an MRI. It has chambers for both liquid nitrogen which is a low cost barrier to room temperature and liquid helium which brings coils to superconductivity. The superconducting coils are maintained at liquid helium temperatures. As the temperature of the helium rises from heat absorption, new liquid is added to the chamber through the cryogenic transfer neck shown in the figure. The coolant is usually replaced about every five weeks. A vacuum jacket is used to provide insulation for maintaining cooling . The magnetic field in the bore, or tube, in the gantry is made homogenous by adjustment of the shim coils. If the temperature is maintained below the superconducting threshold, the DC magnetic field may be maintained for weeks without power being delivered to the coils, as the magnetic loss is less than 0.001 gauss per hour. For example, 200 Amps of current produces a 1.5 T magnetic field in a 1.3 meter diameter tube. Since the current is flowing in a superconductor, it produces essentially no power loss. A larger diameter tube would require more current to produce this field strength.

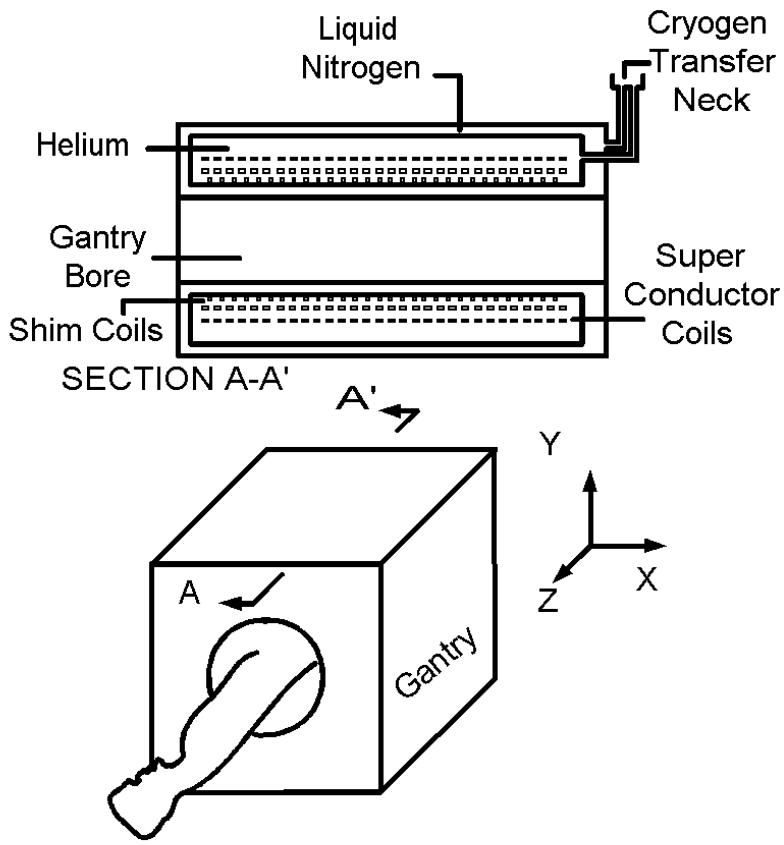

Figure 1.22. Super Conductor Magnet.

Occasionally the magnet will suddenly loose its field in a fault process called “quenching”. Vibrations in the coils may produce enough heat to cause a local loss of super conductive temperature and the current in the coils generate more heat. The process avalanches and the magnetic field is rapidly lost, sometimes with a loud noise. [1.17]

When an MRI scan is taken, the patient is placed on a computer-controlled pallet and moved into the tube in the gantry. In closed versions of the MRI, the tube is rather long and fits closely around the patient. A small, but significant percentage of the patients experience claustrophobia in this situation. That along with the noise of the scanning equipment can make some patients uncomfortable. One source of sound is from the current pulses on the magnetic field shaping coils. Lorentz forces are set up which cause vibrations heard as noise. (This is the same process that causes hum in power transformers.) One does not feel the electromagnetic fields, and they have no measured biological effects other than those of heat generated by high power. However the magnetic field is very strong, and if a metal object gets picked up it will accelerate as it approaches the magnetic coils. Patients have been severely injured, even fatally, when hit by a metal object falling through the magnetic field.

RF Coils

An improvement on the single loop RF coil antenna, shown in Figure 1.3, was introduced by C.E. Hayes and his group in 1985,

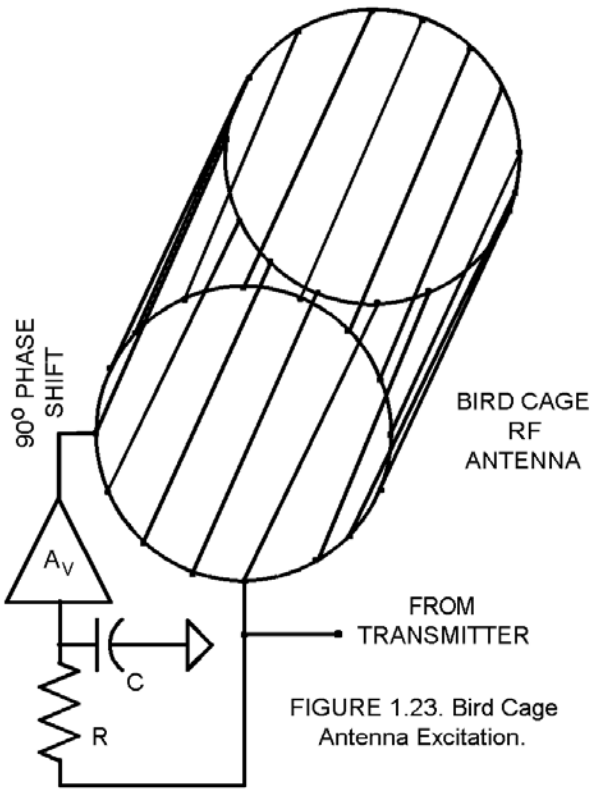

FIGURE 1.23. Bird Cage Antenna Excitation.

the Bird Cage Coil in Figure 1.23. [1.18] This device improves the sensitivity of the antenna and the signal-to-noise (SNR) ratio. The lines on the bird cage antenna in the figure are connected conductors. If one of the rings is energized with RF at two points, one stimulated 90° out of phase with the other, and displaced along the circle by 90° it will resonate such that the RF radiation is polarized in the x-y plane, or in a patient slice, and perpendicular to the DC magnetic field. The 90° phase shift may be introduced with a ¼ wave RF transmission line. Or an RC network, shown in Figure 1.23, introduces a 90° phase shift under the conditions:

$$2\pi f_r RC \gg 1 \tag{1.23}$$

$$A_V = -2\pi f_r RC \tag{1.24}$$

This result is shown in Appendix C. Here A_v is the buffer amplifier voltage gain, and f_r is the RF frequency, as calculated by the Lamor equation (1.1).

The bird cage antenna coil can be made large enough that a patient could fit through the bore. Smaller coils are used to image the head alone, and smaller to image a joint in the arm or leg.

Fast-Scan Techniques

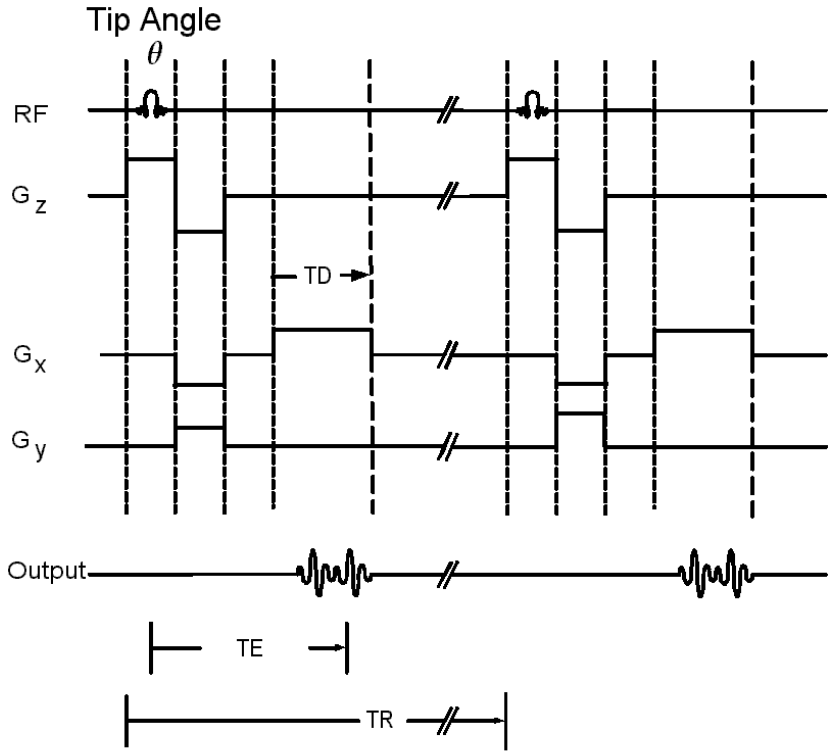

FIGURE 1.24 FAST PULSE SEQUENCE, FLASH (Wehrli, p.20)

The spin-echo scan sequence illustrated in Figure 1.18 produces a single MRI scan in 4 or more minutes in some cases. This is longer than a breath-hold by a patient, and certainly longer than the period of pulsation of the heart and other pulsating organs. Thus to eliminate organ motion and breathing artifacts it is important to find faster excitation sequences. One such method, the gradient-echo imaging, called FLASH (fast-low angle shot) by its originators [19] uses a low flip angle, θ, (as defined in Equation 1.4) and eliminates the 180° echo pulse, and does not require that the T1 and T2 transients pass before the following excitation pulse is applied. The timing diagram for the gradient-echo sequence, Figure 1.24, produces an echo by adjusting the gradient G_x so that the spins have zero phase at the center of the sampling output window. [20]

A derivation of the magnetization in the x-y plane resulting from the FLASH pulse sequence is given in Appendix D as Equation (D14),

$$M_{xy}^{0} = M_0\left(1 - e^{-\frac{TR}{T1}}\right)\frac{\sin\theta\, e^{-\frac{TE}{T2*}}}{1-\cos\theta\, e^{-\frac{TR}{T1}}} \qquad (1.25)$$

where M_0 is the initial longitudinal (z-direction) magnetization, and

M_{xy}^{0} is the component of the magnetization in the x-y plane. $T2^*$ is the x-y plane magnetization time constant modified by machine induced factors.

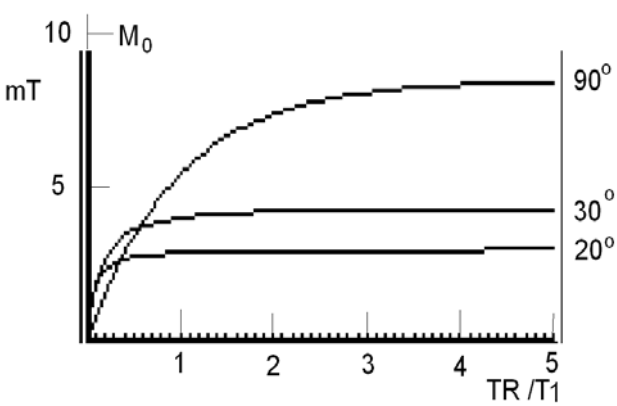

Figure 1.25. Magnitization in the x-y plane as a function of TR /T1 for various tip angles. TE = 30 ms, T2 = 300ms, and M_0 = 10 mT.

A plot of Equation (1.25) for the case TE = 30 ms, T2 = 300 ms, (here $T2^*$ is taken as equal to T2) and the tip θangles are taken successively as θ = 20, 30 and 90 degrees is given in Figure 1.25. The plot is made by programing Equation (1.25) on a Texas Instruments TI-89 graphics calculator. The abscissa , TR/T1, is carried over a range from 0 to 5.

Figure 1.25 shows that the magnetization in the x-y plane holds its value at TR/T1 ratios about at 0.1. Thus the scan time is significantly reduced. For example, if the tissue imaged has a T1 of 0.5 s, a TR of 50 ms could be practical. At 256 lines per scan, this would imply at scan time of 0.05 X 256 = 12.5 seconds, enough so that the scan could be done in one breath hold. In this method, TR should be kept greater than TE, otherwise a focusing echo would not develop.

The effect of the FLASH sequence in Figure 1.24 on the signal-to-noise ratio (SNR) helps guide the user in selecting values for TR, TE and the tip angle. The signal voltage will increase as the number of exications (NEX) increases, thus increasing the

SNR. Since noise is electrical power and signal is voltage, this increase is proportional to $\sqrt{NEX}$. Also, the TR is the time period of these excitations, so signal increase proportional to $\sqrt{[1/TR]}$.

The signal is also proportional to M_{xy} in Equation (1.25). So we write, [1.10]

$$SNR \sim \frac{1}{\sqrt{TR}} \frac{1-e^{-\frac{TR}{T1}}}{1-\cos\theta\, e^{-\frac{TR}{T1}}} \sin\theta \qquad (1.26)$$

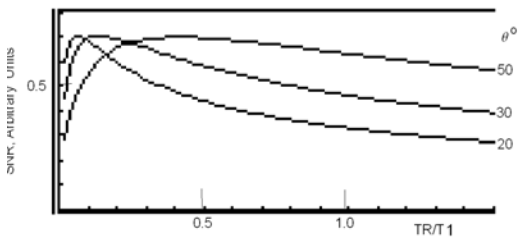

FIGURE 1.26. The effect ot scan time on SNR for various values of tip angle.

This Equation shows the effect of repetition time, TR and tip angle on the signal-to-noise ratio, and is plotted using the TI-89 graphics calculator in Figure 1.26 for the case TE = 30 ms, T2 = 300 ms, (here $T2^*$ is taken as equal to T2) and the tip angles are taken successively as θ = 20, 30 and 50 degrees.

References

1.1. Lauterbur, P. C. "Image formation by induced local interactions: Examples employing nuclear magnetic resonance." *Nature* London: vol 242 190-191, (1973).

1.2. Hornak, J.P. *The Basics of the MRI* Rochester: Rochester Institute of Technology (www.cis.rit.edu/htbooks/mri/) Ch 3, p 2 .

1.3.Vlaardingerbroek, Marinus T., Jacques A. Boer. *Magnetic Resonance Imaging: Theory and Practice.* Berlin: Springer, pp 32-33 (©1996).

1.4.Wehrli, Felix W. "Principles of Magnetic Resonance, Chapter 1" in David D. Stark and William G. Bradley, editors. *Magnetic Resonance Imaging* St. Louis: Mosby Year Book, p 5 (© 1992).

1.5. Wehrli, F. W., Chao P. W., Yousem, D. M.: "Parameter dependence of susceptibility-induced signal losses in gradient-echo imaging. *Magnetic Resonance Imaging* 7 (Supplement 1): 139 (1989).

1.6. Kraus, John D., Keith R. Carver. *Electromagnetics 2nd Edition.* New York: McGraw Hill, Inc. (1973) pp 155-158

1.7. Vlaardingerbroek, *op.cit.* p 27.

1.8. *ibid.* p 28.

1.9. Wehril, "Principles of Magnetic Resonance, Chapter 1", *op. cit.* p11.

1.10 Schwartz, Mischa *Information Transmission Modulation and Noise.* New York: McGraw Hill Book Company, Inc. (1959) pp 103-106.

1.11. Vlaardingerbroek, *op. cit.* p 38.

1.12. Wright, Steven. "Nuclear Magnetic Resonance and Magnetic resonance Imaging". Chapter 16 in John Enderle, Susan Blanchard, and Joseph Bronzino, editors of *Introduction to Biomedical Engineering,* San Diego: Academic Press (2000) p 821.

1.13. Conolly, Steven, A. Macovski, and J. Pauly. "Magnetic Resonance and Imaging: Acquisition and Processing" in Chapter 65.1 in *The Biomedical Engineering Handbook* ed. by Joseph D. Bronzino, Boca Raton, FL: CRC Press (1995) pp 1010.

1.14 Conolly, *ibid.* p1010.

1.15 Suetens, Paul. *Fundamentals of Medical Imaging*, Cambridge, UK: Cambridge University Press (2002) p 112.

1.16. Schneck, John. "Magnetic Resonance and Imaging: Hardware/Instrumetation" in Chapter 65.2 in *The Biomedical Engineering Handbook* ed. by Joseph D. Bronzino, Boca Raton, FL: CRC Press (1995) pp 1014-1020.

1.17. Matwiyoff, N. A. "Instrumentation, Chapter 3" in David D. Stark and William G. Bradley, editors. *Magnetic Resonance Imaging* St. Louis: Mosby Year Book, p 71. (© 1992).

1.18. Hayes, C.E., W.A. Edelstein, J. F. Schenck, *et. al.* "An efficient highly homogeneous radiofrequency coil for whole body

NMR imaging at 1.5 T. *Journal of Magnetic Resonance,* 63:622, (1985).

1.19. Haase A., Frah J, Matthaei D, *et al.* FLASH imaging: rapid NMR imaging using low flip angle pulses. *J Magn Reson* 1986;67:258-66.

1.20. Wehrli, Felix W. *Fast-Scan Magnetic Resonance: Principles and Applications.* New York: Raven Press Ltd. (1991) pp. 10-21.

Engineering Data from Vlaardingerbroek:

- Ball park figures for saddle coils: L = 200μH; coil sensitivity G/I = C = 30 A(mT/m)$^{-1}$. Field gradient 12 mT/m. Rise time 0.6 ms, peak power 43 kW (p 28).
- DC magnetic field homogeneity: better than 5ppm. (p 12)
- Superconductor wire: niobium titanium alloy superconductive below 12 K. Liquid Helium 4.3K. (p 18)
- Prism Magnet: 0.15 T, gap .7 m, length 1.05 m, total weight 3400 kg. Permanent magnetic material NdBFe (33%) and iron yoke (60%). (p 22)
- Magnetic homogeneity of less than 5 ppm within a 50 cm sphere (p 24)
- Spine may require 50 cm maximum length FOV and penetration depth 16 cm. (p. 38)
- MRI signals have a dynamic range of about 8 X 10^{15} at 1.5 T and 10^{15} at .5 T. (p 40)
- Echo time 10.8 ms. (p 68)

FURTHER INFORMATION ON MRI FROM THE WEB

---

http://www.cis.rit.edu/htbooks/mri/
The Basics of MRI, J. P. Hornak

This is a book of 14 chapters by J. P. Hornak of Rochester Institute of Technology on the MRI. Quite comprehensive and widely referenced.

Http://www.t2star.com/modules/MR_Image_Contrast.pdf

"MR Image Contrast", William Faulkner, 1997

Excellent 12 page text on T1 and T2 relaxation and its effect on the image, from an operator's prespective. He shows how the operator can varry TE and TR to make T1 or T2 weighted images. Spin-echo pulsing sequence discussed.

Http://www.mri.jhu.edu/~sreeder/pdf_papers/mse_t~va.pdf

"Development of High Speed, High Resolution Tagging Techniques". By Scott Reeder, Advisor Elliot McVeigh

A graduate thesis out of Johns Hopkins University, Baltimore, Maryland; a 198 page document in full text.

This thesis now requires permission to access.

Http://www4.ncsu.edu/eos/users/w/wes/homepage/MRI/mrilesso.html
"Magnetic Resonance Imaging: A Short introduction for clinicians" by Wesley E. Snyder.

This is an MRI clinician's lecture in complete text with simple diagrams and superficial equipment ideas. He explains T1 and T2 weighting as a user method; shows how TE and TR choices result in T1 or T2 weighting.

Http://www.gehealthcare.com/gecommunity/mri/ortho/ortho_apps-techniques.html

MRI Techniques for Orthopedic Imaging, Cynthia F. Maier, Lewis Lauzon, Ramish Venkatesan
GE application note for FSE TIMING SEQUENCE

A seven-chapter industrial application note directed to orthodontics, relevant to General Electric MRI equipment. Various chapters discuss the CHESS timing sequence, and features of interest to the clinician.

---

http://mrel.usc.edu/class/articles/Riederer-MRI2000.pdf
"Current Technical Development of Magnetic Resonance Imaging"
Stephen J. Riederer. *IEEE Transactions Engineering in Medicine in Biology. (September/October, 2000).*

This is an IEEE review article in complete text about the status of MRI in 2000 by Riederer of the Mayo Clinic, a prolific expert in this field.

Http://www.uib.no/med/avd/miapr/arvid/bfy-361/howseman_bowtell1999.pdf

"Fuctional Magnetic Resonance Imaging:Imaging Techniques and Contrast Mechanisms" Alistair M. Howseman & Richard W. Bowtell. Philosophical Transactions of the Royal Society of London, vol 354, pp 1179 - 94.

The paper is given in full text.

Exercises

Student end-of-chapter exercises and a solutions manual for instructors are available at ABC engineering research, 33 Barney St. Wilkes-Barre, PA, U.S.A. 18702. (astonrj@yahoo.com).

CHAPTER 2

X-RAY, BASIC THEORY

NOTE: This material is for educational purposes only. See the disclaimer above.

Various particles and waves emerge from the atom. Early evidence of this was discovered by Thomas Edison when he put a plate of metal in a light bulb and placed it at a positive voltage with respect to the tungsten filament. It drew a current, called the Edison Effect. It was not known then that these were electrons, but was investigated as cathode rays. One of these investigators, The German Physicist, Wilhelm Conrad Röntgen investigating the florescence cause by these rays, on November 8, 1895, noticed a screen covered with barium platinocyanide glowed when brought near the cathode ray tube, but not in the path of the cathode rays. Serendipitously, he changed the focus of his investigation and studied these mysterious rays, he named x-rays. Most importantly, and amazingly, he also noticed that when he put his hand in the path of the rays, an outline of his bones appeared on the barium plantinocynide screen. He quickly published this and other properties: x-rays could pass through a thousand-page book and three and one half millimeters of aluminum. It was soon discovered these rays could be collimated by pin holes in lead sheets and develop photographic film. This led to techniques so that x-rays could be used to image bone without disturbing the skin, and in fact were used to diagnose broken bones and find foreign objects in the body such as swallowed metal and bullets. Thus radiography was invented.

The modern x-ray vacuum tube, illustrated in Figure 2.1, was invented by W. D. Coolidge in 1913, making possible the production of x-rays at higher energies, produced by anode voltages in excess of 50,000 volts.

X-ray Production

X-rays are produced as a result of the bombardment of an atom by an electron or other atomic sized particles or photons. They are produced in nuclear reactors, and are emitted from stars. But almost all medical x-rays are produced by vacuum tubes.

The voltage, V_F , in Figure 2.1 drives a current into a filament, which, in turn heats the cathode of a vacuum tube. Electrons boil off the cathode, and are attracted by the voltage, V_A. They accelerate to a high velocity and penetrate the anode. The interaction of the electron with the atoms of the anode, often tungsten, transfers the kinetic energy of the electron to an x-ray photon, which emits from the anode.

The energy of the x-ray photon cannot exceed the kinetic energy that the electron acquires as it falls through voltage, V_A. The intensity of the x-ray is measured by the number of photons per second. Since each photon is produced by an electron, the intensity of the x-ray is controlled by adjusting the electron beam current.

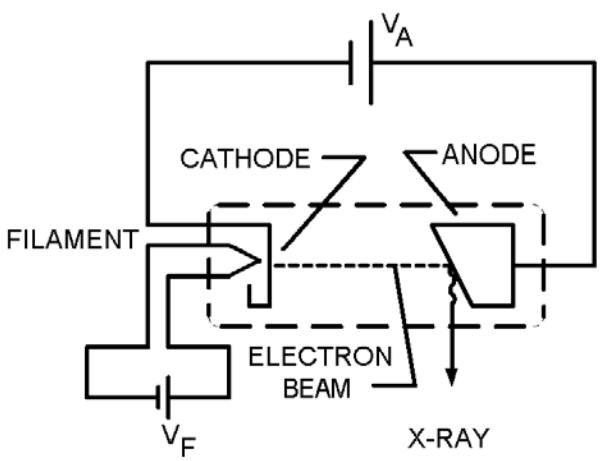

FIGURE 2.1. X-RAY VACUUM TUBE

X-ray Tube Current

The cathode in Figure 2.1 is made of a metal such as tungsten. The heat from the filament agitates the electrons so they acquire enough energy to boil off the metal into the air. An electron leaving the surface will produce a positive charge there which pulls the electron back in. However the voltage V_A, if large enough, will pull it out and accelerate it toward the anode, creating what is called a thermonic current. The higher the temperature of the metal cathode, the greater the current. The

formula for the beam currrent, I_B, has been derived using quantum mechanics as [2.1]

$$I_B = C_0 A_C T^2 e^{\frac{-11600\ E_W}{T}} \qquad (2.1)$$

Here T is the absolute temperature in degrees kelvin, C_0 is the cathode material coefficient, A_C is the area of the cathode in square meters, and E_W is the work function in electron volts for the metal in the cathode. This is the current that would flow if V_A is so high that every electron that boils off the cathode is attracted to the anode. X-ray tubes are designed so this is the case, thus Equation (2.1) gives the current in an x-ray tube. Equation (2.1) shows that the current increases with filament temperature and the area of the cathode, and decreases for larger work functions.

C_0 varies for different cathode materials. The work function, E_W, is a measure of the electrostatic force required to pull an electron from the surface of the

TABLE 2.1

Material Coefficients and Work Functions

Emitter	C_0 amp/(m^2 °K^2)	E_W, eV
Tungsten	60×10^4	4.52
Thoriated-tungsten	3×10^4	2.63
Oxide-coated	0.01×10^4	1

metal. Seely gives a table of values for these constants for commonly used cathode materials, as listed in Table 2.1.[2.2]

These values can be used to generate current versus temperature curves for x-ray tubes having either tungsten, thoriated-tungsten, or Oxide-coated cathodes. The calculation in Figure 2.2 was done by programing Equation (2.1) on a graphics calculator, showing the cathode current for a tungsten versus a thoriated tungsten cathode, of 1 cm^2 area and using the values in Table 2.1. Clearly, the thoriated tungsten cathode produces a beam current at a lower temperature.

X-ray Characteristics

The electron beam in the tube of Figure 2.1 impacts the anode. Most of the electrons enter the anode metal and are stopped, creating heat. About one percent, however, create x-rays when the incoming electrons encounter the atoms. In Figure 2.3, we illustrate two types of x-ray radiation, *characteristic* and *bremsstrahlung*.

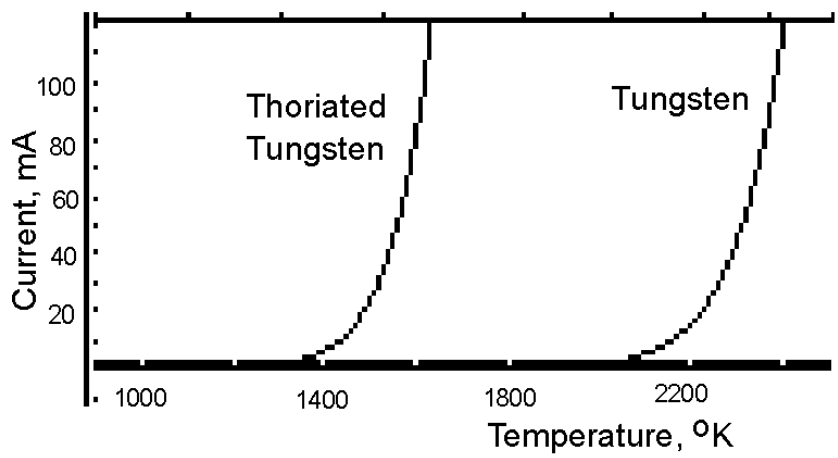

Figure 2.2. Thermal current in an x-ray tube, area 1 cm^2 cathode.

To produce characteristic radiation, the incoming electron collides with an orbital electron in the anode atom. The orbital atom gets knocked to a higher orbit, having absorbed energy from the incoming electron, as illustrated in the top of Figure 2.3. It remains unstable, until it returns to its original orbit, releasing its energy in x-ray *characteristic* radiation. Characteristic radiation emits at a specific energy level, depending upon the atom type in the anode. The energy level is determined by the energy gap between electron orbits in the atom. *Bremsstrahlung* radiation is more like noise, and appears in a band of energy levels. It is caused when the incoming electron is deflected by the atom and slowed down, transferring its kinetic energy into x-ray radiation.

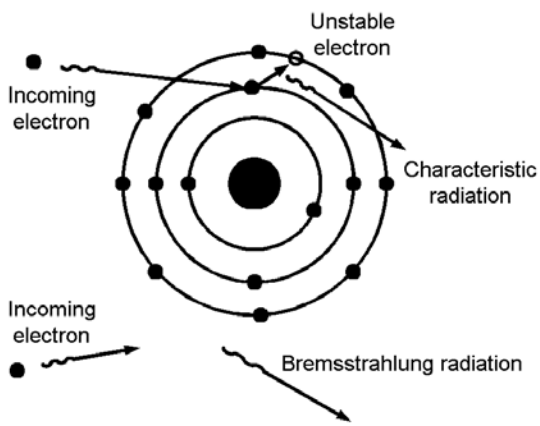

FIGURE 2.3. X-ray produced by electron interactions.

The difference between characteristic and bremsstralung radiation is illustrated in Figure 2.4. Because bremsstralung radiation is caused by collisions of various types, the energy of the x-ray photons released follows the distribution indicated by the curve. The spike on the curve indicates the characteristic radiation, and its specific value is determined by the energy gap between electron orbits. It is caused by very few photons, compared to bremsstrahlung radiation, which contains the majority of the energy in the x-ray. Bremsstrahlung radiation is most important in medical x-ray, and characteristic radiation can be neglected - it being more important in crystallography. Since the bremsstrahlung radiation picks up its energy from the individual electrons in the x-ray tube beam, the energy of each photon cannot exceed the that of those electrons. The energy in an electron in the beam, E_E, is determined by the applied voltage, V_A, in Figure 2.1 as:

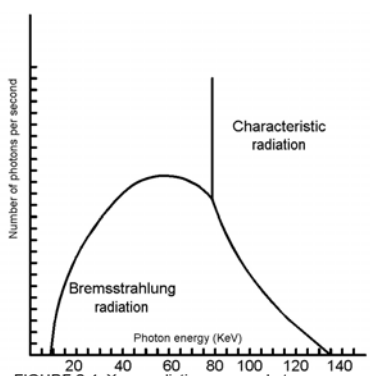

FIGURE 2.4. X-ray radiation versus photon energy level

$$E_E = e\,V_A \qquad (2.2)$$

where e is the charge on an electron (e = 1.602 x 10^{-19} coulomb), and V_A is the voltage on the anode of the x-ray tube. The units in Equation (2.2) are

$$coulomb\ x\ \frac{joules}{coulomb} = joules$$

The units may also be referred to as electron volts, where one electron volt is the energy acquired by an electron as it falls through one volt (1.602 x 10^{-19} joules), as is clear from Equation (2.2).

The energy of an x-ray photon, E_P, is proportional to its frequency, f, and was given by Max Planck as

$$E_P = hf \tag{2.3}$$

where h is plancks constant (h = 6.626 x 10^{-34} joule-seconds).

EXAMPLE 2.1. In Figure 2.4, The maximum energy of an x-ray photon is given as 135 keV. What is the maximum frequency of an x-ray photon. f

SOLUTION

The maximum energy in joules is

$$E_{Max} = 135\,keV\ x\,1.602\,x\,10^{-19}\,coul$$

$$= 2.162\,x\,10^{-14} joules$$

Thus Equation (2.3) can be used to find the maximum frequency

$$\mathrm{f} = \frac{E_P}{h} = \frac{2.162\,x\,10^{-14}}{6.626\,x\,10^{-34}} = 3.26\,x\,10^{19}\ \mathrm{Hz}$$

Notice here that the maximum energy of a photon is equal to the anode voltage in units of electron volts.

Since an x-ray photon is electromagnetic radiation, its wavelength, λ, is given by

$$\lambda = \frac{c}{f} \tag{2.4}$$

where c is the velocity of light (3 x 10^8 m/s), and f is the frequency in hertz. Thus in Example 2.1, the minimum wavelength of the radiation is 3 x 10^8/3.261 x 10^{19} = 9.20 x 10^{-12} m.

Planar X-ray

Throughout the twentieth century, planar x-ray images were created by passing x-rays through the patient as shown in Figure

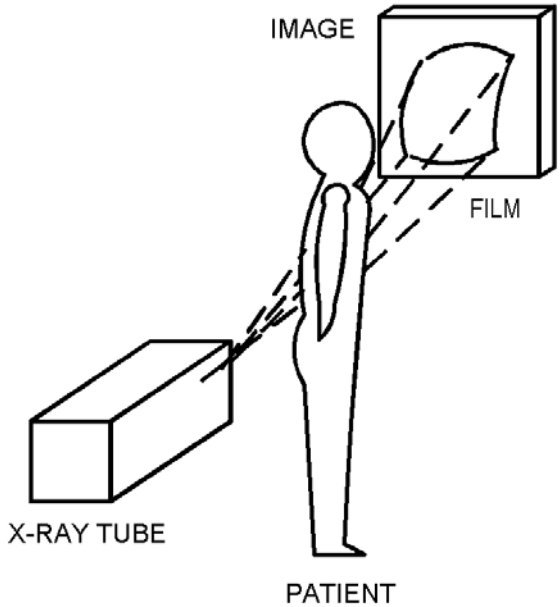

FIGURE 2.5. PLANAR X-RAY

2.5. X-rays from the tube pass through the patient and are absorbed at different rates depending upon what tissue they pass. Bone for example absorbs far more x-ray that soft tissue, and so would appear as a shadow on the film. In order to be precise about how the image is formed we need to analyze how x-ray is absorbed by biological tissue.

Image Production

The planar image is produced because tissue absorbs x-ray at different rates, just as light is absorbed differentially by different materials. Glass is transparent to light, whereas, metal is opaque to light. The differences are made precise by Lambert's Law. He stated that light is absorbed in proportion to the thickness of the material. For x-ray, Lambert's law states that the fractional change in x-ray intensity as it passes through a tissue is proportional to the thickness of the material. In mathematical terms this is:

$$\frac{\Delta\Psi}{\Psi} = -\mu\,\rho\,\Delta x$$

where Ψ is the x-ray intensity in watts per square meter, Δx is the thickness of the tissue and the proportionality constant is $-\mu\rho$. A detailed discussion of this proportionality constant will follow. Taken to the differential limit, this equation becomes

$$\frac{d\Psi}{dx} = -\mu\rho\,\Psi \qquad (2.5\text{ a})$$

The solution to this equation,

$$\Psi = \Psi_0\, e^{-\mu\,\rho\,x} \qquad (2.5\text{ b})$$

is verified by substituting it into Equation (2.5a), and showing the equality.

Mass Attenuation Coefficient

As x-ray photons pass through a tissue, they are reduced in intensity, by being absorbed according to Equation (2.5b). The absorption increases with the density of the tissue, ρ, because the greater number of atoms per unit volume increases the chance of a collision and subsequent absorption of an x-ray photon. Approximate values of this density for common tissue types are given in Table 2.2.

The absorption of an x-ray photon is also dependent upon its energy level as expressed by the mass attenuation coefficient, μ. Values of μ for several common biological tissues is given in Table 2.3. [2.3] There μ most often decreases with increasing photon energy. Above 200 keV, the values do not differ greatly among the tissues listed. At these energies the absorption is determined mostly by the tissue density.

TABLE 2.2.
Density of common biological substances

SUBSTANCE	DENSITY (g/cm^3)
Air	0.0013
Water	1.0
Muscle	1.06
Fat	0.91
Bone	1.85

TABLE 2.3. Mass Attenuation Coefficient Versus Photon Energy

X-ray Photon Energy (keV)	Mass Attenuation Coefficient , μ (cm^2/g)			
	Water	Air	Compact Bone	Muscle
10	4.89	4.66	19.0	4.96
15	1.32	1.29	5.89	1.36
20	0.523	0.516	2.51	0.544
30	0.147	0.147	0.743	0.154
40	0.0647	0.640	0.305	0.0677
50	0.0394	0.0384	0.158	0.0409
60	0.0304	0.0292	0.0979	0.0312
80	0.0253	0.0236	0.0520	0.0255
100	0.0252	0.0231	0.0386	0.0252
150	0.0278	0.0251	0.0304	0.0276
200	0.0300	0.0268	0.0302	0.0297
300	0.0320	0.0288	0.0311	0.0317

EXAMPLE 2.1. An x-ray intensity, produced by a tube having 40 kV on the anode, of 1 W/m^2 is incident on two adjacent tissues, muscle and bone. Plot the intensity of the x-ray in both as they progress through the tissue in the x-direction.

SOLUTION

The x-ray photons have a maximum energy of 40 keV, so we take μ for bone as 0.305 and for muscle as 0.0677 in Table 2.3. From Table 2.2 the densities are 1.85 and 1.06 respectively. A plot of Equation (2.5), on your graphics calculator, with these values is given in Figure 2.6:

FIGURE 2.6. Intensity of x-ray as a function of position in bone and muscle tissue

It is clear in Figure 2.6 that x-ray is absorbed more in bone than in muscle. This is due to the large difference in their densities and mass attenuation coefficients. The x-ray which emerges from the x-ray on to the film is very different in intensity from bone an muscle. This makes for good contrast in x-ray images of bone imbedded in muscle. Blood clots and fluids would make images with good contrast because of the wide difference between the density of lung tissue and muscle or blood, since lung contains a lot of air, having a low density as indicated in Table 2.2. Medical x-rays usually use tube voltages ranging from 20 kV to 200 kV, in part because the values of mass attenuation coefficients get low and undifferentiated at higher photon energy levels, as shown in Table 2.3.

X-Ray Hardware

The x-ray tube is the heart of any x-ray unit. It is where the x-rays are generated, and is an expensive part that wears out and must be maintained and replaced periodically. Difficulties associated with it are due to the fact it uses high voltages and must dissipate a lot of excess heat. The heat arises from the inefficiency of the process by which x-rays are generated.

The efficiency of an x-ray tube, η, is equal to the ratio of the power in the x-ray beam to that in the beam of electrons. The power of the x-ray beam, P_X, increases as the square of voltage on the anode, V_A ,because the higher voltage means the electrons are going faster and penetrate deeper into the anode, increasing their chance of colliding with an atom. It also increases with the beam current, I_B, since this means more electrons are available to collide. A large the atomic number, Z, also increases the probability of collision [2.4]. The net result is:

$$P_X = k\, I_B\, Z\, V_A^2$$

where k is an empirical constant, measured as $k = 1.4 \times 10^{-9}$.
The power in the electron beam, P_B, is the product of the voltage and current as:

$$P_B = I_B\, V_A$$

The x-ray tube efficiency is then the ratio of these two quantities

$$\eta = k\, Z\, V_A \qquad (2.6)$$

For the case of a tungsten cathode, (Z = 74) in a tube operated at V_A = 100 kV, this efficiency calculates to 1.04%.

In general the efficiency of x-ray production is about one percent, and as a result, most of the energy of the electron beam is converted to heat which must be dissipated by the vacuum tube. Several techniques for doing this are illustrated in Figure 2.7.

The X-Ray Tube

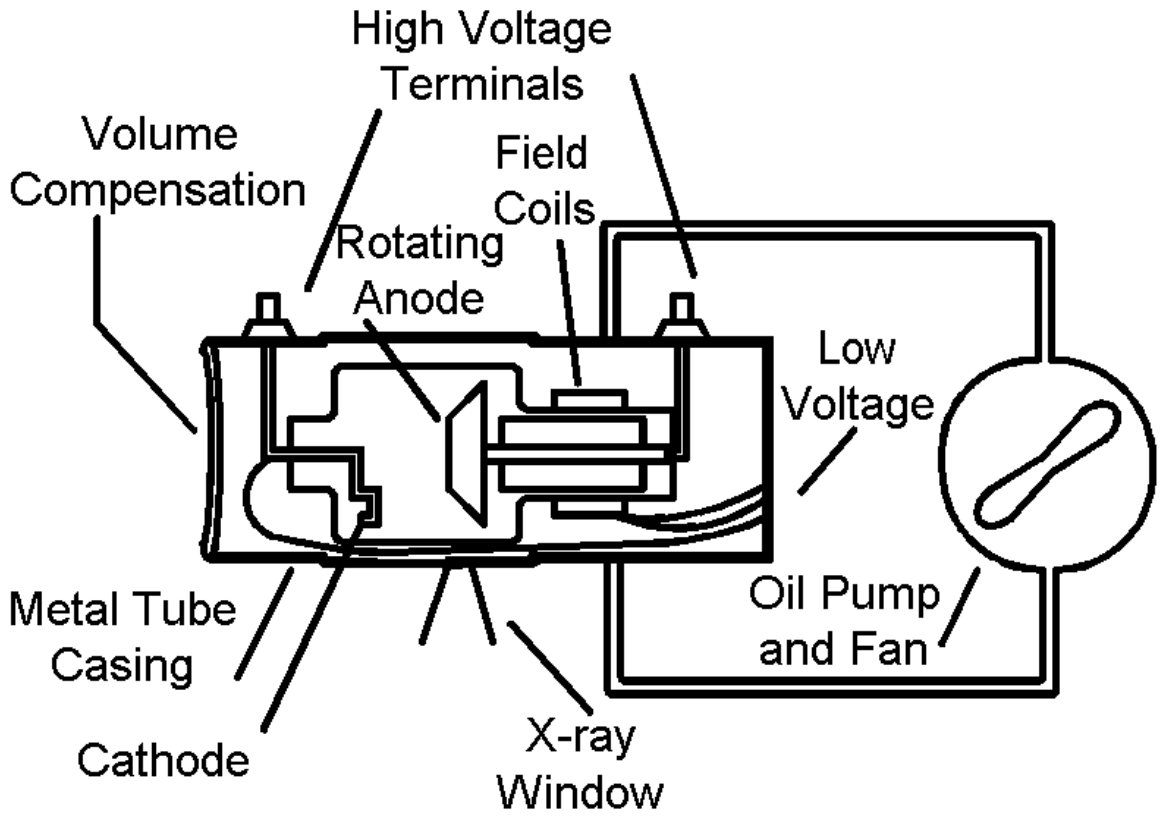

FIGURE 2.7. AN X-RAY TUBE IN ITS CASING

Two mechanisms for dissipating heat are the rotating anode and circulating oil around the tube. The anode rotates between 3600 and 10000 rpm, driven by a motor with field coils exterior to the tube, and an armature interior to the tube. This spreads the impacting electrons over a large area of the anode. The oil is circulated with a pump and cooled with a fan in large tubes. The high tube voltages between 20 and 200 kV are insulated with high voltage terminals. Volume compensation is used to adjust the size as the oil expands when heated. The metal casing around the tube blocks any x-ray from spraying around the room. The x-ray is directed through a glass window toward the patient being imaged. Fabrication of an x-ray tube is very labor intensive making it cost more than one would expect, into the thousands of dollars. The life of the tube can be extended if the operator is careful not to over heat it.

To prevent thermal damage to tube parts such as the cathode and anode, the exposure time for an image often must be limited. A hypothetical characteristic curve for an x-ray tube, Figure 2.8, shows that longer exposure times require lower beam current, I_B, for any particular anode voltage, V_A. That is, the higher the electron beam power, the hotter will becomes the tube. To prevent overheating, the time the tube is turned on must be

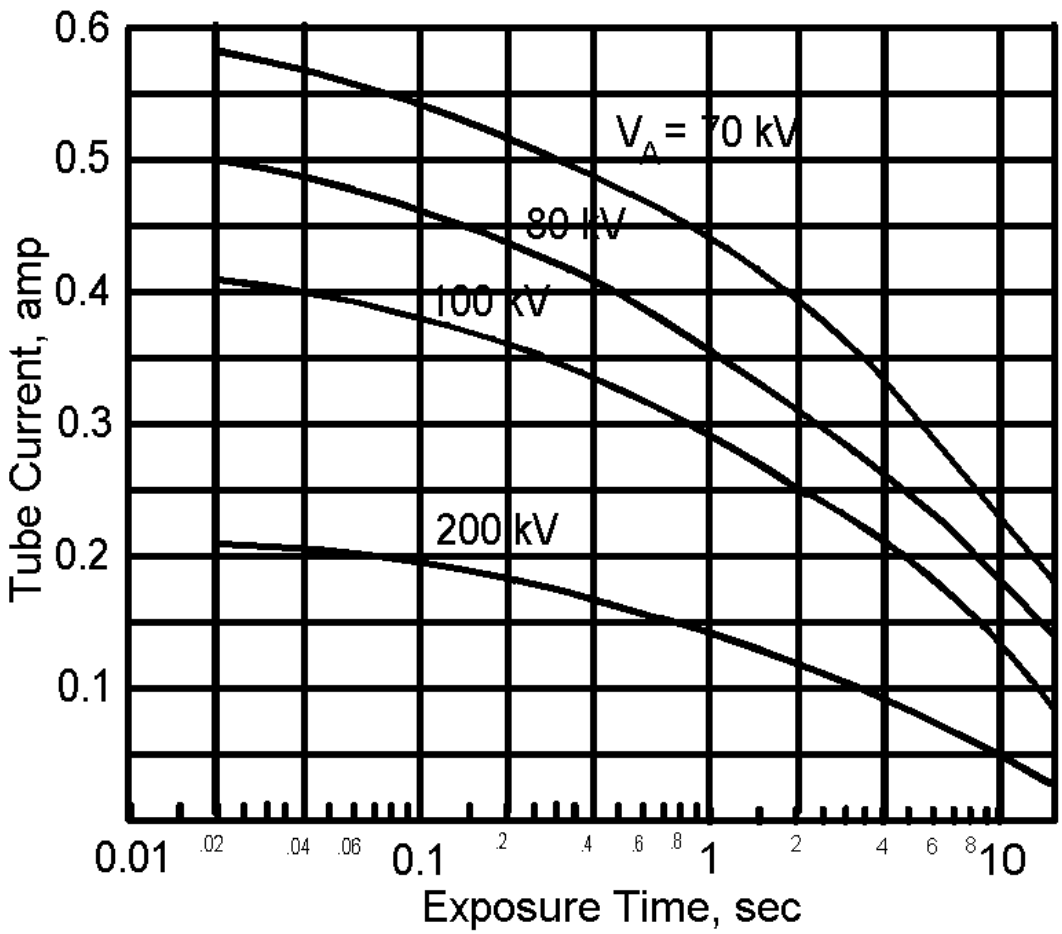

FIGURE 2.8. X-ray tube exposure time limit

limited. For the tube illustrated, if the current is 0.2 A and the anode voltage is 100 kV, the maximum exposure time is approximately 5 seconds, according to Figure 2.8.

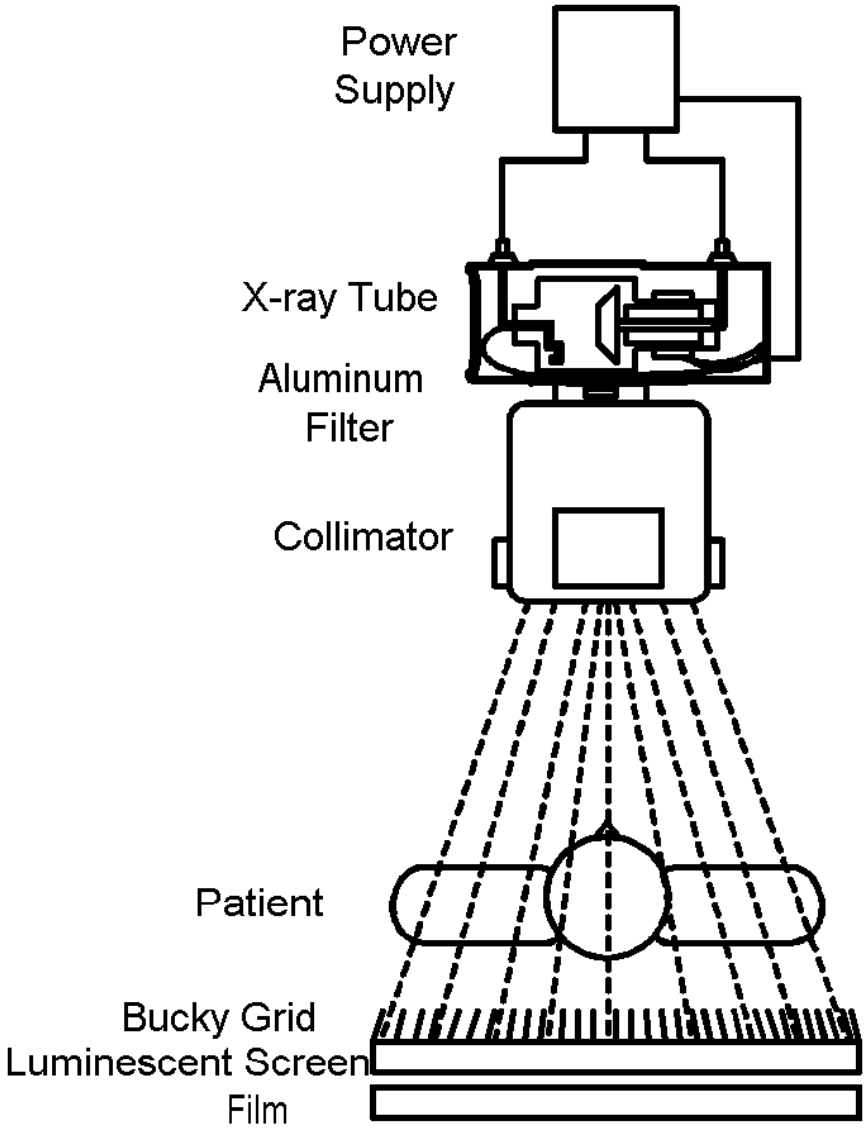

FIGURE 2.9. Planar X-ray Parts

Beam Shaping Parts

The essential elements of a planar x-ray unit are shown in Figure 2.9. The power supply must provide up to 200 kV to the x-ray tube. X-rays which emerge from the tube are first passed through an aluminum sheet which filters them, reducing the number of low energy photons which enter the patient. These photons add to the dose of ionizing radiation, but do not help the image much because they are strongly absorbed by the tissue. The collimator places vanes in the way of the x-ray to absorb energy that would miss the target being imaged and only contribute to more dose for the patient. The bucky grid absorbs the x-ray that has been scattered in the patient, and prevents it from causing unsharpness in the image. It is placed against a luminescent screen which converts the x-ray to light which can develop the x-ray film to produce the image.
The collimator, illustrated in Figure 2.10, casts the x-ray beam on the desired area of the patient's anatomy.

The beam consists of both x-ray and visible light from illuminator tubes, so the operator can see where the beam is striking the patient. The adjustable baffles block unwanted radiation, thus reducing the dose of ionizing radiation to the patient.

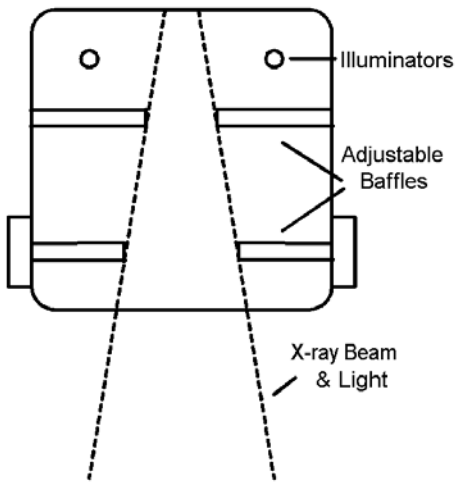

FIGURE 2.10. The Collimator

X-ray Detection

As the x-ray has passes through the patient it becomes selectively attenuated, depending upon the tissue. Thus the x-ray intensity emerging from the patient varies across the plane perpendicular to the rays, giving the information for the image. The quality of the image is degraded by scattering of the x-ray in the patient, interference from the Bucky grid, and blurring in the detector. The process of detection is illustrated in Figure 2.11.. The scattered x-rays are caused when the direct x-ray photon is deflected by an atom in the tissue. When it is scattered it is knocked off its path so that it would not hit the film in a place collinear with the direct ray, and would cause an error in the image. The purpose of the Bucky grid is to absorb this x-ray in its heavy metal, lead or tungsten, vanes. The vanes of the grid then block some direct x-rays as well, because they have a finite width. This can be compensated for, to a degree, by mechanically shifting the grid during the exposure.

After passing through the grid, the x-rays enter a heavy metal screen containing a luminescent material such as phosphor. These heavy metals have high valence, Z, atoms which capture more x-rays, so the screens are called Hi Z. The x-ray is then converted to light. The light then hits the film where it is detected. The film is sensitive to both x-ray and light, but most x-ray would pass through the film. The purpose of the illuminating screen is to capture more x-rays, both before they hit the film, and after they pass through the film. This increases the capture efficiency of the film detector. The conversation of x-ray to light causes some degradation in image resolution due to the blurring illustrated in Figure 2.11. Other solid state detectors are available to detect x-rays and other ionizing radiation. These are discussed in the nuclear medical instrumentation chapter, Table 5.1.

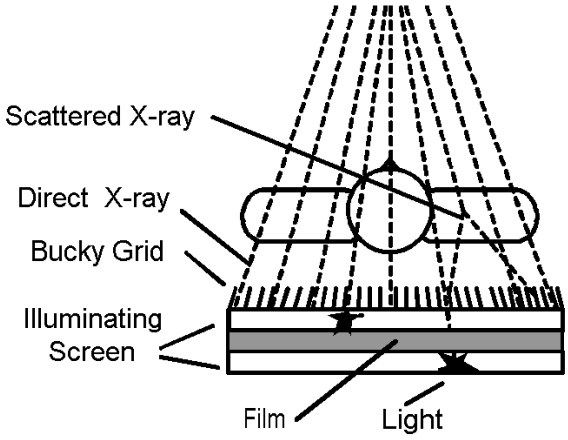

FIGURE 2.11. X-Ray Detection

The Power Supply

The power supply, illustrated in Figure 2.12, must supply high voltage in range from 20 to 200 kV in pulses of varying durations from a few milliseconds to seconds, and in some cases continuously.

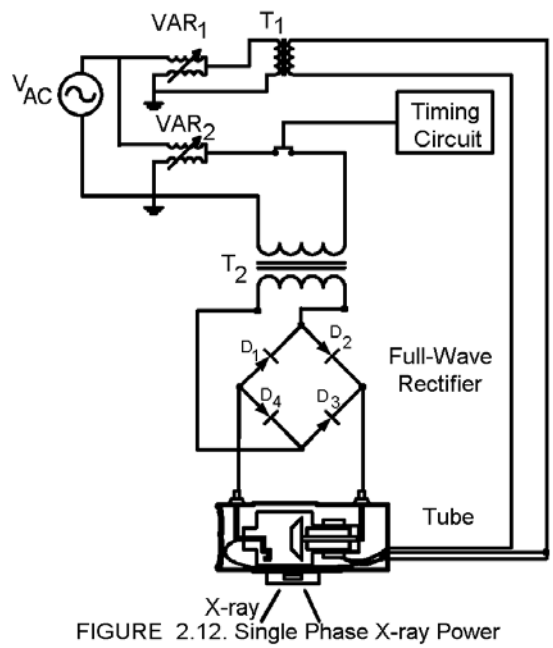

FIGURE 2.12. Single Phase X-ray Power Supply

Adjustment of the x-ray tube beam current is done with a low voltage power supply consisting of varactor VAR_1 and transformer, T_1. Changes in VAR_1 may cause the tube filament temperature to change, thus causing a change in the electron beam current according to Equation (2.1). A separate winding of T_1 may also be used to energize the rotation of the tube anode. A timing circuit is used to turn the x-ray tube anode voltage on and off. It is located on the primary side of T_2 to avoid switching at a high voltage level, which would draw arcs and damage switch contacts. Likewise the anode voltage is varied with VAR_2 on the primary side of the high-voltage transformer T_2. To achieve full-wave rectification, the positive phase of the voltage on the secondary winding of T_2 causes diodes D_2 and D_4 to conduct pushing a positive current from the anode to the cathode of the tube. On the negative phase, diodes D_3 and D_1 conduct. Thus the AC voltage of the source, V_{AC}, is converted to a DC beam current in the x-ray tube.

In summary, in this diagram, the x-ray pulse duration is controlled by the timing circuit and the beam current is controlled

with VAR_1. These quantities are often referred to as the Mas in units of milliamp-seconds. The x-ray photon energy level is controlled by VAR_2 and is referred to as the kV.

People working with the power supply, such as biomedical equipment technologists and clinical engineers need to take high voltage precautions. The voltage breakdown in air at sea level is 75 kV/in. Thus this voltage can jump inches in air and electrocute those who get near the high voltage electrodes in the power supply. Thermal damage to the x-ray tube is prevented by thermal sensors which shut the power supply down when the tube gets overheated.

References

2.1. Seely, Samuel. *Electron-Tube Circuits.* New York: McGraw-Hill Book Company, (1958) p 4.
2.2. *ibid.*
2.3. U. S. Government Printing Office. *Physical Aspects of Irradiation (NBS Handbook No. 85).* Washington DC: (March 1964), p 3.
2.4. Feinberg, Barry N. *Applied Clinical Engineering.* Englewood Cliffs, NJ: Prentice Hall, Inc. (1986) p 245.
2.5 Aston, Richard. *Principles of Biomedical Instrumentaton and Measurement.* Columbus, Ohio: Merrill Publishing Company. (1990).

Exercises

Student end-of-chapter exercises and a solutions manual for instructors are available at ABC engineering research, 33 Barney St. Wilkes-Barre, PA, U.S.A. 18702. (astonrj@yahoo.com).

CHAPTER 3
CT SCANNER THEORY

For educational purposes only. See disclaimer above.

Conventional x-ray records the shadow of anatomical structures on a film. In the 1970's a breakthrough in imaging was achieved with the invention of the Computer Tomography (CT) Scanner, one of a series of devices capable of imaging a transverse slice through the body. These slices can be combined to make a three dimensional picture of the anatomy. The word "tomograph" means "a picture of a slice".

Early forms of tomography were used to make an image of objects hidden behind others. One method of doing this is illustrated in Figure 3.1. The x-ray tube is rotated around one side of the circle and the film follows at the opposite end of a diameter line. A series of pictures is taken on the same film. Each picture will have the object in the center, but the objects off-center will be blurred or averaged away. In some cases this procedure could yield useful diagnostic data, but compared with modern CT scanners it is extremely crude.

The CT Scanner

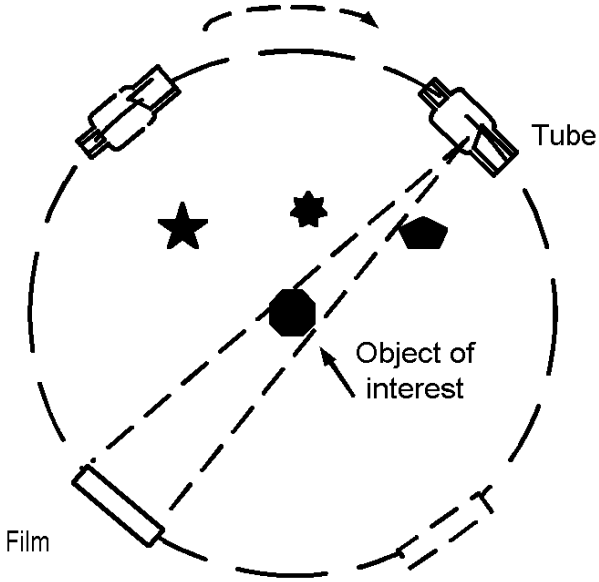

FIGURE 3.1

The CT Scanner, in one form, consists of an x-ray tube that rotates around the patient in a cylindrical opening supported by a gantry, as shown in the top of Figure 3.2. A pencil beam of x-ray, collimated into a single line, passes through the patient to a detector diametrically opposed as illustrated on the lower part of the figure. The detector measures the attenuation of the x-ray beam as it passes through the patient. This data is recorded in a computer. The tube is then rotated a degree or so and the attenuation along another line is recorded. The data is then used by the computer to calculate the x-ray attenuation of each square millimeter of a transverse slice through the patients body, as shown on the lower part of the figure. The attenuation numbers are converted to shades of gray and presented on a computer monitor screen as a picture of a slice of the patient's anatomy.

The process by which the physical data is collected is easy to understand by anyone familiar with conventional x-ray. But the calculation procedure involves advanced mathematics, and would not be practical without modern dedicated computers.

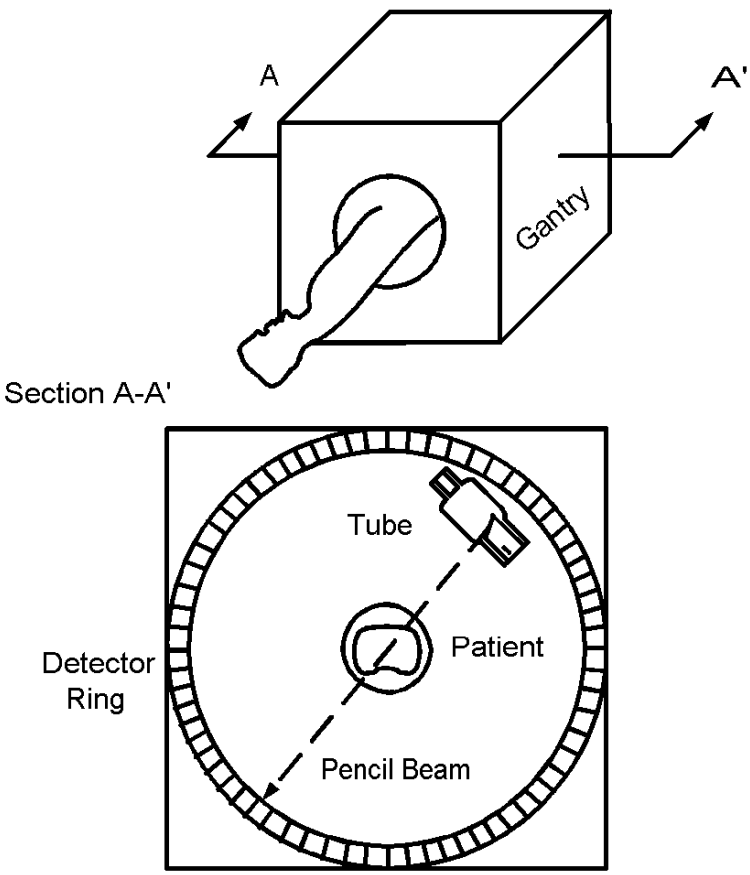

FIGURE 3.2. A CT SCANNER

CT Image Calculation

First the intensity of the x-ray of a pencil beam after passing through a slice is

measured as, $\Psi_\theta(r)$, a

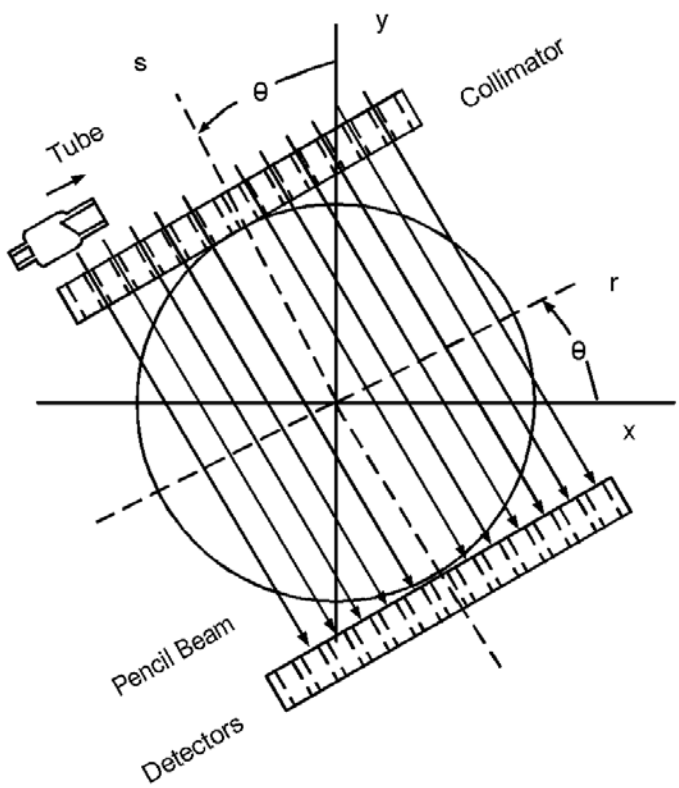

FIGURE 3.3. CT IMAGE CALCULATION

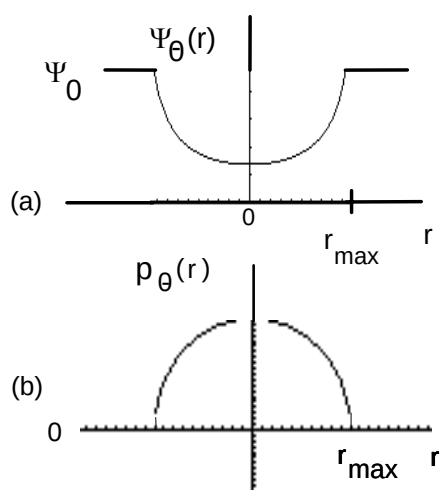

FIGURE 3.4. ATTENUATION PROFILE

function of r in Figure 3.3. The x-ray intensity emerging from the tube is a known quantity, Ψ_0. Thus we can form a function

$$p_\theta(r) = -\ln \frac{\Psi_\theta(r)}{\Psi_0} \quad (3.1)$$

which is called the attenuation profile, $p_\theta(r)$, as a function or r.

To collect this data, one orients the tube, collimators, and detectors as shown in the figure at a specific angle θ_1. The tube is then moved to the right along the collimator, and the detector measures Ψ_θ for each of the pencil beams. These data can be used to form the function $p_{\theta 1}(r)$. Now the whole apparatus is rotated to another angle θ_2 and another set of measurements is taken. This process is continued so that the number of measurements taken would typically be 256 x 256 = 65,536.

As an example calculation of $\Psi_\theta(r)$, consider the medium inside the circle, Figure 3.3, to be uniform of attenuation coefficient $\mu\rho = 1\ m^{-1}$, and the radius of the circle 1 m. Then in Exercise 3.1 we compute the graph in Figure 3.4. Part (a) of the figure shows the x-ray intensity as a function of r on the detectors. And part (b) shows $p_\theta(r)$ for this case. For each value of θ as we rotate the tube-detector pair we have a $p_\theta(r)$ which we can take the polar form of the one-dimensional Fourier transform (1DFT) of, according to the formula

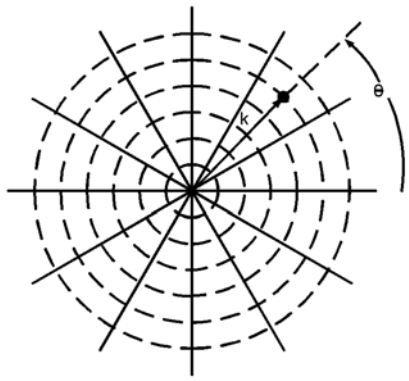

FIGURE 3.5. Polar k-space

$$P_\theta(k) = \int_{-\infty}^{\infty} p_\theta(r) e^{-2\pi i(k\cdot r)} dr \quad (3.2)$$

Here i is the imaginary number $\sqrt{-1}$ and 2πk has the dimensions radians per meter. k is a vector. This formula transforms the spatial quantity p_θ into k-space. This operation can be repeated for each θ value as the tube-detector is rotated through 0 to π radians to yield a two-dimensional function in k-space, P(k,θ). k-space is similar to the frequency domain of the fourier series. The values of k are collected in polar coordinates, and can be plotted is k-space, illustrated in Figure 3.5. The two dimensional Fourier Transform in polar coordinates is: [3.1]

$$p(x,y) = \int_0^{\pi} \int_{-\infty}^{\infty} P(k,\theta) e^{2\pi i(xk\cos\theta + yk\sin\theta)} \mid k \mid dk \quad d\theta \quad (3.3)$$

To create the set of real numbers p(x,y), the computer first integrates on k to create a function of x, y, and θ. It then integrates on θ to create the function p(x,y) which can be mapped as a gray-scale image in rectangular coordinates. In practice we must limit the range on k to a finite number, since the computer cannot go on calculating for ever. A reasonable approximation is achieved if Equation (3.3) is written so that the integration on k goes from -k_{max} to + k_{max} as [3.2]

$$p(x,y) = \int_0^{\pi} \int_{-k_{max}}^{k_{max}} P(k,\theta) e^{2\pi i(xk\cos\theta + yk\sin\theta)} \mid k \mid dk \quad d\theta$$

(3.4)

where

$$k_{max} = \frac{1}{2\Delta r} \quad (3.5)$$

where ▽r is the distance between pencil beams in Figure 3.3, which measures the spatial resolution of the image. The larger the number of k frequencies integrated, the better the resolution. To achieve a 1 mm resolution, k_{max} would equal 500 per meter, for example. The image is an approximation to the ideal because a

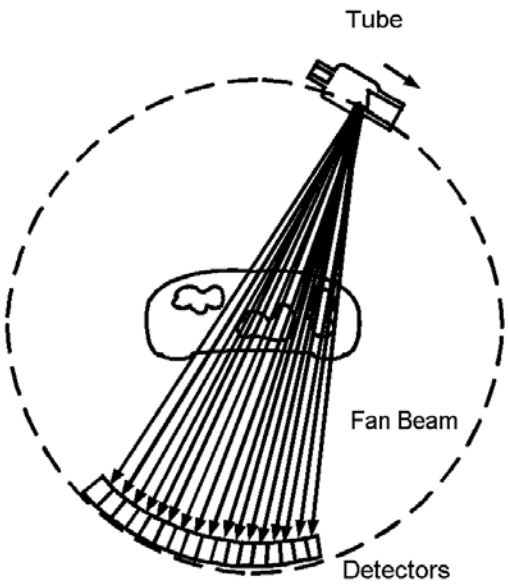

FIGURE 3.6. Third Generation

discrete, finite number of values of k and θ are chosen. Mathematicians over the past quarter century have developed many methods of improving the approximation and the speed with which the calculation can be made by making variations on the basic process of taking the Fourier transform and its inverse as expressed in Equations (3.2) to (3.5). [(3.3)]. The process modeled by these equations is called the filtered back-projection method. The magnitude $|k|$ in Equation (3.4) is called a ramp filter in k-space.

Improving Scan Speed

The first generation of CT scanners used a single detector which followed the tube in a geometric arrangement shown in Figure 3.3.

It took about 5 minutes to create an image of a slice. Byconverting the beam into a fan shape, rather than parallel beams as depicted, that time was reduced to twenty seconds per slice.

A third generation of scanners was developed which eliminated the need to translate the tube, then rotate. In this case the tube would rotate in coincidence with a bank of detectors, around the patient in the center, illuminated by a fan beam as shown in Figure 3.6. The tube and detectors are supported by a gantry. The scan time is reduced to 0.5 seconds a slice with this arrangement, with a consequent reduced x-ray dose to the patient, and it is widely used today.

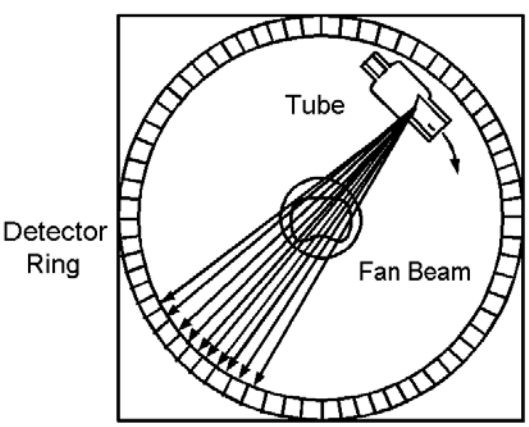

Figure 3.7. The Fourth Generation

The formula for calculating the image from the fan beam is similar to Equation (3.4). See Appendix E, Fan Beam Projection. The derivation of an image formula in terms of practical machine measured parameters is also given there.

Another arrangement, called the fourth generation is illustrated in Figure 3.7. It features a large number of permanent detectors on the outer ring. The use of up to 5000 detectors increases the cost of the equipment, but the mechanical stress on these detectors is reduced. The scan time remains about the same as in the third generation.

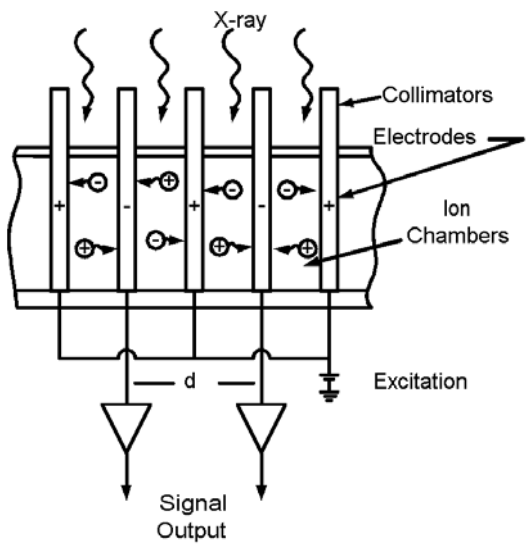

FIGURE 3.8. Ionization Chamber Detectors (From Alker)

X-ray Detectors

The bank of detectors is placed between one half and one meter from the center of the gantry opening. Slow acting film is replaced by instantaneous detectors in the CT scanner, most often of gas ionization chamber or solid state scintillation detector design.

An ionization chamber design is shown in Figure 3.8. The ionization chambers [3.4] are formed between tungsten electrodes. Purified xenon (Xe) gas usually pressurized between 10 and 30 atmospheres absorbs about 60% of the x-rays that enter the chamber. The absorbed x-rays create positive ions and electrons which are attracted to oppositely charged plates to create an output signal current proportional to the incident x-ray. The excitation voltage is chosen so that the output current is proportional to the x-ray incident. The tungsten in the electrodes tends to absorb scattered x-rays, acting thereby as collimators. The distance, d, between the signal output electrodes is about 1.2 mm, insuring an image resolution at that level. The response time of Xe chambers is about 700 μs. The excellent stability of these detectors helps keep the calibration set.

Solid state detectors, such as illustrated in Figure 3.9 can offer better detection efficiency. The scintillating crystal cadmium tungstate ($CdWO_4$) absorbs almost all of the x-ray incident. Modern solid state detectors reach 98 percent conversion efficiency. Both solid state and gas detectors allow scan times better than 2 seconds. The number of detectors used in a CT scanner ranges from 500 to 5000.

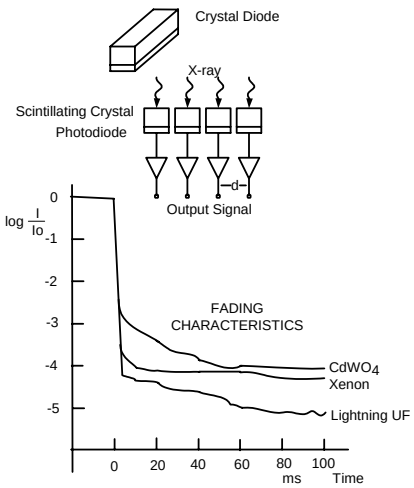

Figure 3.9. Solid State Detector

Solid state detectors generally achieve higher quantum efficiency, and absorb more of the x-ray than xenon, thereby reducing dose and allowing for smaller detectors. The fading characteristics of the detectors determine how quickly the signal reduces so that it can be used again in the next scan. A comparison of $CdWO_4$, Xenon gas, and a compound of Gadolinium Oxygen and Sulfur, GdOS, ceramic (developed as Lightning UFC by Siemens Corporation) appears in Figure 3.9.[3.5] It is important that the solid state detector Lightning UFC has a faster fading time, as it also has higher quantum efficiency and smaller size. This leads to faster and better resolution lower dose CT designs.

Gantry Hardware

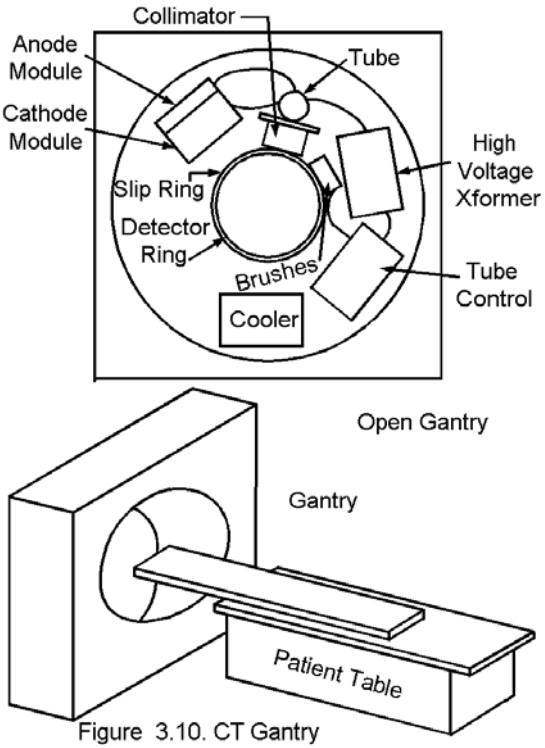

Figure 3.10. CT Gantry

The x-ray tube is mounted inside a gantry, as shown in Figure 3.10. Control voltages and signals are connected through slip rings. The voltage is increased to x-ray levels, near 100 kV, and applied to the tube. X-rays are aimed in the collimator to produce a fan beam, which is detected by detectors mounted on a circular strip around the patient in this case. The cathode module controls the filament current, and the anode module keeps the anode spinning properly. All of this hardware in s rotated with the tube, and so presents a lot of inertia, which limits the speed of scanning. The patient lies on the table and can be positioned in the hole in the gantry as shown in the bottom of the figure.

Fifth Generation CT Scanner

The fifth generation CT scanner, shown in Figure 3.11, creates a focused electron beam which is passed through deflection coils that direct it toward a tungsten target ring as shown.[3.6] The resulting x-rays are directed out of the tube, through the patient onto a detector ring. The electron beam can be scanned around a circle, at electronic speeds, much faster than a massive conventional x-ray tube. In contrast to other approaches, this has no moving parts other than the electron beam. Commercial designs are available which will produce an image in 50 ms, making possible 17 frames per second. Thus, not only breathing artifacts, but the effect of the beating heart blurring the image can be eliminated. One version of electron beam tomography (EBT) has a resolution better than .5 mm, with a slice thickness of 1.5 to 10 mm.

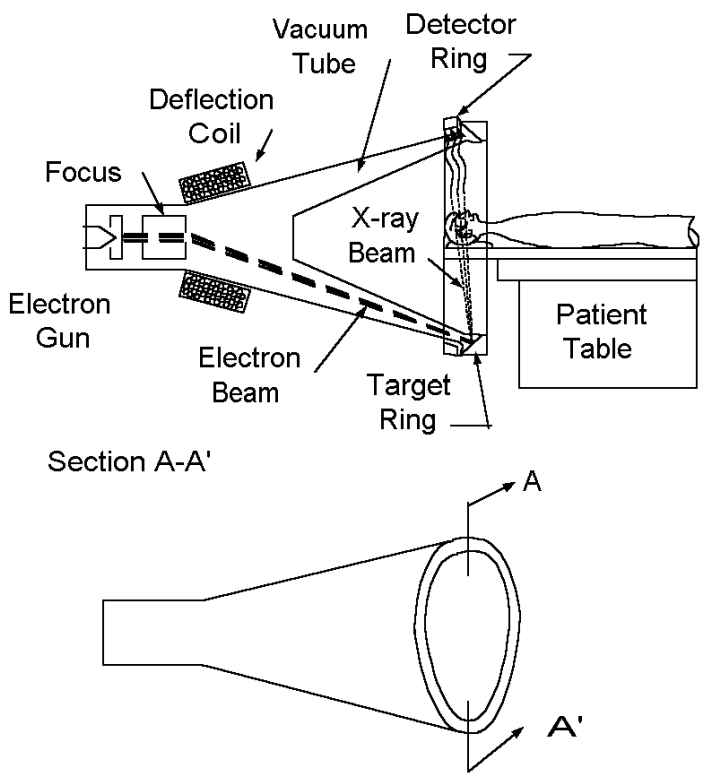

FIGURE 3.11. Fifth Generation CT Scanner

Image Properties

Attempts at theoretical calculation of x-ray contrast based on basic principles, as we did previously,[3.7] are limited by the fact that the attenuation constant, $\mu\rho$, is a function of the energy of the x-ray photon, and the beam contains a spread of energies. That calculation requires one to make a rather arbitrary choice of what energy level to take the attenuation constant. Thus it is common practice to resort to empirical methods to obtain a measure of the contrast between, let's say, kidney and the viscera surrounding it.

A measure of contrast is given by the CT number, CT_n, in the formula[3.8]

$$CT_n = k\left(\frac{\mu\rho - \mu_w\rho_w}{\mu_w\rho_w}\right) \qquad (3.6)$$

where μ_w ρ_w is the attenuation constant of water and k is a proportionality constant. If k is 100 for example, CT_n would represent the percentage difference between the attenuation constant of the tissue in question, $\mu\rho$, as compared to that of water. In practice, k is assigned the value 1000, and the CT_n is called a Hounsfield unit, HU, in honor of one of the inventors of CT.

$$HU = 1000\left(\frac{\mu\rho - \mu_w\rho_w}{\mu_w\rho_w}\right) \qquad (3.7)$$

The least attenuating substance in the body is air, so we arbitrarily assign the number 0 to its $\mu\rho$ value. Thus the HU = -1000 for air. Also, the HU number for water, where $\mu\rho = \mu_w\rho_w$, is 0. At medical energies, around 70 keV, the $\mu\rho$ for bone is approximately 2 times that of water. Thus the HU is taken as HU $\simeq$ 1000. All other normal tissues in the body fall between these values. However if contrast substances are injected, HU may exceed 1000.

Typical values of Hounsfield number for biological tissues are given in Table 3.1.[3.9]

Table 3.1. Typical HU for Biological Tissues

Tissue	**Hounsfield number (HU)**
Dense bone	~1000
Red Blood Cell	93
Spleen	46
Muscle	44
Blood	42
Pancreas	40
Gray matter	38
White matter	30
Heart	24
Cerebral spinal fluid	0-20
Water	0
Fat	-20 to -100
Bowel Gas (air)	-1,000

Notice how close the HU numbers are for spleen, muscle, blood, pancreas are, portending low contrast for these tissues in a CT scan unless absorbing substances are added as contrast agents.

CT Scanner Calibration

A phantom, such as is illustrated in Figure 3.12, is used to test the ability of the CT scanner to distinguish objects of different size, and having different attenuation coefficient, μ, values, expressed as Hounsfield numbers. A set of rods of uniform size are made of different plastics: Teflon (HU = 882), Bakelite (262), Plexiglas (126), Nylon (89), Polystyrene (-28), Octane (-303). A CT image of these rods will appear as different shades of gray, depending on the HU number. Thus the rods can be used to calibrate the HU number that corresponds to a particular shade of gray. They enable one to set the range of HU values that are covered by the shades of gray from white to black. If, for example, internal organs are being imaged, the shades of gray would be set to range from white to black as HU varied from say -100 to 100. If, on the other hand bone was being imaged, white to black might cover HU numbers from 500 to 1500. In this way the contrast of the image can be adjusted.

The objects of diminishing size can be used to measure the spatial resolution of the of the image. The phantom is a known object that can be compared with the x-ray image, so that any distortions can be clearly identified.

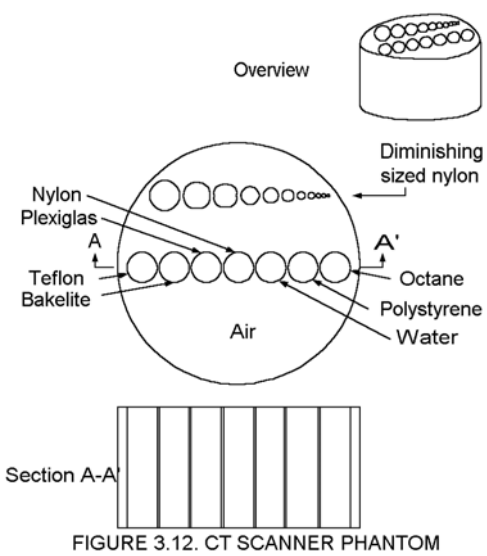

FIGURE 3.12. CT SCANNER PHANTOM

Resolution

The resolution of the image is the smallest distance at which two objects can be distinguished. If two objects are closer than the resolution distance, they will appear as one object on the image. The resolution is limited, in a CT scanner, by the size of the holes in the collimator. the width of the detector.

On the imaging surface, the resolution is limited by the number of pixels per meter in the image. A typical slice size may be 25

centimeters in diameter. The display matrix may be 256 X 256. The horizontal or vertical resolution in this case, R_{CT}, cannot be better than

$$R_{CT} = \frac{250\,mm}{256} = 0.977 \text{ mm}$$

To measure the resolution in x-ray, the concept of modulation transfer function (MTF) pertains.

The MTF grid, shown in Figure 3.13, consists of lead having holes of diminishing size as the fan beam rotates in the counterclockwise direction. When the intensity of x-ray that hits the detectors begins to decrease because of the decreased spacing, the limit on the resolution has been reached. In the case illustrated, the percentage of transfer begins to diminish when the vanes and gaps reach 1 mm. If the intensity has diminished significantly at 2 cycles/mm, the resolution is

$$\frac{1}{2/mm} = .5mm$$

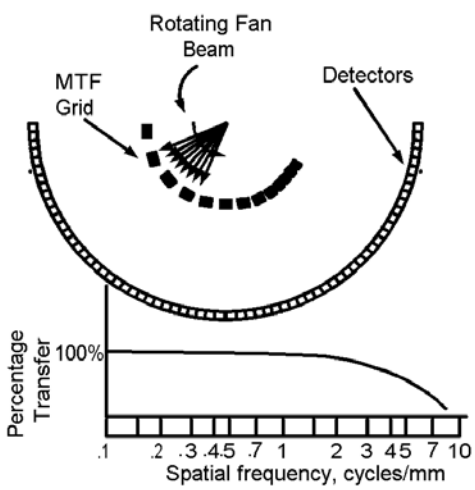

Figure 3.13. Modulation Transfer Function

Patient Dose

The patient dose is the amount of x-ray energy absorbed in the tissue per unit mass, measured in grays (1 J/kg) or rads (.01 J/kg). Each photon of x-ray gives up an amount of energy as it passes through the tissue. Thus an increase in the number of photons, or x-ray intensity, increases the dose in a given mass. The patient dose does not increase when one increases the number of slices in a study, since increasing the number of photons absorbed is balanced by an increase in the mass. However if x-ray scattering occurs, as it inevitably will, the dose of the individual slices increases. The dose is increased if the time to scan each slice is increased, or if the intensity of the x-rays (mAs) is increased.

The dose from a particular CT scanner depends on the manufacturer. The scanners typically run at 120 kV and from 80 to 300 mA. Typical dose levels range from 1 to 8 rads.[3.10] The key to reducing dose is to manufacture more sensitive x-ray detectors, and generate computer algorithms that require shorter duration x-ray exposures per scan. The demand for better resolution tends to increase dose because thinner slices mean less mass per slice, and longer tissue exposure times.

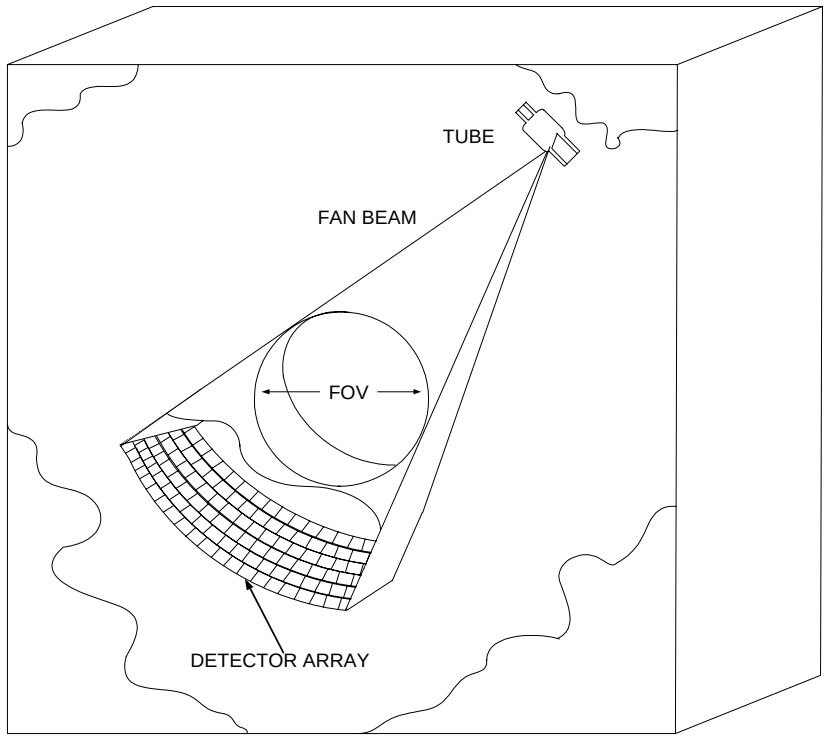

FIGURE 3.14 SPIRAL SCANNER

The Spiral Scanner

The Spiral Scanner was made possible by the introduction of slip rings into the gantry so that the tube and detector assembly, as oriented in the Generation 3 scanner (Figure 3.14) can rotate continuously. Both the electrical power and the signal are transmitted through the slip rings. The patient table is moved slowly through the gantry hole so that the x-ray beam outlines a spiral (helix) on the body being imaged. Each 360 degrees of rotation constitutes a slice. Because of the rapid response time of the detectors depicted in Figure 3.9, it is possible to go through one slice in less than 0.5 seconds. The detectors can be made small enough to allow 0.35 mm spatial resolution, and a slice resolution of 0.4 mm. The detector array in Figure 3.14 may have up to 64 rows. In one study, as many as 800 slices are produced. A 64 slice CT Scanner can scan the entire heart in 10 seconds. If the x-ray is gated with an ECG waveform, an image of the heart in one phase of its beat can be made. For example, one could trigger off the R wave of the ECG on each beat to show the heart in contraction (systole). Introducing a delay into the trigger could produce an image of the heart in relaxation (diastole).

The Spiral Scanner may be used in angiography to view the vessels of the heart. Temporal resolution of 185 milliseconds has been reported. This compares to 20 milliseconds for conventional angiography techniques [3.11]. Although the CT resolution is not as good in this instance, the procedure is much quicker with the CT scanner, measured in the seconds, and it is noninvasive.

The large number of slices produced by the scanner poses the problem of analyzing all of that data. It may produce information overload for a human analyst. Machine data processing may be developed. Combination of many slices into a three-dimensional image also provides diagnostic data.

References

3.1. Suetens, Paul. *Fundamentals of Medical Imaging.* New York: Cambridge University Press, (2002) p 22.
3.2. *ibid.* p 78.
3.3 *op.cit.*
3.4. Alker, George, S. Rudin, D. Bednarek. "Computer Tomography" in John Webster, Editor, *Encyclopedia of Medical Devices and Instrumentation, Volume 2.* New York: John Wiley & Sons, (1988). pp 826-848.
3.5 Günter Hahn, Rolf Hupke, Gerhard Kohl, Jürgen Leppert "Developing an Ultrafast Radiation Detector for CT Scanning" Siemens AG 2001, D-80312 München, (2001) accessed on line May 2005 at <http://w4.siemens.de/FuI/en/archiv/ zeitschrift/heft1_97/artikel03/>.
3.6. Cunnigham, Ian A. & Philip F. Judy. "Computed Tomograpy, Chapter 64" in Joseph D. Bronzino, Editor, *The Biomedical Engineering Handbook.* Boca Raton, FL: CRC Press (1995) pp. 990-1001.
3.7. Aston, Richard. *Principles of Biomedical Instrumentation and Measurement.* Columbus OH: Merrill Publishing Company (1990) p456.
3.8. Alker, *op.cit.* p 833.
3.9. *ibid.* p834.
3.10. Cunnigham, *op cit.* p. 999.
3.11. Becker, "Tailoring contrast administration for cardiac CT" University of Munich, Grosshadern, Germany. Accessed on line May 2005 at<http://www.ctisus.org/cta_web/ 12_04/12_04_Becker/12_04_CTA_Becker.html>.

More Information on CT Scanners from the WEB

---

http://ric.uthscsa.edu/personalpages/lancaste/DI2_Projects_2003/HelicalCT_artifacts.pdf

"Artifacts in helical CT images", Yu-Huei (Jessica) Huang. Good article about the Helical CT scanner, with practical observations and good references. A full text article.

---

http://www.the-infoshop.com/study/go9670_tomography_scanners_toc.html

A major marketing study of CT scanners available at a cost of over 3000 dollars.

---

http://www.ispub.com/ostia/index.php?xmlFilePath=journals/ijmt/vol1n1/pet.xml

Dario B. Crosetto: "A Modular VME Or IBM PC Based Data Acquisition System For Multi-Modality PET/CT Scanners Of Different Sizes And Detector Types." *The Internet Journal of Medical Technology.* 2003. Volume 1 Number 1.

This full text article presents a new design for a combination CT and PET scanner, using a fifth generation CT.

---

http://www.ctisus.org/cta_web/12_04/12_04_Becker/12_04_CTA_Becker.html

Becker. "Tailoring contrast administration for cardiac CT"

This full text article presents clinical applications of the 64 slice CT Scanner.

---

http://www.medical.toshiba.com/news/pressreleases/072704-484.htm

Advertising information from Toshiba about the 64 slice CT.

Another such site form Siemens is:

Http://www.businesswire.com/webbox/bw.092804/242725134.htm

---

http://w4.siemens.de/FuI/en/archiv/zeitschrift/heft1_97/artikel03/

"Developing an Ultrafast Radiation Detector for CT Scanning"

Günter Hahn, Rolf Hupke, Gerhard Kohl, Jürgen Leppert.

An excellent report on developing new detector material for the CT scanner in full text. This is an extensive article on CT scanner detectors from Siemens is important to read. It reviews the state of the art of CT scanner detectors as of 1997 by Siemens researchers: Günter Hahn, Rolf Hupke, Gerhard Kohl, Jürgen Leppert . They conclude lightening UFC is a promising material for solid state detectors.

---

http://www.devicelink.com/mddi/archive/99/05/004.html
A state-of-the art review of CT Scanners, 1999.

---

http://www.isy.liu.se/cvl/ScOut/TechRep/Papers/LiTHISYR2682.pdf
"The MATLAB/C program *take* - a program for simulation of X-ray projections from 3D volume data. Demonstration of beam-hardening artefacts in subsequent CT reconstruction". Olle Seger, Maria Magnusson Seger. Department of Electrical Engineering
Linköping University, SE-581 83 Linköping, Sweden
Email: olles@isy.liu.se, maria@isy.liu.se
March 15, 2005
A demonstration of how to use the mathematics program MATLAB to construct CT images.

---

http://www.sv.vt.edu/xray_ct/parallel/Parallel_CT.html
Raman Rao, Ronald D. Kriz, *et al* "Parallel Implementation of the Filtered Back Projection Algorithm for Tomographic Imaging", Department of Electrical Engineering, Virginia Polytechnic Institute and State University, Blacksburg, Virginia 24061

In this project, they describe a parallel implementation of the filtered back projection algorithm for finding 2D cross sectional images. The results show that parallel processing is very viable for CT reconstruction and results in significant run time savings. They describe an implementation on two different machines: the Intel Paragon and the Connection Machine.

Exercises

Student end-of-chapter exercises and a solutions manual for instructors are available at ABC engineering research, 33 Barney St. Wilkes-Barre, PA, U.S.A. 18702. (astonrj@yahoo.com).

CHAPTER 4
NUCLEAR MEDICAL EQUIPMENT: Part 1, Planar Imaging

For educational purposes only. See disclaimer above.

Nuclear Physics found application in Nuclear Medicine before its applications in electrical power production and in the military. Its use is based on radio nuclides.

A nuclide is a species of atom characterized by the contents of nucleus: its energy, number of protons and neutrons in the classical model. If a nucleus is bombarded by a high energy particle, it can be transmuted to a new element or an isotope of that element. In in this case a new nuclide is formed. When the nuclide is radioactive and emits particles, and is called a radio nuclide. The concept of the isotope is illustrated with a discussion of hydrogen.

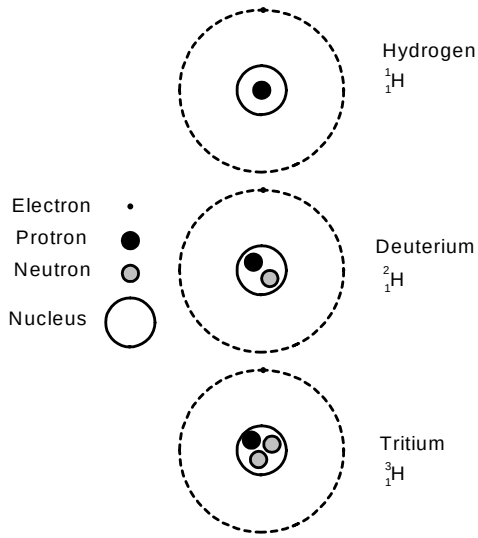

FIGURE 4.1. Hydrogen and Its Isotopes

Hydrogen and its Isotopes

Hydrogen is found in nature in three forms, hydrogen, deuterium and tritium, illustrated in Figure 4.1.

The elements are designated by symbols in the form:

$$^{A}_{Z}X$$

Where A is the mass number, Z is the atomic number, and X represents the element symbol. A is the number of protons and neutrons in the atom. Z is the number of protons in the nucleus. Thus the number of neutrons, N, is given by,

$$N = A - Z \qquad (4.1)$$

The atom is orbited by electrons. In the classical model, the nucleus consists of protons and neutrons, illustrated in Figure 4.1. The mass of a proton is 1836 times that of an electron and the mass of a neutron is nearly the same, 1840 times that of an electron. The mass number A essentially allows you to calculate the mass of the whole atom, since the mass of the electrons is small enough to be neglected. The mass of the atom is approximately :

$$(1840 \times N + 1836 \times Z) \times \text{Mass of an electron.} \qquad (4.2)$$

The mass of an electron is 0.000549 Atomic mass units (amu), (9.1096×10^{-31} Kg, at rest).

Most hydrogen has the symbol shown in Figure 4.1. About 8:1000 parts of all hydrogen in nature appears as Deuterium, with the symbol shown in the figure. Since it has the same number of protons and orbiting electrons as hydrogen, it is an isotope of hydrogen. It therefore has most of the same chemical properties of hydrogen. Tritium is also an isotope of hydrogen. It does not occur in nature but can be artificially produced in a cyclotron, as discussed below.

The Cyclotron

There are several ways of producing nuclides artificially: as a byproduct of nuclear reactions in a reactor such as in a nuclear electrical power plant, in a linear accelerator, Van de Graaff generator, synchrotron, or in a cyclotron. [(4.1)] The cyclotron will be discussed here, since these are often used in the hospital environment.

The cyclotron in Figure 4.2 consists of two hollow vacuum D-chambers and a source, S, of protons generated from hydrogen inserted in a chamber.

The voltage V_F heats a tungsten filament which emits electrons, accelerated by voltage V_A, and which in turn collide with the hydrogen atoms, stripping their electrons. This results in a positively charged proton which is in turn accelerated by the RF generator, and launched into the D chamber. There a magnetic field B, perpendicular to the path of the proton, coming out of the page in Figure 4.2, exerts a force on it according to Ampere's law:

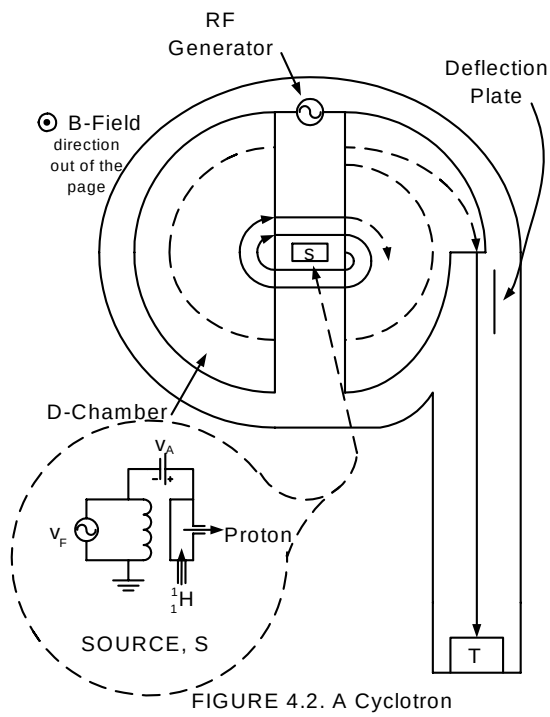

FIGURE 4.2. A Cyclotron

$$f = q v B \qquad (4.3)$$

where q is the charge in coulombs, v is the velocity in meters per second and B is the magnetic field in Tesla (Webers/m^2). The force, f, is perpendicular to the direction of flow, and causes the particle to travel in a circle. (To find the direction of f by the right-hand rule, place your right-hand fingers in the direction of the velocity of the positive charge. Roll your fingers in the direction of the B-field, and your extended thumb will point in the direction of the force on the charge.) The mass, m, of the proton thus experiences a centripetal force (4.2) given by

$$f = \frac{m v^2}{r}$$

where r is the radius of the circle. These two forces must be equal, so:

$$qvB = \frac{mv^2}{r}$$

Solving for the radius r yields,

$$r = \frac{mv}{qB} \tag{4.4}$$

The RF generator is of such a frequency that when the particle has traversed a half-circle, it changes polarity so that as the particle enters the gap between the two D-chambers it is accelerated in the gap. In the second D-chamber, it follows a larger circle because it is going faster. That causes it to follow a spiral path as shown in Figure 4.2. The angular velocity, ω, of the particle, from Equation (4.4) is,

$$\omega = \frac{v}{r} = \frac{qB}{m}$$

which gives a frequency f = $\omega/(2\pi)$ as

$$f = \frac{qB}{2\pi m} \tag{4.5}$$

where f is the frequency the RF generator needs to maintain in order to keep in step with the spiraling proton in the cyclotron. The spiral path keeps getting larger until the α-particle exits the D chamber on to a trajectory toward the target, T, as shown in Figure 4. 2. The trajectory is adjusted by a voltage on a deflection plate along the path. The collision of the proton with the target creates a radio nuclide.

Radioactivity

Nuclear bombardment, as in a cyclotron, can produce radioactive substances which radiate particles spontaneously. Marie Curie studied radium at the turn of the twentieth century and isolated three different types of particles emitting from the atom, arbitrarily called: α, alpha, β, beta and γ, gamma. Since then many other particles have been discovered such as neutrinos, positrons, and several quarks.

The α-particle is a helium nucleus consisting of two protons and two neutrons. Its orbiting electrons are stripped off, so it has a net positive charge of +2. Because it is large and heavy it does not penetrate matter very deeply, traveling only 4 centimeters in air, and it cannot penetrate human skin. It therefore has limited use in nuclear medicine.

The β-particle is either an electron, called β^-, or a positron, β^+, the magnitude of the charge is that of an electron. (The β-particle is assumed to be an electron unless specified otherwise.) The β-particle penetrates 0.42 cm in tissue at 1 Mev energy, slightly better than an α-particle.

The γ-ray is electromagnetic radiation, a photon. It has no mass and no electrical charge. Depending upon its energy it penetrates through most biological tissue with varying degrees of attenuation. Because of its strong penetrating power it is very useful in nuclear medicine.

Radio nuclides

Several example radio nuclides, used in nuclear medicine, radio pharmaceuticals, shown in Table 1 illustrate some important properties. The half life [4.3] indicates the time it takes for the radioactivity to decrease by half, and indicates how long the substance in the body will remain radioactive .

A longer half life will likely mean a larger dose of radiation for the patient. On the other hand, long lasting radio nuclides are easier to ship long distances. In the table, Chromium 51 has a half-life of 27.8 days, while Technetium 99m emits half of its radiation in 6 hours. Gamma radiation is the most common type among these radionuclides. The higher the energy level of the radiation the more its penetration power.

The nuclear medicine may be administered by injection, or it may be ingested, or inhaled. Iodine 131, for example may be administered either orally or intravenously, and it collects in the thyroid. Xenon may be administered through a ventilation system for lung imaging studies. Technetium 99m is a very versatile and can be used to image the brain, liver, kidney, bone marrow, heart; and check organ flow, function and location in most of these sites.

The radioactive substance may be monitored while in the body, or it may be excreted for inspection in the blood, urine or feces.

Tracking Radio Pharmaceuticals

Once a radio pharmaceutical is placed in the body, the fundamental problem is that of determining its location at any point in time. The

easiest case would be inspection of excreta or blood samples for radioactivity. This may be done with a Well counter, an important case because many nuclear medical imaging devices have evolved from it.

Well Counter

A Well Counter consists of a sample, scintillating crystal, photo cathode, photo multiplier tube (PMT) and electronic detecting circuit, as illustrated in Figure 4. 3. [4.4]

The sample is a biological substance such as blood, urine, or tissue which contains a radio pharmaceutical. The purpose of the well counter is to measure the radioactivity of the sample. In this case the emissions are gamma rays. The sample is placed in a scintillation crystal.

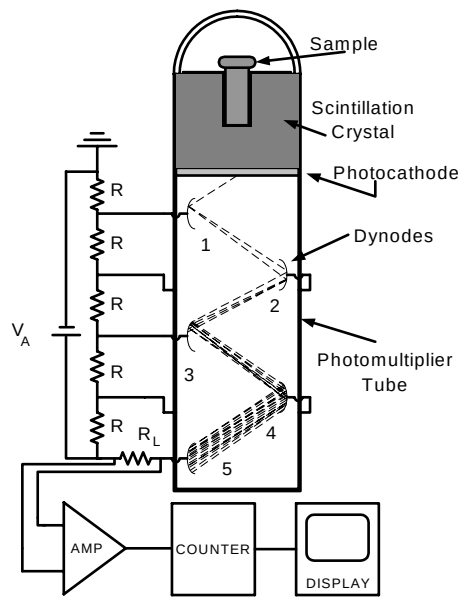

FIGURE 4.3. Well Counter

A commonly used scintillation crystal consists of sodium iodide doped with thallium (NaI(TI)). The thallium is necessary to make it scintillate, or release light at room temperatures after a gamma ray impacts it. The crystal is coated with aluminum on all sides except that next to the photo cathode. The gamma ray passes through the crystal in any direction, producing light rays which hit the photo cathode directly, or they may reflect off the aluminum foil onto the photo cathode.

The photo cathode consists of an opaque substrate coated with a cesium lead compound, which emits an electron when a photon of light strikes it. Typical sensitivities run from 3 to 150 microamps per lumen (μA/lm) of light.[4.5] The acceleration

voltage, V_A, causes equal voltage drops across successive dynodes, or plates, numbered 1, 2, 3, 4, 5 in the diagram. These voltages accelerate the electrons from the photo cathode, causing secondary electrons to emit from each dynode, such that the electron beam increases in intensity successively from dynode 1 to 5, as illustrated in the diagram. The voltage, V_A, may be adjusted by the operator, since different pharmaceuticals emit different energy levels, and the amplification required varies accordingly. Thus the current through R_L is amplified. The amplifier measuring the voltage across R_L increases the voltage of each pulse of radiation and delivers it to a counter. The output of the counter may then be displayed as counts per minute (cpm), which is the number of nuclear disintegrations per minute.

If the sample has two different pharmaceuticals of different energy levels, one may distinguish between them by inserting a threshold detector in front of the counter in Figure 4. 3. The threshold may then be set to eliminate the lower energy pulses, thus counting the higher energy pulse. This number may then be subtracted from the total count without any threshold to yield the lower energy pharmaceutical count. This process may be automated with a window detector that can select each count individually. Typically the counter should handle more than 10 thousand counts per minute (cpm).

Anger Camera

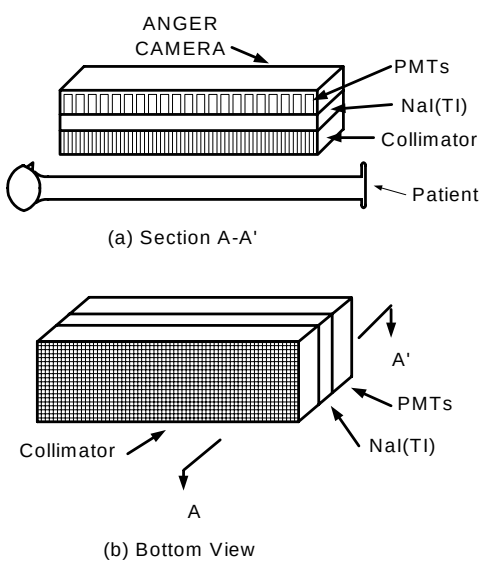

FIGURE 4.4. Anger Camera

A radio pharmaceutical in the body may be imaged on a plane with an Anger Camera, shown cut in half in Figure 4. 4. In this device, a NaI(TI) crystal, as large as 50 cm across is placed over a patient treated with a radio pharmaceutical which radiates gamma rays. The rays emit in all directions. The collimator selects those which are traveling perpendicular to the plane of the crystal. Those light rays cause the crystal to scintillate, and emit light rays into the photo multiplier tubes (PMTs), which are arranged in the plane of the crystal. Thus the location of the radiating source can be mapped in that plane by monitoring the output of the PMTs

fixed in known locations. The details of the process are illustrated in Figure 4. 5.

Of the gamma rays that emit from the patient, the direct ray passes through a lead lined hole in the collimator directly into the scintillating crystal. Those rays that are traveling at the wrong angle hit the lead or tungsten walls of the collimator hole and are absorbed. Another ray may be scattered, or deflected by atoms in the body so that it goes into a collimator hole not directly over it. This could be confused with a direct ray and cause an error in the image. However the scattered ray is of lower intensity than the direct ray, having given some of its energy to the deflecting atom. Thus the pulse height detector can distinguish between direct and scattered rays on the basis of their intensity. The pulses then are processed and produce a dot on the display, mapping the position of the PMT, resulting in a planar image of the radioactive sites in the body. The pulse height detector can also select among different pharmaceuticals radiating different energy levels, as indicated in Table 4.1. Pulses with higher energy levels create brighter scintillations. Those pulses not within the selection window would be rejected.

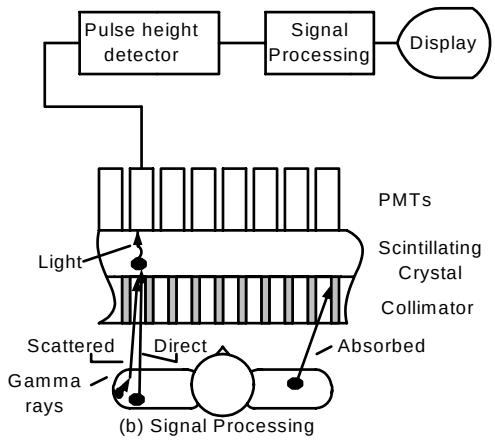

FIGURE 4.5. Planar Nuclear Imaging

It is assumed that each radiating gamma ray emerges at a different time. Counts have been achieved with an Anger camera as high as 2.22 x 10^9 counts per minute (cpm). [4.6] The time between counts is therefore 27 nanoseconds (ns). The rise times of the processing circuits need to be shorter than this to distinguish between counts. Since Tc-99m is one of the most popular radio pharmaceuticals in single photon nuclear medicine, many clinical Anger cameras are optimized for use at its radiating energy, 140 keV. This can be altered by changing the pulse height detector window.

References:

4.1. Blanchard, C. H., C. R. Burnett, R. G. Stoner, R. L. Weber. *Introduction to Modern Physics.* Englewood Cliffs, NJ: Prentice-Hall, Inc. (1958) pp 364 - 379.

4.2. Sears, F. W., M. W. Zemansky. *College Physics.* Reading, MA: Addison Wesley Publishing Co. (1957) pp. 152-156.

4.3. Weast, Robert. *Handbook of Chemistry and Physics, 52nd Edition.* Cleveland, OH: The Chemical Rubber Company (1971) p. B245.

4.4. Early, Paul J., D. B. Sodee. *Principles and Practice of Nuclear Medicine.* St. Louis, MI: C.V. Mosby Company (1985) p 232.

4.5. Aston, Richard. *Principles of Biomedical Instrumentation and Measurement.* Columbus, OH: Merrill Publishing Company (1990) p 478.

4.6. Croft, Barbara Y. "Nuclear Medicine: Instrumention" Chapter 66.1 in in Joseph D. Bronzino, Editor, *The Biomedical Engineering Handbook.* Boca Raton, FL: CRC Press (1995) pp. 1049.

Exercises

Student end-of-chapter exercises and a solutions manual for instructors are available at ABC engineering research, 33 Barney St. Wilkes-Barre, PA, U.S.A. 18702. (astonrj@yahoo.com).

CHAPTER 5
SPECT AND PET SCANNERS

For educational purposes only. See disclaimer above.

The single photon emission computer tomography (SPECT) device and positron emission tomography (PET) device are both nuclear medicine imaging instruments that create three dimensional pictures of internal anatomical sites. The SPECT scanner is a direct extension of the nuclear medicine imaging device discussed previously in Chapter 4. It can use the same Anger camera and the same nuclear pharmaceuticals. It uses the same principle, namely that the pharmaceutical is inserted into the patient and accumulates in the tissue of interest. The nuclear radiation is detected by the Anger camera and processed into a visual image, useful in diagnosis. Each nuclear event creates a singe photon, hence the name single photon emission computer tomography. The PET scanner differs in that it uses different pharmaceuticals, emitting positrons, and a different detecting camera. Fundamentally, the physics of the nuclear emission is different in the PET, as will be discussed below, in that two photons of gamma radiation result from each nuclear reaction.

The SPECT Scanner

A SPECT scanner using same detecting components as a nuclear medical imaging device that produces a two-dimensional image is illustrated in Figure 5.1.

The anger camera is fixed to a c-arm and is rotated around the patient. At each position, a scan of the radiation from the nuclear pharmaceutical is taken and stored in a computer. The same algorithm as is used in the CT scanner can then be made to generate an image of a slice through patient, as explained in the next section.

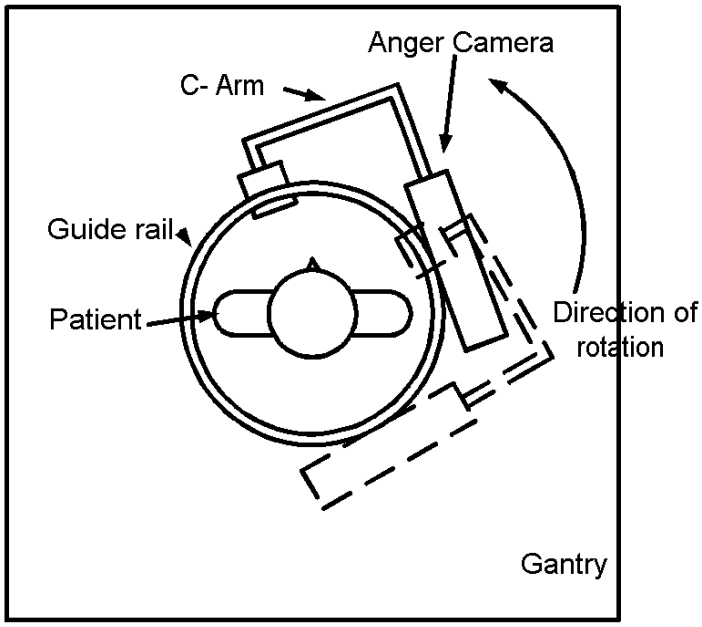

Figure 5.1. The SPECT Scanner

The SPECT Algorithm

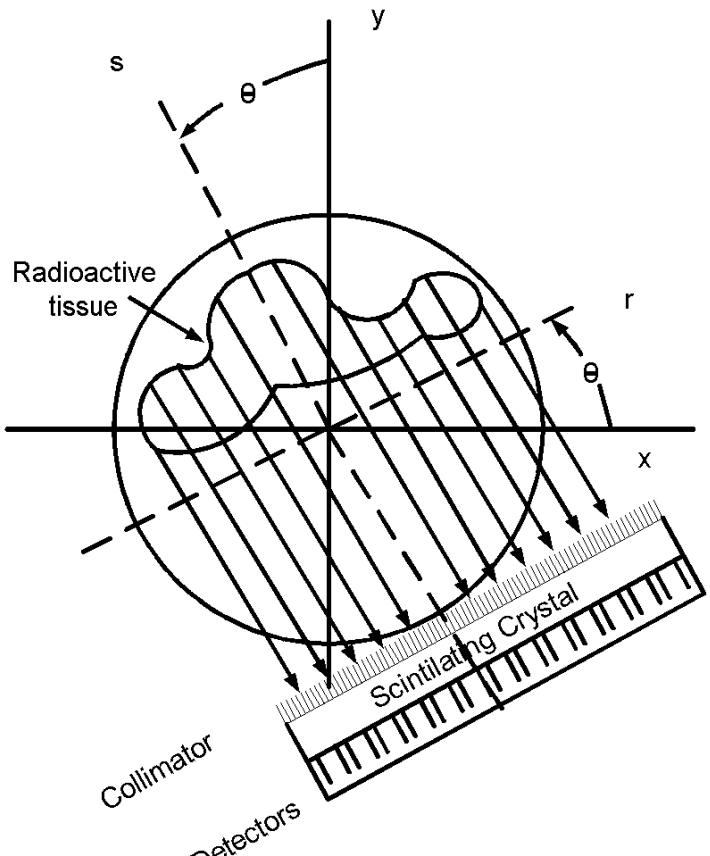

FIGURE 5.2. SPECT Scanning

The geometric relation between the radioactive tissue being imaged and the anger camera is shown in Figure 5.2. The situation is similar to that of the CT scanner (Figure 3.3 in the CT Scanner chapter). In that case, attenuation, or energy absorption, varies along the line collinear with the ray being detected. In this case it is energy generation that varies along that line. Mathematically, this is just a change in the sign; absorption negative is replaced by generative positive. Thus the form of the mathematical equations describing the process remains the same.

The Anger camera in Figure 5.2 measures rays of radiation that get through the collimator. The collimator is ideally designed to absorb any rays not collinear with the s axis. Thus the collimator insures that the measured nuclear event occurs on a cord of the circle formed by the rotating Anger camera. At a given angle θ_1, this forms a function of the axis r, $p_{\theta 1}(r)$. We may take the one-dimensional Fourier transform of this as

$$P_\theta(k) = \int_{-\infty}^{\infty} p_{\theta 1}(r) e^{-2\pi i (k \cdot r)} dr \quad (5.1)$$

Here i is the imaginary number $\sqrt{-1}$ and 2πk has the dimensions radians per meter, where k is a vector. This formula transforms the

spatial quantity $p_{\theta 1}$ into k-space. This operation can be repeated for each θ value as the Anger cammera is rotated through 0 to π radians to yield a two-dimensional function in k-space, P(k,θ). k-space is a mathematically created region containing imaginary numbers.

Thus by scanning linearly along the r-direction in Figure 5.2, rotating to another value of θ, and scanning again we have created a two-dimensional Fourier transform P(k,θ). It follows that the inverse Fourier Transform can be calculated using the two dimensional Fourier Transform in polar coordinates [5.1]

$$p(x,y) = \int_0^{\pi} \int_{-\infty}^{\infty} P(k,\theta) e^{2\pi i(xk\cos\theta + yk\sin\theta)} \; | \; k \; | \; dk \quad d\theta \tag{5.2}$$

To create the set of real numbers p(x,y), the computer first integrates on k to create a function of x, y, and θ. It then integrates on θ to create the function p(x,y) which can be mapped as a gray-scale image in rectangular coordinates. In practice we must limit the range on k to a finite number, since the computer cannot go on calculating for ever. A reasonable approximation is achieved if Equation (5.3) is written so that the integration on k goes from -k_{max} to + k_{max} as [5.2]

$$p(x,y) = \int_0^{\pi} \int_{-k_{max}}^{k_{max}} P(k,\theta) e^{2\pi i(xk\cos\theta + yk\sin\theta)} \; | \; k \; | \; dk \quad d\theta \tag{5.3}$$

where

$$k_{max} = \frac{1}{2\Delta r} \tag{5.4}$$

where Δr is the distance between radiation beams in Figure 5.2, which measures the spatial resolution of the image. The larger the number of k frequencies integrated, the better the resolution. In practice, the resolution is in the order of 1 cm for the SPECT scanner, as compared to 1 mm for an x-ray CT scanner. The image is an approximation to the ideal because a discrete, finite number of values of k and θ are chosen. Mathematicians over the past quarter century have developed many methods of improving the

approximation and the speed with which the calculation can be made by variations the basic process of taking the Fourier transform and its inverse as expressed in Equations (5.1) to (5.4) [5.3]. This process is called the filtered back-projection method. The magnitude $|k|$ in Equation (5.4) is called a ramp filter in k-space.

Advances in SPECT Scanning

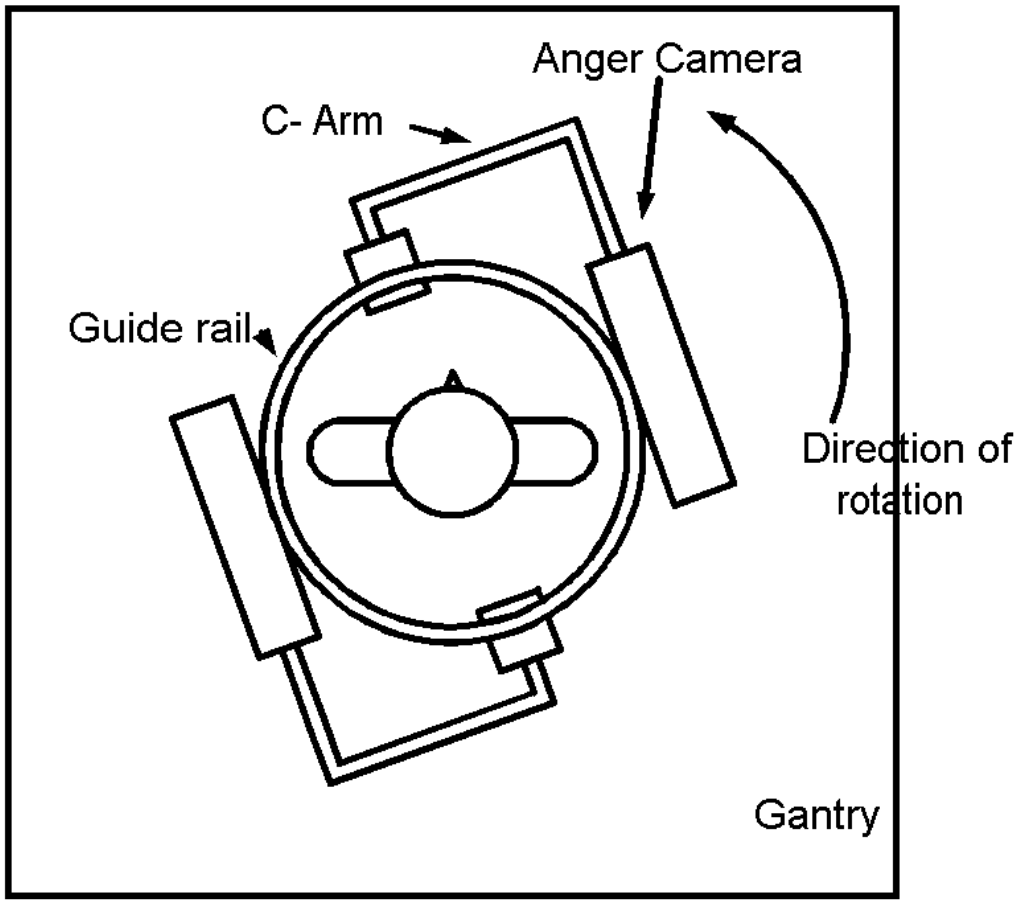

Figure 5.3. The Dual Camera SPECT Scanner

Engineering development of the SPECT scanner should have the objective of improving the scan time, count detection efficiency, resolution and accuracy.

The scan time can be shortened by adding more anger cameras, as shown in Figure 5.3, where two are shown.

The radiation from each nuclear event goes in all directions. Thus with more cameras surrounding the patient one would pick up more events and the count capability would be higher, up into the 150K count per second range. Also the patient can be scanned with less rotation of the cameras, decreasing therefore the scan time.

This logic would indicate adding more cameras around the circle, at the cost of more complexity. With a full size anger camera, four would fill the circle. However if the camera is made smaller, ten or more could fit around the circle. [5.4] Often in clinical practice, complexity and cost considerations keep the number of cameras to two. The resolution of the image is determined by the size of the collimator holes. A brain SPECT image using about 500K counts per slice has a spatial resolution reported at 8 mm, whereas a myocardial study using 150K counts per image produces a resolution of 15 mm. [5.5]

Most clinical nuclear medical instruments use thallium-activated sodium iodide (NaI(Tl)) scintillators. These have some disadvantages: they require PTMs; they are hygroscopic and thus yellow as they absorb moisture; and their density is relatively low, so their stopping power for high energy radiation is relatively low. Thus the search for better crystals is ongoing. Table 1[5.6] lists a number of candidates.

Scintillating Crystals for Gamma Radiation

Table 5.1 Properties of Scintillators [5.6]

Detector	Density g/cm^3	Effective Z	Decay time(ns)	Light Output (%)	Hygro-scopic
NaI(TI)	3.67	50.6	230	100	Y
CsI(TI)	4.51	54.1	1000	45	N
CsI(Na)	4.51	54.1	630	85	Y
BGO	7.13	74.2	350	15	N
LSO	7.4	65.5	42	75	N

As the density and effective atomic number Z of the crystals in Table 5.1 increase the stopping power increases, which means higher energy gamma rays are detected. Thus bismuth germanate (BGO) crystals, and lutetium oxyorthosilicate (LSO) crystals have higher stopping power than NaI(TI).

The decay time limits the number of counts per second that can be detected. LSO has the fastest response time, and thallium-activated cesium iodide crystal (CsI(TI)) the slowest. LSO with a 42 ns decay time could detect as much as $1/(42(10^{-9}))$ = 23.8 Million counts per second. That number for NaI(TI) is $1/(230(10^{-9}))$ = 4.35 Million counts per second.

The light output for NaI(TI) is best of the set of crystals considered, and BGO is the worst. Overall LSO has the best properties, having superior stopping power, higher count capability, relatively high light output and no hygroscopic yellowing. E.V. Garcia reports [5.7]:

> LSO can stop a 511 keV photon in about 1.16 cm, BGO in 1.05 cm, and NaI(TI) in 2.88 cm. Yet, LSO has five times the light output of BGO and about 1/10th the decay time,

making it an excellent scintillator. One drawback of the LSO crystal is that it produces its own natural radiation.

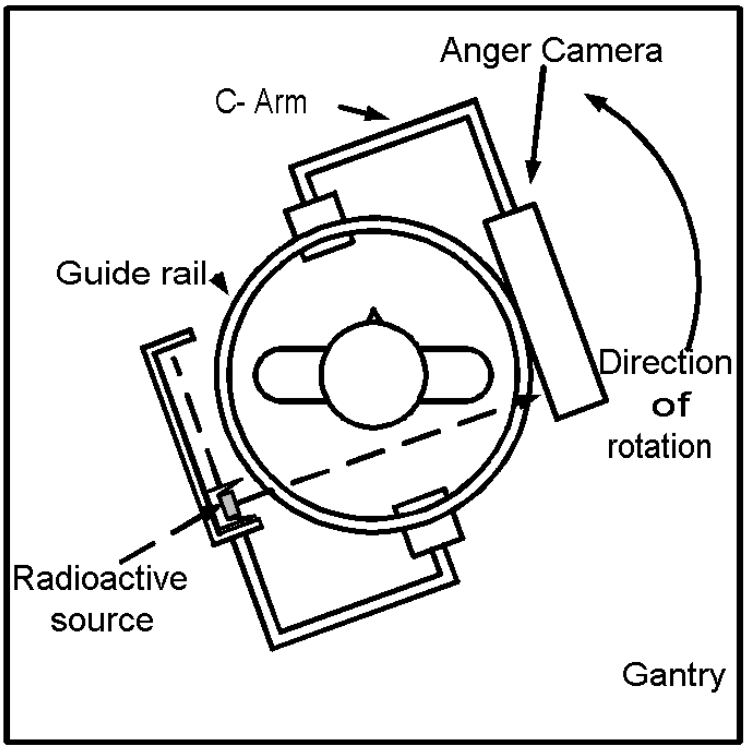

FIGURE 5.4. Attenuation Correction

Attenuation Correction

As in the case of x-ray, gamma rays are attenuated as they pass through tissue. The propagation of the gamma ray is governed by Lambert's law as discussed in the x-ray Chapter 3. Although this is nearly the same for most viscera tissue, lung and bone have widely different attenuation coefficients. Thus large errors can be introduced in to the SPECT scan. To compensate for this a CT absorption scan is taken. A x-ray tube may be used as a source. In Figure 5.4, a radioactive source is illustrated. The source is translated along its holder, and rotated around the patient so that the gamma rays emit from the source and pass through the patient's body to be collected by the Anger Camera. The CT algorithm is then used to map the attenuation coefficients. These are used to correct the SPECT scan resulting from the radio pharmaceutical in the patient.

The increased accuracy of the scan is achieved at the cost of an extra radiation dose in the patient, and more radioactive material to be contended with in the hardware.

The PET Scanner

The Positron emission tomography (PET) scanner is similar to the SPECT scanner in that it detects nuclear pharmaceuticals in the body tissue of a patient. It differs in the fact the the pharmaceuticals it uses emit positrons which in turn emit gamma rays.

Commonly used positron emitting with their half-lives and example uses are listed in Table 5.2. The half-lives listed are very short, from 2 to 110 minutes. Therefore the cyclotron used to produce ^{11}C, ^{13}N, and ^{15}O isotopes, for example has to be close by the use facility. This adds significantly to the cost. The short life times minimize the radiation dose to the patient, but make the pharmaceuticals highly perishable.

The PET scanner is useful in heart perfusion tests through the use of ^{11}C and in measurement of brain properties through glucose metabolism, oxygen utilization, and neuroreceptor studies.

The physics of positron interaction in tissue imposes differences in PET and SPECT hardware. After the positron is emitted from the isotope, it travels 1 to 4 mm before it encounters an electron with which it annihilates and produces a gamma ray as illustrated in Figure 5.5. This imposes a limit on the resolution of the PET scanner, because the position of the gamma ray is 1 to 4

TABLE 5.2. Positron emitting isotopes used in PET [5.8]

ISOTOPE	HALF LIFE (MIN)	EXAMPLE LABLED PHARMACEUTICAL	EXAMPLE USE
CARBON 11	20.39	CARBON MONOXIDE GLUCOSE	BLOOD VOLUME GLUCOSE METABOLISM
NITROGEN 13	9.96	AMMONIA	PERFUSION
OXYGEN 15	2.07	OXYGEN 15	OXYGEN UTILIZATION
FLORINE 18	109.77	HALOPERIDOL	NEURORECEPTORS

mm away from the pharmaceutical containing the isotope, which is the point desired.

The gamma ray travels in opposite directions within a tolerance of plus or minus 0.25° (0.004363 rad) . Each gamma ray is at the 511 keV level. Since the rays are assumed to be collinear in the image reconstruction mathematics, this imposes another error in measurement.

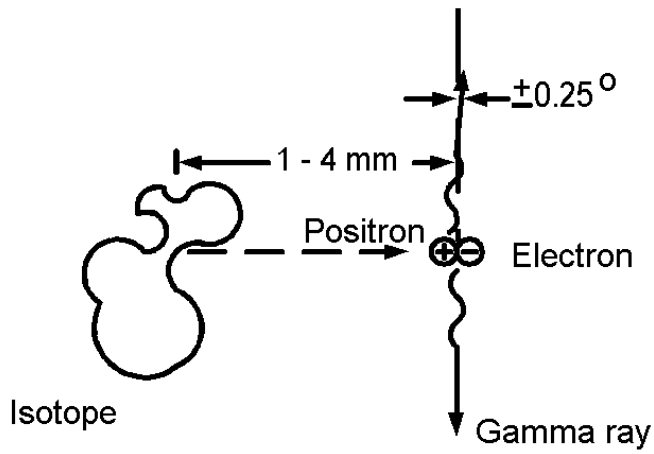

FIGURE 5.5. Positron/Electron Interaction

The gamma ray photon is electromagnetic radiation and travels at the speed of light, 3 x 10^8 m/s. This means to travel one meter the photon requires 3.33 ns. To travel 1 mm, the order of resolution desired, would require 0.0033 ns. Electronic circuitry capable of resolving the 0.0033 ns would be very difficult to design.

Electronic Collimation

The fact that the PET scanner can use electronic collimation, illustrated in Figure 5.6, and the SPECT scanner cannot, creates a major difference between the two devices.

A radio pharmaceutical is depicted as being in the right shoulder of a patient. At the top of the figure, positron-electron annihilation,

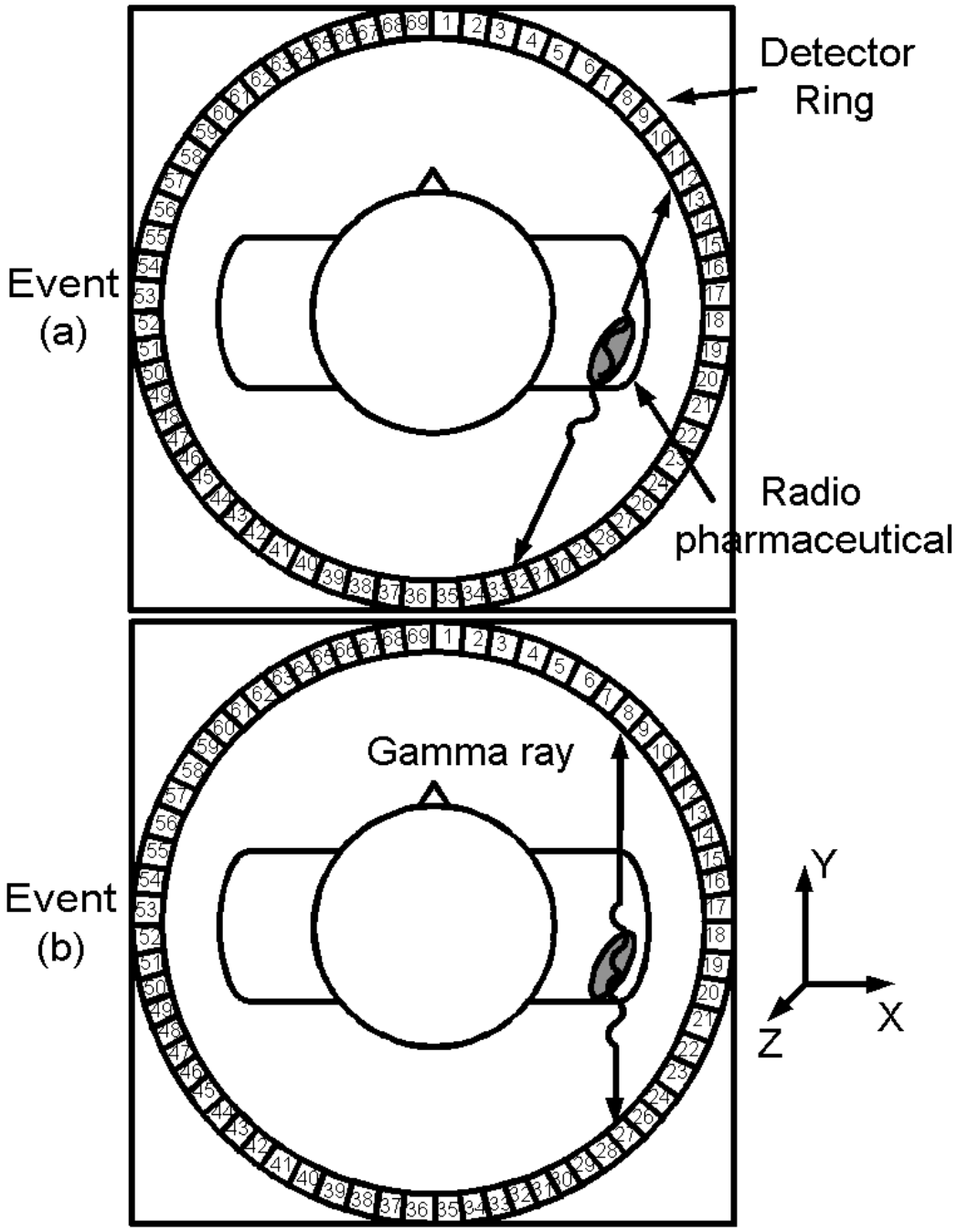

FIGURE 5.6. Electronic Collimation

event (a), creates a collinear pair of gamma ray photons that strike detectors 12 and 32 on the detector ring. Thus it is known the event occurred on a cord of the circle of the detector ring. Event (b) depicted below strikes detectors 8 and 27, telling us the event is on the cord going between those two detectors. Since millions of these isolated events occur one after another, going randomly in all directions, in a short time all detector pairs will have received a pair of gamma rays. Therefore each event, and the cord on which it occurred, can be stored a computer memory site. This is exactly the information given by the SPECT scanner as illustrated in Figure 5.2 above. This information can be used in Equations (5.1) to (5.6) to form an image of the location of the radio pharmaceutical in a cross sectional slice through the patient.

Collimation Errors

The path of the gamma rays in both the SPECT, Figure 5.2, and PET scanners, Figure 5.6 are shown to be straight lines. Some photons scatter, that is they collide with atoms and interact with electrons. This may cause their path to deviate from a straight line, and their intensity level to diminish because they loose energy in the collision. Thus they may hit the wrong detector, or enter the wrong collimation hole, and cause an error. As many as 30% of the gamma rays to enter the detectors may be scattered. To reduce the effect of scattered photons, a threshold detector is used to block low energy counts.

Errors may result if two nuclear events occur almost simultaneously, and seem to merge into one event. In this case in the PET, two gamma rays, one from each event, may hit detectors and two may be lost. Statistical methods are used classify events as random. [5.9]

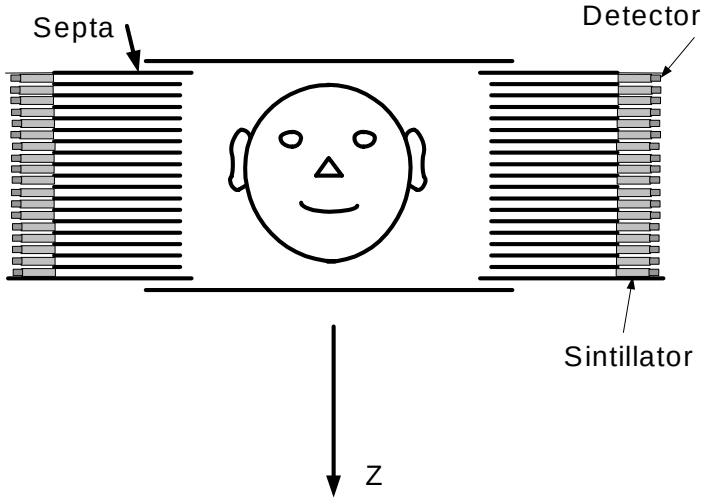

FIGURE 5.7. Axial Collimation

Axial Collimation

The collimation in Figure 5.6 is in the x-y plane, a transverse slice through the body. The nuclear event may send gamma rays in any direction. To reject gamma rays from outside the slice desired, tungsten septa may be used to absorb them as illustrated in Figure 5.7 [5.10]. In modern PET scanners, Budinger reports the septa separate 15 to 47 levels. This collimator works as described in Figure 4.5.

Detectors

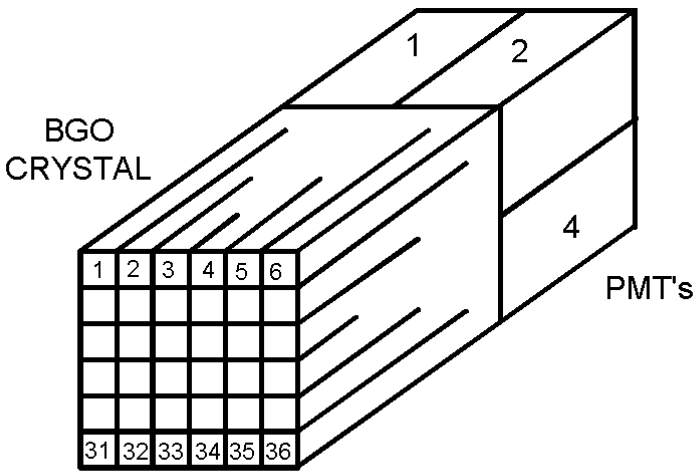

FIGURE 5.8. Detector Module

In order to improve the resolution limit imposed by the size of a photo multiplier tube (PMT), a scheme illustrated in Figure 5.8 is used.[5.11] The PMT is typically 16 mm square. A bismuth germanate (BGO) crystal is attached to an array of four such PMTs, cut into squares as illustrated in the figure. The squares may be as small 4 by 4 mm, thus improving the resolution. The depth of the cut into the crystal changes the character of the light that impinges on the PMT. The deep cuts tend to focus the light on one PMT, while the shallow cuts spread the light over several PMTs.

In the case illustrated, if the gamma ray were to fall on BGO crystal 1, it might illuminate only PTM 1. If it fell on BGO 2, it might illuminate both PMT 1 and 2. If it fell on BGO 3, it would illuminate both PMT 1 and 2, but at a lesser intensity. Continuing this coding down to BGO 36 which would illuminate only PMT 4, we have a scheme such that the 36 BGO locations can be coded into combinations of the 4 PMTs. PET scanners are used which extends this to 64 BGO crystals coded down to 4 PMTs.

Further improvement in resolution would result from the use of solid state detectors that create an electrical signal directly from the gamma ray, eliminating the need for a scintillating crystal and PMT. One such crystal is cadmium zinc telluride (CZT) [5.12]. It can be made small enough that the resolution would be limited only to the 1 to 4 mm determined by the basic physical process of conversion of a positron to gamma rays, as illustrated in Figure 5.5.

OVERVIEW, ADVANCES AND COMPARISON OF SPECT AND PET SCANNERS [5.13]

The intent of this section is to give you an overall review of nuclear imaging which emphasizes the needs of people who manage, maintain, and design such equipment. The information here is expanded greatly by the inclusion of many web sites immediately and fully available to all readers.

Nuclear imaging differs from the others such as X-ray, CT Scan, MRI and Ultrasound in that it images primarily the biological function or process of organs rather than their anatomical structure or morphology alone. This is not a totally exclusive characteristic, since the MRI can also do functional imaging, and anatomical data is sometimes gleaned from nuclear imaging. Common to all nuclear imaging, whether planar imaging, or tomography as in single photon emission computer tomography (SPECT) or positron emission tomography (PET), is the nuclide in a radiopharmaceutical which is injected into the body being imaged. The insertion is either by needle injection, oral, or by inhalation. The radiopharmaceutical is usually specific to a particular organ which absorbs it and becomes radioactive. The radiation from radioactive decay is almost always of gamma rays, which are electromagnetic waves of higher frequency and energy than either visible light or x-rays.

The planar imaging device which is designed to make a two-dimensional image of the radioactive organ or substance can, fortunately, be extended into and become an element of the tomography device, SPECT, and does not have to be redesigned. Thus if you can solve all the problems regarding SPECT scanners, you can deal with those with planar nuclear imaging as well - a nice double whammy, which justifies our emphasis on the SPECT Scanner here.

The PET scanner differs fundamentally from the SPECT in that the nuclear decay process is in two steps: first a positron (the anti-body of an electron) emerges and travels 1 to 4 millimeters until it hits an electron and annihilates, converting the masses into two gamma rays traveling in essentially opposite directions. The

travel of the positron creates a blurring effect, such that the resolution of the PET scanner cannot be better than that 1 to 4 millimeter travel distance. The resolution of nuclear imaging devices is more course than MRI or CT Scan because of this, compton scattering, and the need for collimators or equivalent gamma ray selective software. If a commercial imager has a resolution between 3 and 6 millimeters, it is probably operating within specification.

The other major design problem with nuclear imaging is in attenuation of the gamma ray as it travels from the target organ to the imaging camera. This is variable depending upon the interfering tissue. Often this attenuation is accepted as clinically tolerable error, but higher-end equipment is available which calculates the attenuation the gamma ray encountered and thereby improves the image. This correction may be built into a SPECT scanner, or one may take advantage of the fact that the fundamental process by which a CT scanner makes an image is to calculate a map of the attenuation of each element (voxel) in a slice. Thus we see on the market now combinations such as the PET/CT Scanner. This happy combination both improves the PET image by calculating the attenuation map of the slice, and by making an anatomical image of the slice as well as a biofunctional image. The MRI is not combined on a large scale yet because of the interference of its large magnetic field with the PET process. Work is also being done to combine PET and SPECT Scanners and SPECT and CT.

SPECT Scanner Advances

The basics of SPECT Scanner is available in full text on line at the web site < http://venda.uku.fi/~aoseppan/SPECTthesis.pdf > [5.14] The SPECT scanner depicted in Figure 5.3 consists of two anger cameras at right angles with each other. The cameras rotate around the patient and collect gamma rays emitted from the patient. The information thus obtained is of the same form as that in a Computer Tomography X-ray scanner. Thus the same kind of signal processing can be used to create a two dimensional (slice)

image of the organ containing the pharmaceutical. The basic data collection hardware is shown in Figure 4.5. Suppose the pharmaceutical is concentrated as shown in the patient. The gamma rays emitted may go in any direction. Those which go directly through the collimator enter a scintillating crystal, often thallium doped sodium iodide (NaI(TI)) and as a result of collisions with atoms produce a visible light photon. The light enters a photomultiplier tube where it is converted into an electron beam which is amplified. These gamma rays are attenuated by a factor depending on the patient's body tissue. Other gamma rays are scattered by collisions with atoms along the path. These rays tend to be of lower amplitude than the direct rays and may be identified by the signal processing equipment, most simply by a pulse height detector, or better with software. The collimator has septa, often of lead which absorbs gamma rays that enter it. The two major figures of merit of the SPECT scanner: *sensitivity*, the percentage of nuclear events which send rays to the detector PMTs, and the *resolution* which is a measure of the smallest particles that can be distinguished, are affected by the parts in Figure 4.5. Over the years resolution has been improved by developments in the collimator, the reduced size of PMTs, and in signal processing. Sensitivity has been improved by developments in the type of scintillating crystal and collimation process.

If the holes on the collimator are made smaller in diameter, the resolution improves, but at the cost of less sensitivity, because the gamma ray is more likely to be absorbed by the septa material when the hole is small. Smaller size PMTs also improve resolution. A position-sensitive photomultiplier tube (PSPMT) is available from Hamamatsu (see their web site < http://nedelec.home.cern.ch/nedelec/UHE/hardware/R5900-C8.pdf >) which has an array of 64 anodes in an approximately 1 square inch area package. Experiments with PET scanners using PSPMT show the possibility of a 2.8 mm resolution. (see the web site < http://www.bic.mni.mcgill.ca/users/chris/ANIPET_2000.PDF >[5.15] for a complete paper) Another approach to SPECT scanning is to employ solid state diode detectors instead of a PMT. Such a device is available from Digirad Corporation. Their website describes their Thallium doped Cesium Iodide (CsI(TI)) detector based equipment. Extensive description is offered there along with photographs. (see < http://www.digirad.com/default.asp >)

Improvements in sensitivity of nuclear imaging equipment are being sought by investigating other crystals other than the traditional thallium doped sodium iodide NaI(TI) as scintillators. Bismuth germanate (BGO) has higher stopping power but less light output per unit volume than NaI(TI), and is used in the PET scanner which emits high energy, 511 keV gamma rays. E.V. Garcia reports [5.16] that lutetium oxyorthosilicate (LSO) can stop such a photon in about 1.16 cm, BGO in 1.05 cm, and NaI(TI) in 2.88 cm. Although LSO has less light output than NaI(TI) it has five times the light output of BGO and about 1/10th the decay time, making it an excellent scintillator. One drawback of the LSO crystal is that it produces its own natural radiation, which could raise the ionization dose to the patient, and pose a hazard to the users. Gadolinium oxyorthosilicate (GSO) also has excellent stopping power and is used in PET scanners.

An excellent article on how to assess and control the quality of the SPECT image is available in full text on line at the web site: <http://tech.snmjournals.org/cgi/reprint/29/1/12.pdf >[5.17]

PET Scanner Advances

One of the major advantages of the positron emission tomography (PET) scanner is that it improves sensitivity over the SPECT scanner by utilizing electronic collimation and getting rid of the mechanical collimator. Two dimensional (2 D) PET scanners use electronic scanning in the cross-sectional plane, and use mechanical colliminators in the axial direction. Three dimensional (3D) scanners eliminate the mechanical device in all planes, and use software to colliminate in the axial direction.

In the positron emission tomography (PET) electronic collimator illustrated in Figure 5.6. The gamma rays are detected in the PET much as in the SPECT, except the PET rays are higher energy (511 KeV) so BGO crystals are often used with PMTs because of their higher stopping power, and a coincident detector is added to select those gamma rays which hit opposing detectors at the same time.

Since the SPECT and PET are primarily used to assess biological function rather than anatomical structure, it is useful to use the CT scanner in conjunction with either of these to add anatomical data. The CT scanner also measures the attenuation map so that both the PET and SPECT scans can be made more accurate. That is, the computer can take into account the attenuation the gamma ray experiences as it travels through the body tissue to the detector, using the CT data.

A PET/CT scanner has been evaluated in a full text document available on the web as the site:< http://www.petmadrid.com/documentos/Performance%20evaluation%20of%20the%20new%20whole-body%20PET_CT%20scanner_Discovery%20ST.pdf > [5.18] Written in 2004, this comprehensive article gives a description of state of the art PET scanners, describes the phantoms used for test and gives complete resolution and sensitivity data for the General Electric Corporation, Discovery PET-CT Scanner. Excellent pictures of the Philips Corporation PET/CT open Gemini scanner appear on the corporate website: < http://www.medical.philips.com/main/products/pet/assets/docs/GEMINI_Brochure_040903.pdf >.

Some experimental work is being done to combine SPECT and CT,[5.19] but to avoid excessive amounts of hardware, attenuation correction can be done by using a radioactive substance as a known source of radiation, instead of an x-ray tube, which is rotated around the patient to make a CT scan from which an attenuation map can be made to correct the SPECT scan without adding a separate CT scanner, as shown in Figure 5.4.

Troubleshooting

The quality of nuclear imaging equipment must be frequently tested in order to insure accurate data for disease diagnosis [5.20]. Phantoms containing radio active substances such as tectnetium (^{99m}Tc) as a known source of radiation are used to measure sensitivity and resolution of clinical hardware. Low sensitivity could be caused by a cloudy scintillating crystal, damaged colliminator, or weak PMTs. A failed PMT for example might produce a blank spot in the image. Good troubleshooting tips about replacing PMTs are found in the web site < http://www.atral.com/pmtwrap1.html >. Cracks in the scintillating

crystal could produce artifacts. Both resolution and sensitivity are improved if the camera is placed closer to the patient. SPECT scanners are available that have the camera follow the contour of the body for this reason.

REFERENCES

5.1. Suetens, Paul. *Fundamentals of Medical Imaging.* New York: Cambridge University Press, (2002) p 22.
5.2. *ibid.* p 78.
5.3 *ibid.*
5.4. Milster, T.D., Aarsvold, J.N., *et.al.*, "A Full-field Modular Gamma Camera." *J. Nuclear Medicine* 31:632.
5.5. Tsui, B. M. W., "SPECT (Single-Photon Emission Computer Tomography)" in Joseph D. Bronzino, Editor, *The Biomedical Engineering Handbook.* Boca Raton, FL: CRC Press (1995) pp. 1055.
5.6. Garcia, E.V., T.L. Faber, *et.al.* "Advances in Nuclear emission PET and SPECT imaging." *IEEE Engineering in Medicine and Biology*, vol 19, No 5, September/October 2000, pp 22-33.
5.7. *ibid.* p 25.
5.8. Graham, M. G. "Positron-emission Tomography" in *Encyclopedia of Medical Devices and Instrumentation, Volume 4*, Ed. by John Webster, New York: John Wiley and Sons (1988), p 2343.
5.9.Hoffman, E.J., S.C. Huang, *et.al.* "Quantitation in positron emission computed tomography: 4. Effect of accidential coincidences." *J. Computer Assisted Tomography.* 5:391, 1981.
5.10. Budinger, T.F., "Positron Emission Tomography Instrumentation" in Joseph D. Bronzino, Editor, *The Biomedical Engineering Handbook.* Boca Raton, FL: CRC Press (1995) pp. 1140-1150.
5.11.Suetens, Paul *op.cit.* p. 203.
5.12. Garcia, *op.cit.* p 22.
5.13 Aston, R. "The Fundamentals of Nuclear Imaging: SPECT and PET Scanners" *Biomedical Instrumentation and Technology.* vol 38, no 5, pp. 363-366 (Oct/Nov, 2004). This section is taken from the article cited here.

5.14. Seppänen, Aku O., “Correction of Collimator Blurring and Attenuation in Single Photon Emission Computed Tomography” University of Kuopio, M.S. Thesis, on line < http://venda.uku.fi/~aoseppan/SPECTthesis.pdf >

5.15. Nguyen, K. O. “Operational and Performance Report on ANPET, a versatile PET Scanner for Laboratory Animals”. Montreal Neurological Institute, on line < http://www.bic.mni.mcgill.ca/users/chris/ANIPET_2000.PDF >

5.16. Garcia, E.V., T.L. Faber, *et.al.* “Advances in Nuclear emission PET and SPECT imaging.” *IEEE Engineering in Medicine and Biology*, vol 19, No 5, September/October 2000, pp 22-33.

5.17. Groch, M. W., W. D. Erwin, *Journal of Nuclear Medicine Technology 2001; 29:9-15. Text on line at* < http://tech.snmjournals.org/cgi/reprint/29/1/12.pdf >

5.18. Bettinardi, V. *et al.* “Performance evaluation of the new whole body PET/CT scanner: Discovery ST,” *European Journal of Nuclear Medicine and Molecular Imaging, 10.1007/ 500259-003-1444-2 (10 February, 2004).* Full text is on line at http://www.petmadrid.com/documentos/Performance%20evaluation%20of%20the%20new%20whole-body%20PET_CT%20scanner_Discovery%20ST.pdf

5.19. Kalki K, et al. "Myocardial perfusion imaging with a combined x-ray CT and SPECT system. "J Nucl Med. 1997 Oct;38(10):1535-40.

5.20. Early, P. J., D. B. Sodee. *Principles and practice of nuclear medicine.* Saint Louis:C.V. Mosby Company (1985) Ch 13, pp 372 - 425.

Exercises

Student end-of-chapter exercises and a solutions manual for instructors are available at ABC engineering research, 33 Barney St. Wilkes-Barre, PA, U.S.A. 18702. (astonrj@yahoo.com).

CHAPTER 6
ULTRASONIC IMAGING EQUIPMENT THEORY

For educational purposes only. See the disclaimer above.

Ultrasonic Waves

Ultrasonic waves are similar to the pressure and flow waves seen in fluid flow. A pressure difference, p, across two points in matter, whether air, tissue, or metal, causes a displacement of the atoms, giving them a velocity, v. The atoms do not move very far because they are bound by elastic forces. However, the energy of one atom is transferred to the other atoms, and it propagates through matter at its own velocity.

There exists an analogy of ultrasonic waves to voltage waves: ultrasonic pressure, p is analogous to voltage, and the particle velocity, v, of ultrasonic waves is analogous to current. Furthermore, the acoustic impedance is analogous to the impedance of an electrical circuit. Therefore, your knowledge of electrical circuits will help you understanding of ultrasonics.

We must begin with a fundamental understanding of ultrasound itself. Most biological tissue of interest in ultrasound imaging, soft tissue, supports ultrasonic waves according to the following model: A solid surface is caused to vibrate and is put in contact with the tissue to launch a pressure wave in the longitudinal direction. That is, the tissue displacement is in the same direction as the wave travel.

The Wave Equation

To analyze how sound propagates in matter, we treat a fluid medium first. Most soft tissues, the primary object of medical ultrasonic imaging, would fit this model. Consider an element of

fluid with a surface area S (m^2) as shown in Figure 6.1. An external sinusoidal force, F is applied over that surface. The density of the fluid, ρ, has units of kilograms per meter cubed (Kg/m^3). M_B represents the bulk modulus of the element which is defined in the *Handbook of Chemistry and Physics* by the equation

$$M_B = \frac{p_2 - p_1}{\frac{v_1 - v_2}{v_1}} \tag{6.1}$$

where p_1, p_2 are the pressures on either side of the volume, and the denominator is the fractional change in volume due to the pressure differential. The units on Equation (6.1) are pressure in newtons per meter squared (n/m^2). M_B is measured by applying a pressure across the material under test, and measuring the fractional volume change.

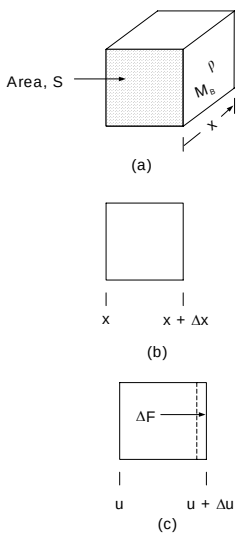

FIGURE 6.1. An element of matter in ultrasound

In equilibrium, the element in Figure 6.1(b) extends from a position of x to x + △ x. A force is applied at the surface x which displaces the left surface by a distance u and the right surface by a distance u + △u, as shown in part c of the figure. The incremental displacement ζu arises from spring action or elasticity in the element. The energy inserted into the surface at x is transferred into the element, setting it, as we see from the resulting equations, into harmonic motion. Assuming first a lossless case, the energy inserted is equal to the potential energy stored in the spring at its maximum displacement. (At other points in the oscillation the energy would be distributed between potential and kinetic energies). Thus we can form the equation

$$F\,\partial x = M_B\,S\,\partial u$$

The units on both sides here are newton-meters (n-m). Thus we can write

$$F = M_B\,S\,\frac{\partial u}{\partial x} \tag{6.2}$$

Then differentiating this with respect to x

$$\frac{\partial F}{\partial x} = M_B\,S\,\frac{\partial^2 u}{\partial x^2} \tag{6.3}$$

The displacement △u shown in Figure 6.1(c) is caused by the difference in forces on the left and right surfaces of the element,

△F. Since we have a linear system we can say the ratio of △F to △x extends down to infinitesimal dimensions so that Equation (6.3) becomes

$$\frac{\Delta F}{\Delta x} = \frac{\partial F}{\partial x} = M_B\, S \frac{\partial^2 u}{\partial x^2} \tag{6.4}$$

Now we remember Newton's law that force equals mass times acceleration and realize that the differential force △F in Figure 6.1(c) accelerates the mass ρS △x, (where ρ is the element density in kilograms per meter squared, and S is the area in meters squared) according to the equation

$$\Delta F = \rho\, S\, \Delta x \frac{\partial^2 u}{\partial t^2} \tag{6.5}$$

where u is the displacement in meters of the element from its equilibrium position and t is time. Combining Equations (6.4) and (6.5) gives

$$M_B\, S\, \Delta x \frac{\partial^2 u}{\partial x^2} = \rho\, S\, \Delta x \frac{\partial^2 u}{\partial t^2}$$

Hence

$$\frac{\partial^2 u}{\partial x^2} = \frac{\rho}{M_B} \frac{\partial^2 u}{\partial t^2} \tag{6.6}$$

We now define a quantity, c,

$$c = \sqrt{\frac{M_B}{\rho}} \tag{6.7}$$

where c has the dimensions meters per second (m/s) as shown in Exercise (6.1), and, as will shown below, is the velocity of sound in the medium. Thus Equation (6.6) becomes

$$\frac{\partial^2 u}{\partial x^2} = \frac{1}{c^2} \frac{\partial^2 u}{\partial t^2} \tag{6.8}$$

This is the wave equation for a longitudinal sound wave. It is longitudinal because the force that displaces the matter travels in the same direction as the wave, as illustrated in Figure 6.1. A Transverse wave is the kind commonly seen on the string of a guitar. The displacement of the matter is perpendicular to the direction of sound wave flow. It can be shown that the wave equation for transverse waves is identical to that for longitudinal waves.[(6.1)]

Solutions to the Wave Equation

The wave equation (6.8) describes the displacement u as a function of time and position. In a linear system, the displacement is proportional to the force, or pressure which creates it. Thus we can write u = a p, where a is a constant and p is the pressure in newtons per square meter (n/m^2). Substituting this into Equation (6.8) gives

$$\frac{\partial^2 ap}{\partial x^2} = \frac{1}{c^2}\frac{\partial^2 ap}{\partial t^2}$$

Canceling the constant a on both sides we have the wave equation for the pressure, p,

$$\frac{\partial^2 p}{\partial x^2} = \frac{1}{c^2}\frac{\partial^2 p}{\partial t^2} \tag{6.9}$$

The solution to this equation is shown in Exercise (6.2) to be

$$p = P_0 e^{j(\beta x - \omega t)} \tag{6.10}$$

where β is a phase constant with units (m^{-1}) , ω is the radian frequency, in radians per second (rad/s), both of which are measurable physical quantities, and

$$c = \frac{\omega}{\beta} \tag{6.11}$$

having units meter per second (m/s). In this solution, the sign before both the ω or β may be either plus (+) or minus (-). Equation (6.10) is a complex number, having the imaginary number designator

$$\sqrt{-1} = j$$

One solution of Equation (6.10) is the real part

$$p = P_0 \cos(\beta x - \omega t) \tag{6.12}$$

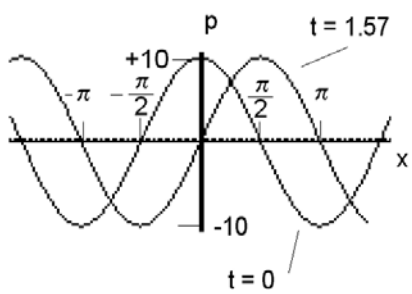

FIGURE 6.2. Sound pressure, p, as a function of x for two cases: t = 0 and 1.57 seconds.

This is the expression for a forward traveling wave, as illustrated in Figure 6.2. where an example calculation is worked out as done in Example 6.1.

EXAMPLE 6.1. Program Equation (6.12) on a graphics calculator and plot p(x) for several instants in time to illustrate that this is a forward traveling wave. Take β = 1 rad/m, ω = 1 rad/s, and P_0 = 10 N/m^2, and plot for successive times.

SOLUTION

Equation (6.12) is programed into a graphics calculator for two cases, $t = t_1$, and $t = t_2$. The resulting printout for $t_1 = 0$ and $t_2 = 1.57$. The result plotted in Figure 6.2 shows that from the time t = 0 to t = 15.7 the crest of the sound pressure wave has moved from x = 0 to x = π/2. Thus as time increases the wave travels in a positive direction. Thus it is called a forward traveling wave.

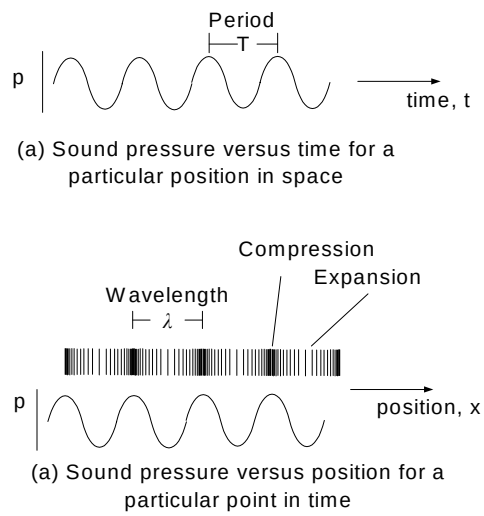

FIGURE 6.3. A logitudinal sound pressure wave

Example 6.1 shows that Equation (6.12) describes a forward traveling sound pressure wave. Notice the minus (-) sign in front of the ωt term. If one changes that to a plus (+) sign, Exercise 6.3 shows that the sound pressure wave travels in the negative x direction, and is called a backward traveling wave, with the expression

$$p = P_0 \cos(\beta x + \omega t) \tag{6.13}$$

Since the sound wave is longitudinal, it travels through the air, or other physical medium, causing alternate compressions and expansions as illustrated in Figure 6.3. Part (a) of the figure is a plot of Equation (6.13) when x is fixed at a particular value, and is simply a sinusoidal wave form. The period is the time between crests,

$$T = \frac{1}{f} \tag{6.14}$$

Where $\omega = 2\pi f$.

The wavelength, λ, is the distance between compression crests when Equation (6.13) is plotted at a particular point in time, as illustrated in part (b) of the figure. When x passes through a distance λ, the quantity βx equals 2π radians. Thus

$$\beta \lambda = 2\pi$$

or

$$\lambda = \frac{2\pi}{\beta} \tag{6.15}$$

The velocity of the sound wave is the speed at which a crest travels through space. Mathematically this is derived by noting that if we would travel along a crest in the wave the pressure would remain constant. Thus in Equation (6.12) we would have

$$\beta x - \omega t = cont$$

The crest velocity, c, is dx/dt. Differentiating both sides,

$$\beta \frac{dx}{dt} - \omega = 0$$

and

$$\frac{dx}{dt} = \frac{\omega}{\beta} = c \tag{6.16}$$

This shows that the velocity c in Equation (6.11) is indeed the speed of sound in the medium. The c is also the same as in Equation (6.7), which means that c is a physical property of the medium, dependent on its bulk modulus and density.

Also, combining Equations (6.15) and (6.16) gives another relationship for the speed of sound as

$$c = \lambda f \tag{6.17}$$

Characteristic Impedance

A sound pressure, p, propagating through a medium causes a displacement of its particles as illustrated in Figure 6.3 at a velocity, v. Materials with higher characteristic impedances cause less velocity for a given pressure. Therefore it makes sense to define characteristic impedance, Z_0, as the ratio of the pressure to the velocity, as

$$Z_0 = \frac{-p\,(when\,a\ one-directional\ traveling\,wave)}{v\,(when\,a\ one-directional\ traveling\,wave)} \tag{6.18}$$

where the negative sign arises because a positive pressure gradient causes a velocity in the negative x-direction. (In an electrical system, this impedance is defined as the ratio of voltage to current,

where voltage is analogous to sound pressure and current is analogous to particle velocity.)

To derive relationships for Z_0 we begin with an equation for the displacement, u, of the particles. Since in a linear system, the displacement is proportional to pressure, p, Equation (6.13) yields

$$u = U_0 \cos(\beta x - \omega t) \tag{6.19}$$

where U_0 is the amplitude of the displacement. The velocity, v, of the particle is du/dt, so

$$v = \omega U_0 \sin(\beta x - \omega t) \tag{6.20}$$

We can also differentiate u with respect to x, yielding

$$\frac{du}{dx} = -\beta U_0 \sin(\beta x - \omega t) \tag{6.21}$$

Then from Equation (6.2) we have

$$\frac{du}{dx} = \frac{F}{M_B S}$$

and the pressure p is equal to F/S, so this becomes

$$\frac{du}{dx} = \frac{p}{M_B} \tag{6.22}$$

This into Equation (6.21) gives

$$p = -\beta U_0 M_B \sin(\beta x - \omega t)$$

Using Equation (6.20) gives

$$\frac{p}{v} = \frac{-\beta U_0 M_B \sin(\beta x - \omega t)}{\omega U_0 \sin(\beta x - \omega t)} = \frac{-\beta M_B}{\omega}$$

This into Equation (6.18) and (6.7) yields the formula for characteristic impedance as

$$Z_0 = \frac{\beta c^2 \rho}{\omega}$$

Then from Equation (6.11) we have

$$Z_0 = c\rho \tag{6.23}$$

Table 6.1. Typical ultrasonic parameters

Material	Propagation Speed (m/s)	Density (g/mL)	Characteristic Impedance (kg/m^2-s)
Air	330	0.0012	0.000396×10^6
Blood	1530	1.06	1.622×10^6
Bone	2700-4100	1.38-1.81	$3.726\text{-}7.421 \times 10^6$
Fat	1460-1470	0.92	$1.343\text{-}1.352 \times 10^6$
Lung	650	0.40	0.260×10^6
Muscle	1540-1630	1.07	$1.648 - 1.744 \times 10^6$
Water	1520	1.000	1.520×10^6

Source: Bronzino, Joseph D, *Biomedical Engineering and Instrumentation*, p 351.

So we see the characteristic impedance of a material is equal to the product of its density and the speed of sound in the material, both measurable physical properties of the medium. The characteristic impedance of several materials appears in Table 6.1[(6.2)].

Ultrasonic Wave Reflections

Ultrasonic imaging equipment works by detecting the reflections of incident ultrasound waves, called echoes, on the tissue being investigated. Tissues are distinguished from one another by their relative reflected wave intensities. It is important to understand what property of the tissue influences reflection so that the proper uses and limitations of the equipment may be appreciated. We shall see that tissue density is important in distinguishing different organs under test. The exact analysis of ultrasound wave reflections is very complex because the boundaries in biological tissues are pretty much randomly distributed so that incident waves are largely scattered back. However in order to understand what factors affect reflection, and to make approximations of the intensity levels of reflections one may analyze the simple case of plane wave incident on a boundary between two tissues extending infinitely in either direction from the boundary as illustrated in

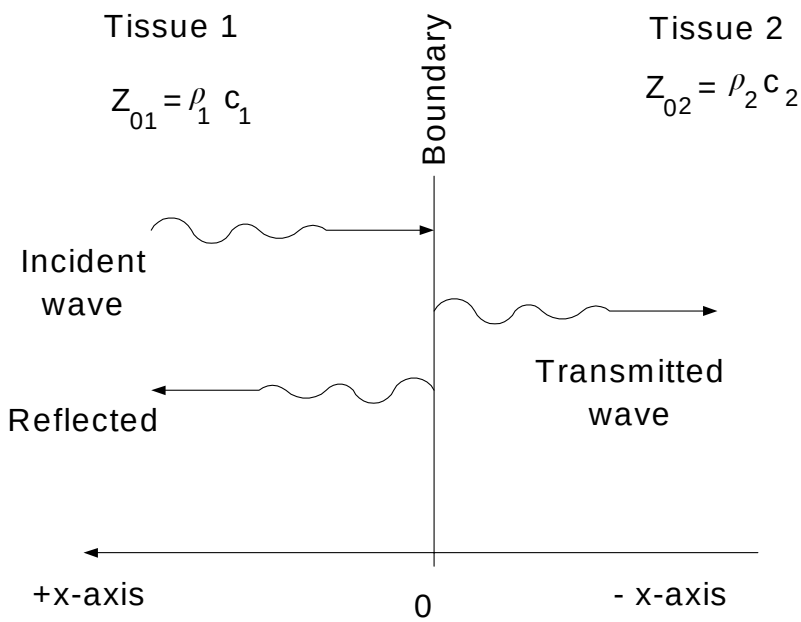

FIGURE 6.4. Ultrasound reflection from a boundary between two substances

Figure 6.4. Here the x-axis is drawn positive to the left. The expression for the sound wave traveling in the negative x-direction is given by Equation (6.13), it having a plus sign in the argument

$$p_1 = P_{01} \cos(\beta x + \omega t)$$

This is called the incident wave in the figure. As this wave hits the boundary between two tissues with different characteristic impedances, Z_{01} or Z_{02}, a portion will be reflected from it, p_2, which will travel in the positive x-direction, and will be referred to as the reflected wave

$$p_2 = R P_{01} \cos(\beta x - \omega t)$$

where R is the fraction of the incident wave which bounces off the boundary. R, the pressure reflection coefficient is defined as

$$R = \frac{pressure\ magnitude\ refected\ at\ the\ boundary\ at\ x = 0}{pressure\ magnitude\ incident\ on\ the\ boundary\ at\ x = 0} \tag{6.24}$$

Both the incident and reflected waves are traveling in tissue 1, and so the total pressure there is the sum of these, $p = p_1 + p_2$. Thus

$$p = P_{01}[\cos(\beta x + \omega t) + R\cos(\beta x - \omega t)] \quad (6.25)$$

The pressure in tissue 1 causes the molecules to move with a velocity, v, proportional to the pressure in a linear system. The reflected wave will travel in the opposite direction of the incident wave, and will therefore have a minus sign, a 180° phase shift, so that

$$v = V_{01}[\cos(\beta x + \omega t) - R\cos(\beta x - \omega t)] \quad (6.26)$$

The ratio of pressure to velocity is defined as the *wave impedance* in the tissue, z,

$$z(x) = \frac{p}{v} \quad (6.27)$$

That is, the wave impedance equals the pressure divided by the velocity of the wave composed of the sum of all incident and reflected waves, and is a function of position, x. Notice z is not the characteristic impedance as defined in Equation (6.18) because it contains waves going in multiple directions..

A means of measuring the reflection coefficient is derived by considering the wave impedance at the boundary. First set x = 0 in Equations (6.25) and (6.26) and insert these in to Equation (6.27) to yield

$$z(0) = \frac{P_{01}[\cos(\omega t) + R\cos(-\omega t)]}{V_{01}[\cos(\omega t) - R\cos(-\omega t)]}$$

Here the cosines cancel because cos(ωt) = cos(-ωt). Also the characteristic impedance in tissue 1 is given by

$$Z_{01} = \frac{P_{01}}{V_{01}}$$

since this is the ratio of the magnitudes of a wave traveling in one direction only in the tissue. Thus these two equations become

$$z(0) = Z_{01}\frac{1+R}{1-R}$$

Also at the pressure on one side of the boundary at x = 0 equals that on the other side, since both sides are infinitesimally close. Also on the right side of the boundary there are no reflected waves, so the impedance z(0) is equal to the characteristic impedance of that medium, Z_{02}. So this equation becomes

$$\frac{Z_{02}}{Z_{01}} = \frac{1+R}{1-R} \quad (6.28)$$

This is solved for the reflection coefficient as

$$R = \frac{Z_{02} - Z_{01}}{Z_{02} + Z_{01}} \tag{6.29}$$

$$R = \frac{\rho_2 c_2 - \rho_1 c_1}{\rho_2 c_2 + \rho_1 c_1} \tag{6.30}$$

These equations show that the sound pressure reflection coefficient, R, can be calculated from the physical properties of the tissue, namely its density, ρ, and the speed of sound in the material, c, or the characteristic impedance of the tissue. Appropriate data for several common biological materials are given in Table 6.1.

Power Reflection Coefficient

The quantity ultrasound pressure times velocity, pv, has the physical units

$$\frac{n}{m^2}\frac{m}{s} = \frac{n\text{–}m}{s}\frac{1}{m^2}$$

Here we see on the right side of the equation, the newton-meters per second represent energy flow,or power. Thus the right hand side represents power per meter squared, or power density, PWR. Since p and v are sinusoidal steady state waveforms, we know by analogy with electrical power theory that the power density is

$$PWR = P_{rms} V_{rms} \tag{6.31}$$

where P_{rms} and V_{rms} are the root mean square magnitudes of the sinusoidal pressure and velocity waveforms. In the case of a single traveling wave of pressure in the medium we note that

$$Z_0 = \frac{P_{rms}}{V_{rms}}$$

which inserted into the above equation gives

$$PWR = \frac{P_{rms}^2}{Z_0} \tag{6.32}$$

where PWR is the power density in watts per meter squared (W/m^2).

The power reflected from a boundary such as is illustrated in Figure 6.4 is calculated as follows: The incident pressure wave in medium carries a power given by

$$PWR_{inc} = \frac{P^2_{rms(inc)}}{Z_{01}}$$

and in the reflected wave, the pressure is reduced by a factor of the reflection coefficient, R such that

$$PWR_{ref} = \frac{(RP_{rms(inc)})^2}{Z_{01}}$$

The ratio of these two equations, where we define the ratio of reflected to incident power as Γ_R, then yields

$$\Gamma_R = \frac{PWR_{ref}}{PWR_{inc}} = R^2 \qquad (6.33a)$$

Expressed in decibels, the decibel ratio of reflected to incident power, Γ_{dBR}, is

$$\Gamma_{dBR} = 10 \log \frac{PWR_{ref}}{PWR_{inc}} = 20 \log \mathrm{R} \qquad (6.33b)$$

EXAMPLE 6.2. A power density of 1.5 Watt per meter squared is incident on a boundary of muscle and bone. The physical constants for the bone are ρ_B = 1.85 g/cm^3 and c_B = 3360 m/s, and those for muscle are ρ_M = 1.06 g/cm^3 and c_M = 1570 m/s. How much power is reflected from the boundary?

SOLUTION

From Equation (6.30) we calculate

$$R = \frac{1.85x3360 - 1.06x1570}{1.85x3360 + 1.06x1570} = 0.578$$

Then Equation (6.33) gives $\Gamma_R = 0.578^2 = 0.333$. Thus the reflected power is PWR_R = .333x1.5 = 0.5 W.

Power Transmission Coefficient

The power transmitted, PWR_{trans} through the boundary illustrated in Figure 6.4 is equal to the difference between the incident power, PWR_{inc}, and that reflected, PWR_{ref} . That is

$$PWR_{trans} = PWR_{inc} - PWR_{ref} \qquad (6.34)$$

since the power into the boundary must equal that out. The power transmission coefficient is define as

$$\Gamma_{trans} = \frac{PWR_{trans}}{PWR_{inc}} \tag{6.35}$$

From Equation (6.35) and (6.33) then we have

$$\Gamma_{trans} = 1 - \Gamma_{ref} = 1 - R^2 \tag{6.36a}$$

Expressed in decibels,

$$\Gamma_{dBtrans} = 10 \log \Gamma_{trans} = 10 \log(1 - R^2) \tag{6.36b}$$

Power Attenuation

As ultrasound propagates through matter, the magnitude of the wave attenuates due to several factors including friction between moving particles, dispersion or spreading of the beam, scattering, and spurious oscillations it may induce. To keep the mathematical model simple enough to be useful in practical calculations, we consider only friction. In a linear system this is proportional to velocity, which in the case of traveling sinusoidal waves means it is proportional to the rate of phase change. Thus the traveling wave in Equation (6.10) becomes

$$p = P_0 e^{(-\alpha_n x + j(\beta x - \omega t))}$$

or

$$p = P_0 e^{-\alpha_n x} e^{j(\beta x - \omega t)}$$

The actual wave is the real part of this, or

$$p = P_0 e^{-\alpha_n x} \cos(\beta x - \omega t) \tag{6.37}$$

where α_n is the attenuation in nepers per meter.

EXAMPLE 6.3. Program Equation (6.37) on a graphics calculator and plot p(x) to illustrate how it attenuates. Take α_n = 0.1 neper/m, β = 1 rad/m, ω = 1 rad/s, and P_0 = 10 N/m^2, and plot as a function of x for t = 1s.

SOLUTION Programing Equation (6.37) on a graphics calculator results in the graph of Figure (6.5). Notice the loss in amplitude as x increases.

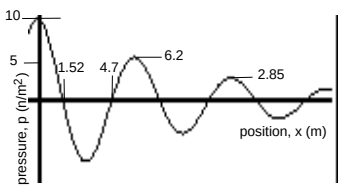

FIGURE 6.5. Attenuation as a function of position

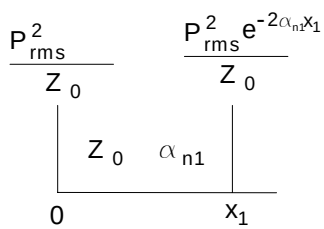

FIGURE 6.6

According to Equation (6.32) the power at x = 0 in Figure 6.6

$$\frac{P_{rms}^2}{Z_0}$$

where Z_{01} is the characteristic impedance of the medium. α_{n1} is the neper attenuation of the pressure wave. So the power at point x_1 is given by

$$\frac{P_{rms}^2}{Z_0} e^{-2a_{n1}x_1}$$

The power attenuation at x_1 relative to that at x = 0 is the ratio of these two power levels,

$$\Gamma_{att} = e^{-2a_{n1}x_1}$$

By the definition of decibel, this attenuation in decibels, Γ_{DB} is given by

$$\Gamma_{DB} = 10 \log \Gamma_{att} =$$

$$-2a_{n1}x_1 \log e = 0.8686\, a_{n1}x_1$$

We may now define the decibel unit attenuation coefficient as a_{dB} with units decibel per centimeter as,

$$a_{dB} = \frac{\Gamma_{dB}}{x_1} = 0.8686\, a_n \qquad \text{dB/cm}$$

(6.38)

where the units on α are neper per centimeter. Values for α_{dB} for several common materials are given in Table 6.2.

Table 6.2. Typical ultrasonic dB attenuation coefficient parameters

Material	α_{dB} at 1 MHz (dB/cm)	Frequency dependence
Air	1.2	f^2
Blood	0.1	$f^{1.3}$
Bone	10	$f^{1.5}$
Fat	0.6	f
Lung	40	$f^{0.6}$
Muscle	1.5 - 2.5	f
Water	0.002	f^2

Source: Bronzino, Joseph D, *Biomedical Engineering and Instrumentation, p 351.*

Notice the great variation in attenuation in different media: 10 dB/cm in bone, 1.5 to 2.5 dB/cm in muscle at 1 MHz. The frequency dependency of attenuation also varies. In fat, as you double frequency, attenuation doubles. In water since it goes as f^2, so doubling frequency quadruples the attenuation in dB/cm. As a rule of thumb approximation, the attenuation of ultrasound in the whole body is taken as directly proportional to frequency.

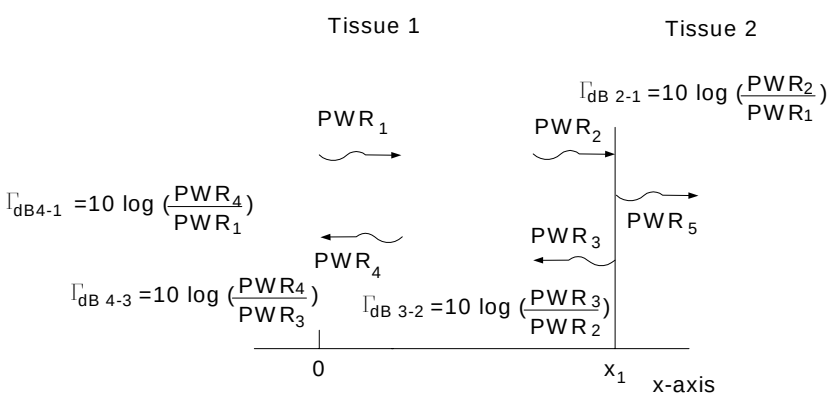

$$\Gamma_{dB\ 4-1} = \Gamma_{dB\ 2-1} + \Gamma_{dB\ 3-2} + \Gamma_{dB\ 4-3}$$

FIGURE 6.7. Power relations in a lossy medium

Power Relations at a Boundary

It is important to be able to estimate power levels as an ultrasonic wave travels through the body because the amount of reflection allows us to distinguish between tissue masses so that we can see the boundaries. To analyze the situation we follow Figure 6.7.

In this figure two lossy materials form a boundary at x_1. A pulse of power PWR_1 at x =0 is directed at the boundary, and experiences a loss in magnitude as it traverses tissue 1, and acquires the value PWR_2 incident on the boundary. A portion is reflected, depending on power reflection coefficient, producing a power level PWR_3. The pulse then travels back through tissue 1 and is attenuated to produce a power PWR_4. We need to know the

PWR_4/PWR_1 in order to estimate the signal to noise ratio of a receiver which detects PWR_4 for example. The process of calculation is as follows. Clearly,

$$\frac{PWR_4}{PWR_1} = \frac{PWR_2}{PWR_1}\frac{PWR_3}{PWR_2}\frac{PWR_4}{PWR_3}$$

since canceling like terms on the right gives the ratio on the left. To convert to decibels, we take 10 log of both sides as

$$10\ \log\left(\frac{PWR_4}{PWR_1}\right) = 10\ \log\left(\frac{PWR_2}{PWR_1}\frac{PWR_3}{PWR_2}\frac{PWR_4}{PWR_3}\right)$$

Since the log of the products is equal to the sum of the logs we write this as

$$10\ \log\left(\frac{PWR_4}{PWR_1}\right) = 10\ \log\left(\frac{PWR_2}{PWR_1}\right) + 10\ \log\left(\frac{PWR_3}{PWR_2}\right) + 10\ \log\left(\frac{PWR_4}{PWR_3}\right) \qquad (6.39)$$

In words, the total dB loss around a path is equal to the sum of the dB losses over each segment of that path. Using the symbolism of Equation (6.33b) we have

$$\Gamma_{dB4-1} = \Gamma_{dB2-1} + \Gamma_{dB3-2} + \Gamma_{dB4-3} \qquad (6.40)$$

EXAMPLE 6.4. In Figure 6.7, a pulse of power, very short compared to the transit time, heading toward the boundary is 2 W/m^2 at x = 0. It travels to the boundary at x = 2 cm, a portion is reflected, which travels back to x = 0. Tissue 1 is muscle (Z_{01} = 1.7 x 10^6 kg/m^2-s , α_{db} = 2 dB/cm) and Tissue 2 is bone (Z_{02} = 4 x 10^6 kg/m^2-s, α_{dB} = 10 dB/cm). How much power arrives back at x = 0 after making the round trip.

SOLUTION: First we calculate the dB losses experienced by the power pulse on its round trip.

Loss from x =0 to 2 cm in muscle

= -2dB/cm x 2 cm = -4 dB

To find the reflection loss at the boundary we compute the reflection coefficient, R from Equation 6.29 as

$$R = \frac{(4x10^6 kg/m^2\text{–}s) - (1.7x10^6 kg/m^2\text{–}s)}{(4x10^6 kg/m^2\text{–}s) + (1.7x10^6 kg/m^2\text{–}s)} = 0.404$$

Thus the power reflection coefficient is by Equation (6.33a) = 0.404^2 = 0.163. Then by Equation (6.33b), Γ_{dBR} = 20 log 0.163 = -15.75 dB. Then

Loss from x=2 to 0 cm in muscle is as above = -4 dB.

Thus the total round trip loss is additive as shown in Equation (6.40). So

Total round trip loss = -4 dB - 15.75 dB - 4 dB = -23.75 dB

To find the power we note that decibels are equivalent to 10 x the log of the power ratio, so in Figure 6.7 we have

$$-23.75 \text{ dB}=10 \log \frac{PWR_4}{PWR_1}$$

Taking the antilog to find the power ration gives

$$\frac{PWR_4}{PWR_1} = 10^{-2.375} = 0.00422$$

Thus the return power, PWR_4 = 0.00422 x 2 W/cm^2 = 8.44 mW/cm^2

EXAMPLE 6.5. For the situation described in Example 6.4, calculate the power launched into tissue 2 at the boundary x = 2 cm.

SOLUTION: First we calculate the dB losses experienced by the power pulse on its trip to the boundary:.

Loss from x =0 to 2 cm in muscle = 2dB/cm x 2 cm = -4 dB.

To find the reflection loss at the boundary we compute the reflection coefficient, R from Equation 6.29 as

$$R = \frac{(4x10^6 kg/m^2 - s) - (1.7x10^6 kg/m^2 - s)}{(4x10^6 kg/m^2 - s) + (1.7x10^6 kg/m^2 - s)} = 0.404$$

To find the loss the power experiences passing through the boundary, we use Equation (6.36b)

$$\Gamma_{dBtrans} = 10 \log(1 - R^2) = 10 log(1 - 0.404^2)$$
$$= -0.774\, dB$$

The total loss from x = 0 to the right side of the boundary is therefore -4 - 0.774 = -4.774 dB.

The to find the power level,

Figure 6.7 we have

$$-4.774 \text{ dB}=10 \log \frac{PWR_5}{PWR_1}$$

Taking the antilog to find the power ration gives

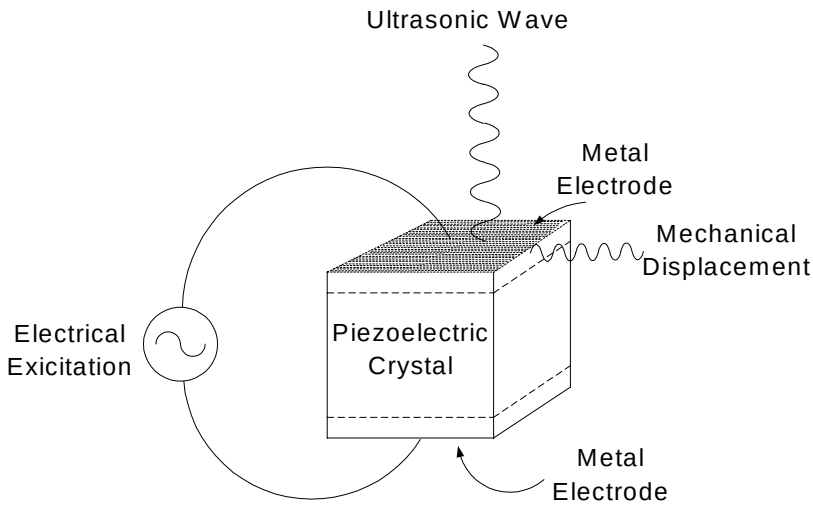

FIGURE 6.8. Ultrasound generated with sinusoidal exication

$$\frac{PWR_5}{PWR_1} = 10^{-0.477} = 0.333$$

Thus the transmitted power, PWR_5 = 0.333 x 2 W/cm^2 = 0.666 W/cm^2.

Ultrasonic Transducers

Ultrasound is usually generated with piezoelectric transducers. The typical situation is illustrated in Figure 6.8.

The transducer converts the electrical excitation applied to the two metal plates into an ultrasonic wave setup by the resultant vibrations in the crystal. A piezoelectric crystal has the property that when a voltage is placed across it, the electrical forces on the atoms are disturbed and cause the atoms to change their position. The net result, in the case shown, is the surface of the crystal in contact with the metal vibrates. If the excitation is a sinusoidal wave, the mechanical displacement will also be sinusoidal. If the metal electrode is in contact with a tissue for example, this vibration will set up a propagating, longitudinal ultrasound wave perpendicular to the electrode surface.

Piezoelectricity was first discovered in natural crystals like quartz and tourmaline, quartz (silicon dioxide) being the best of the two. Better piezoelectric materials such as barium titanate and amonium dihydrogen phosphate can be fabricated. One which produces relatively large mechanical displacements for a given voltage, lead titanate zirconate, called PZT (a registered trade name of Vernitron Ltd.) normally consists of grains in a random crystallographic orientation. Their orientation can be made systematic by application of an applied electric field, in a process called poling. In the process, the temperature of the material is raised above the Curie point, then slowly lowered so that the

piezoelectric effect remains at room temperature.[6.3] Some physical constants associated with common piezoelectric materials are given in Table 6.3[6.4].

TABLE 6.3. Properties of some piezoelectric materials

	Quartz, x-cut (see note i)	PZT-4 (see note ii)	PZT-5A (see note ii)
Tensor Subscript	11	33	33
Transmitting Constant d (m/V)	2.31×10^{-12}	289×10^{-12}	374×10^{-12}
Receiving constant g (v m/N)	5.78×10^{-2}	2.61×10^{-2}	2.48×10^{-2}
Coupling coefficient k_e	0.1	0.70	0.71
Dielectric Constant ε^T (F/m)	4×10^{-11}	1150×10^{-11}	1500×10^{-11}
Wave velocity c (m/s)	5740	4000	3780
Density, ρ kg/m	2650	7500	7750
Characteristic Imped. Z (kg/s m^2)	1.52×10^{7}	3.0×10^{7}	2.93×10^{7}
Mechanical Q	> 25000	> 500	75
Curie Temp. (deg C)	573	328	365

Table from P.N.T. Wells, p52. note(i) Data quoted from Cady, 1946) note (ii) Data extracted from Bulletin 66011/E, Vernitron Ltd., Southamptonn, UK. PZT is a registered trade name of Vernitron Ltd. Southampton, UK.

We note that PZT has a hundred fold better transmitting constant than quartz, and transmits more power per volt. It can also be molded into almost any shape and can be polarized in what ever direction desired, giving them extensive practical advantages over quartz in transducer production. The lower mechanical Q means that PZT will produce a broader bandwidth of ultrasound waves.

Impedance Matching

In order to transfer the maximum amount of energy from the piezoelectric transducer into the tissue, the crystal or ceramic must

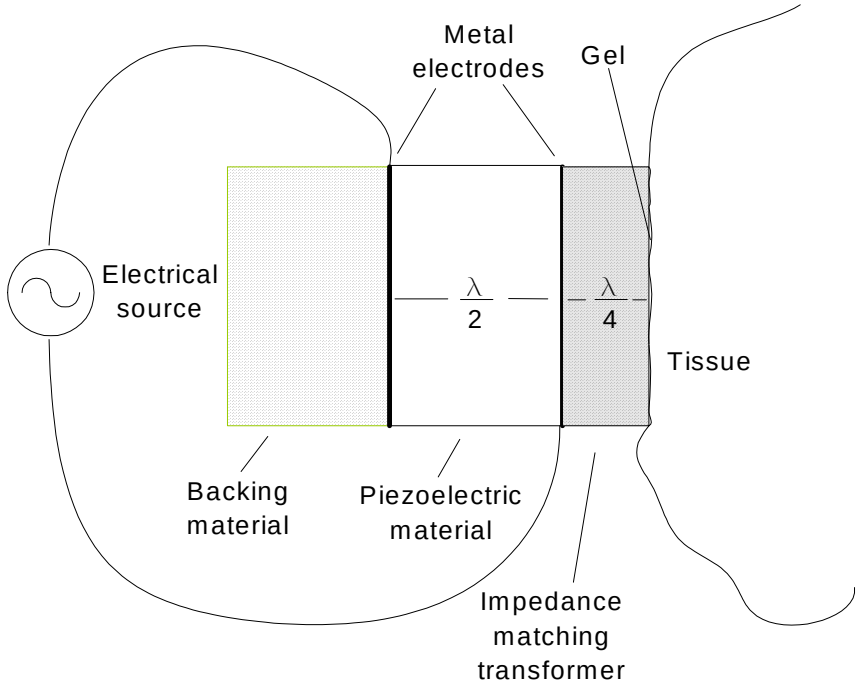

FIGURE 6.9. An ultrasound transducer

be placed in an appropriate structure that provides optimum oscillation and impedance matching. The basic structure is illustrated in Figure 6.9.

To set up an ultrasonic wave in the piezoelectric transducer, a sinusoidal voltage source may be applied between two metal electrodes. A longitudinal oscillation will be set up such that the transducer is one half wavelength ($\lambda/2$) long. (An analogy is, suppose a guitarist plucks a string and puts a finger on it. A node appears there and the string will vibrate between that point and the point where it is fixed to the guitar, one half wave length away. In general resonators vibrate at frequencies such that their length is an integer multiple of half wavelengths.) The transducer is coupled to the tissue through a quarter wave transformer ($\lambda/4$). The quarter wavelength is chosen because such a transformer will deliver maximum power to the tissue if its impedance is chosen according to the formula.

$$Z_T = \sqrt{Z_{IN} Z_{OUT}} \tag{6.41}$$

where Z_T is the characteristic impedance of the transformer, Z_{IN}, is the characteristic impedance of the material at the input to the transformer (in this case the transducer), and Z_{OUT} is the characteristic impedance of the material at the output of the transformer (the tissue). This relationship for a quarter wave transformer is derived from electrical transmission line theory, and is valid because the voltage on the line is analogous to the sound pressure, and the current on the line is analogous to the velocity of the ultrasound. An example derivation is found in Kraus.[6.5]

A gel is needed between the transducer and the tissue to fill up the air gaps that inevitably form. As you can see, from Table

6.1, the characteristic impedance of air is very much smaller than tissue, and so will introduce huge reflections that make for a bad connection. The characteristic impedance of the gel is close to that of tissue, making it suppress these reflections. The characteristic impedance of the $\lambda/4$ transformer can be adjusted by using different viscosities of oil encased in a rubber container. Thus a transducer coupled to the skull bone would use oil of a different viscosity from that coupled to muscle for maximum power transfer. In general, notice from Tables 6.1 and 6.3 that the characteristic impedance of the transducer is more that ten times that of most body tissues, making impedance matching very important for adequate power transfer. Other polymers are used to make transducers for a variety of applications. In Exercise 6.7 we show that a PZT-4 transducer can produce almost 10 mW/cm^2 with 1 volt rms excitation, meaning it can be operated from low voltage transistor circuits.

EXAMPLE 6. 6. Calculate the thickness of a PZT-4 transducer operating at 1 megahertz.

SOLUTION: From Equation 6.17 and Table 6.3 we have

$$\frac{\lambda}{4} = \frac{c}{4f} = \frac{4000\,m/s}{4x10^6\,/s} = 1\,mm$$

which is the thickness of the transducer.

In practice, ultrasound transducers may be as small as 1 mm^3.

The backing material in Figure 6.9, ideally, would reflect all of the energy from the piezoelectric device back toward the $\lambda/4$ transformer. However if it does, ringing occurs, so an empirical compromise is reached in the choice of the backing material to suppress those oscillations without absorbing too much energy.

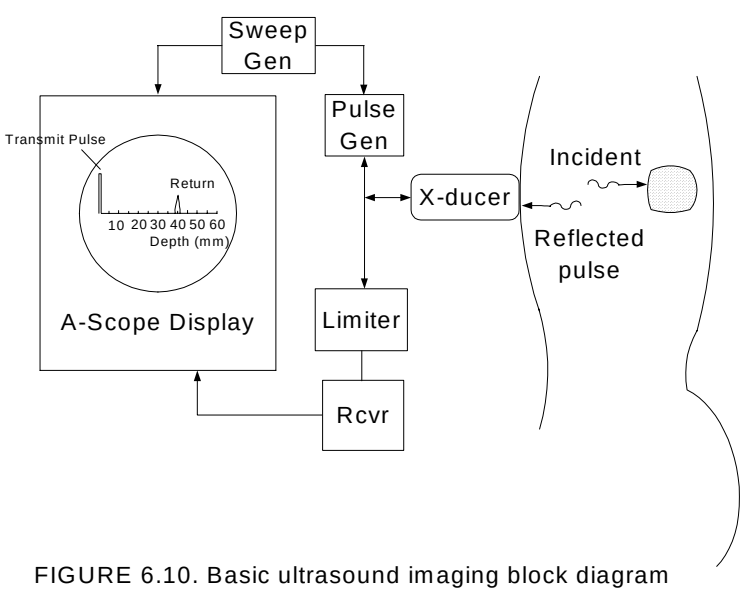

FIGURE 6.10. Basic ultrasound imaging block diagram

A-Scope Ultrasound Imaging

A simple block diagram of an ultrasound imaging system is given in Figure 6.10. Its

operation begins with the production of a pulse of voltage in the pulse generator, triggered by a timer which also begins the trace across the A-scope. The transmit pulse appears as a deflection on the left edge of the A-scope. The voltage across the transducer sets up a pulse of ultrasound power which is delivered to the subject, creating an incident power pulse that travels toward an organ to be imaged. The reflected power returns to the transducer where it is fed to the the limiter. The limiter limits the voltage level so that the high level transmitter pulse (perhaps 100 dB above the return signal) does not overload or burn out the receiver. The receiver accepts signals in the 1 to 10 MHz range in typical ultrasound equipment, and then feeds the return pulse to the A-scope. This return pulse appears as a deflection on the A-scope trace seen as the return pulse in Figure 6.10. The trace measures the time elapsed from the transmit pulse to the return, which is the time the ultrasound takes to travel from the transducer to the object imaged and back.

The trace on the A-scope is calibrated in millimeters of depth by converting the time of round trip travel to distance. The whole body speed of ultrasound is taken as 1540 m/s. Thus 1 microsecond measured on the trace is equivalent to 1.540 mm round trip, or half this in depth to the object imaged. (ie. 1 microsecond is equivalent to 0.770 mm depth). This type of display may be used to find the depth of an object in the body. It is similar to a range finder in a sonar on ships that determine the distance to obstacles under water, or the depth to the ocean floor. Controls on the receiver may be adjusted so that the receiver gain increases in proportion the distance along the trace. This compensates for attenuation the power pulse experiences in travel and keeps the size of the reflection pips about the same for similar boundaries. The A-scope gives information about the depth of objects under the skin. To obtain a planar view of the object, showing both the depth and breath of the object, a B-scope is used.

B-Scope Imaging

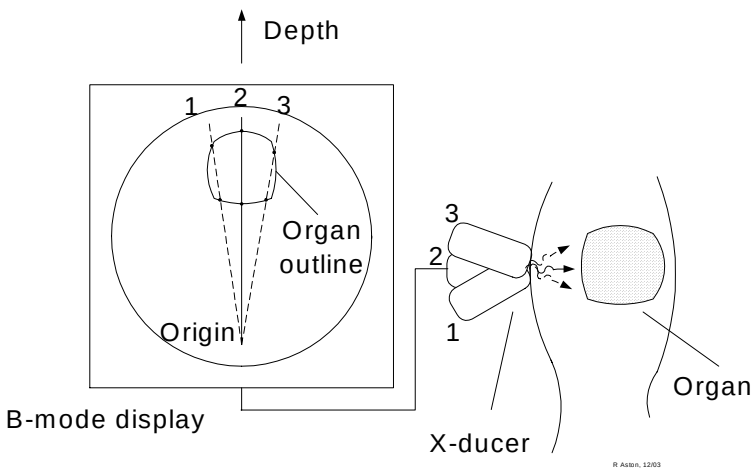

FIGURE 6.11. A B-mode image

A planar view of an organ can be obtained by causing the transducer to sweep through an angle, as illustrated in Figure 6.11. In position 1, the ultrasound pulse travels to the object and sends a reflection at the two boundary points where it enters and leaves. These are recorded on a screen as an increase in intensity of the beam which makes a brighter mark. The beam then rotates toward position 2, giving reflections which trace out more of the boundary on the screen, proceeding to postion 3, etc. This type of scope is widely used in producing ultrasound images of fetuses.

The transducer may be rotated mechanically to achieve this display, and such transducers are in use in the clinic. To achieve faster display sweeps, phased array transducers, explained below, are used. These rotate the sweep electronically, so that one is not slowed down by the inertia of a mechanical system, making it possible achieve clear images of moving objects such as the heart.

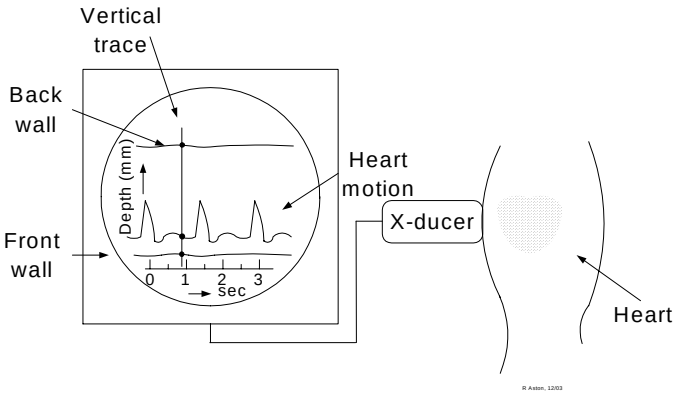

FIGURE 6.12. An M-mode image

M-mode Display

Motion of an organ such as the heart can be imaged using the M-mode on an ultrasound imager, as shown in Figure 6.12.
The vertical trace is proportional to the depth of the object imaged, as in the A-scope, and the height of the echo is displayed by a brightening of trace. The trace then moves at a speed much slower than the transit time of the ultrasound pulse, so that it records changes in depth as a function of time. In the case shown, heart

valve motion appears as a deflection, showing its variation in the depth as the heart beats.

Phased Array

The phased array approach , illustrated in Figure 6.13, allows one to sweep a B-mode image at electronic speeds, and to focus the ultrasound deep under the skin. The piezoelectric transducer elements, which can be as small as one millimeter across, are aligned in a row as illustrated, with a distance, D, separating them. Consider the ultrasound at the point P at the end of a line OP, which is very much longer than the length of the transducer. (Figure 6.13 is not in scale.). The difference in the OP path length, l, between adjacent transducer elements is related to D and the angle, ϑ, between the transducer array and OP. The expanded view at the two elements shows a right triangle, for which the following relationship holds,

$$\cos\vartheta = \frac{l}{D} \tag{6.42}$$

Of the two paths shown, the lower one in this case is longer, but its pulse leaves its element T_D seconds sooner than the upper one. Thus the two pulses arrive at point P at the same time when

$$l = c\,T_D \tag{6.43}$$

where c is the speed of sound in the medium. Combining Equations (6.43) and (6.42) yields,

$$\cos\vartheta = \frac{c\,T_D}{D} \tag{6.44}$$

This has the effect of causing constructive interference, or pulse addition at the point P. Similarly, the pulses from the other transducer elements will arrive in phase at point P and add. Now if the time delay is changed to a new value, a new angle ϑ will be made. This process can be carried on at electronic speeds, making it possible to sweep a B-mode display more rapidly than is possible by physically rotating the transducer.

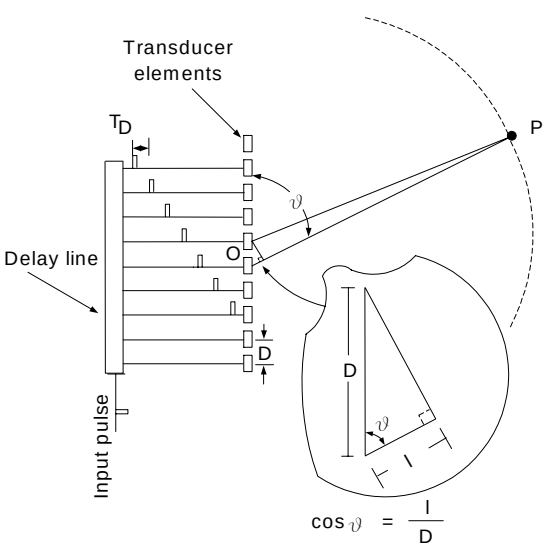

FIGURE 6.13. Ultrasound Phased Array

References

6.1. Wells, P.N.T. *Biomedical Ultrasonics.* New York: Academic Press (1977) p 1.16.
6.2. Bronzino, Joseph D. *Biomedical Engineering and Instrumentation: Basic Concepts and Applications.* Boston, MA: PWS Engineering (1986) p 351.
6.3. Hennig, Ewald D. "Piezoelectric Sensors" in *Encyclopedia of Medical Devices and Instrumentation*, ed. by John Webster, New York: John Wiley & Sons, vol 4. (1988) pp2310-2319.
6.4. Wells, P.N.T. *op.cit. (p 52).*
6.5. Kraus, John D and K. R. Carver. *Electromagnetics, Second Edition.* New York: McGraw Hill Book Co. (1973) p 509.

Exercises

Student end-of-chapter exercises and a solutions manual for instructors are available at ABC engineering research, 33 Barney St. Wilkes-Barre, PA, U.S.A. 18702. (astonrj@yahoo.com).

.

APPENDIX A

Magnetic Field of a Current Loop [1A]

According to the Biot-Savart Law, the magnetic field density caused by a current, I, in an element of wire, dl, in a circular current loop, shown in Figure A1 is

$$dB=\frac{\mu I dl \sin\theta}{4\pi r^2} \qquad \text{(A1)}$$

where dB is the magnetic field element, θ is the angle between the element of wire and the radian, r, and μ is the permeability of the medium. The direction of dB is shown perpendicular to the radian. Because of the symmetry of the loop, the magnetic field exists only as the component B_Z along the axis of the loop. B_Z is given by

$$dB_Z=dB\cos\xi=dB\frac{R}{r} \qquad \text{(A2)}$$

The angle θ between the direction of dl and the radian r is 90° , making the sin θ equal to 1 in Equation (A1). The arc length dl is given by,

$$dl = R\, d\phi$$

and because it in a right triangle, r is,

$$r = \sqrt{R^2 + z^2} \qquad \text{(A3)}$$

Substituting these into Equation (A2), yields

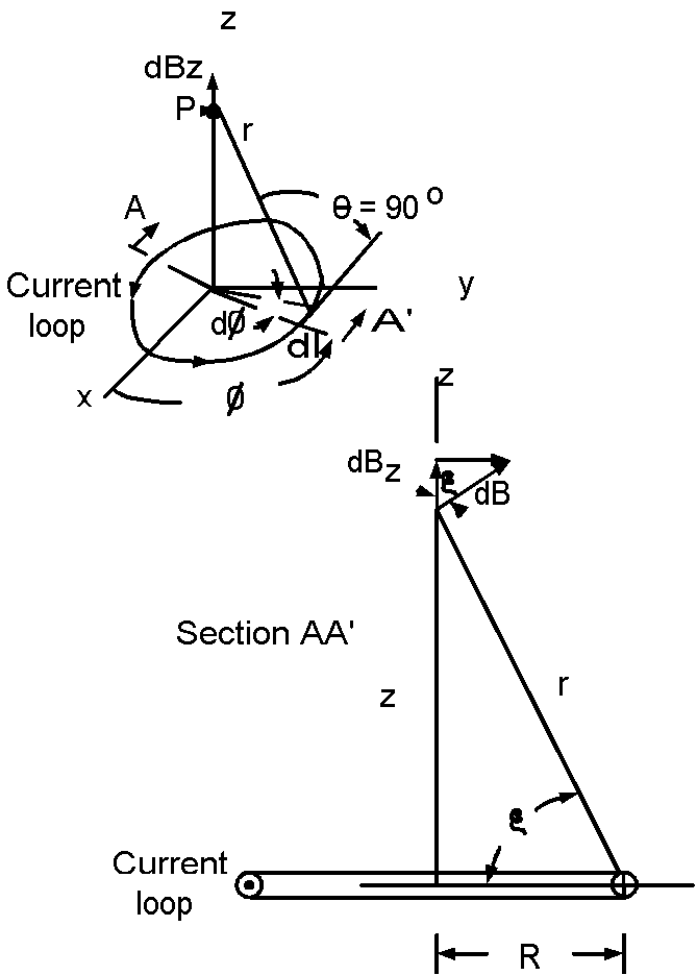

Figure A1

$$dB_Z = \frac{\mu I R^2}{4\pi r^3} d\phi$$

Then substituting Equation (A3) yields,

$$dB_Z = \frac{\mu I R^2}{4\pi (R^2 + z^2)^{\frac{3}{2}}} d\phi$$

To get the total field along the z-axis, we integrate with respect to ϕ

$$B = \int dB_Z = \int_0^{2\pi} \frac{\mu I R^2}{4\pi (R^2 + z^2)^{\frac{3}{2}}} d\phi$$

Integrating we have

$$B = \frac{\mu I R^2}{4\pi (R^2 + z^2)^{\frac{3}{2}}} [\phi]_0^{2\pi} = \frac{\mu I R^2}{2(R^2 + z^2)^{\frac{3}{2}}} \qquad \text{(A4)}$$

Which is the magnetic field along the z-axis of the loop. Off that axis the field is more complicated.

Magnetic Field in a Solenoid [2A]

The magnetic field along the axis of a solenoid can be derived from Equation (A4). If the coil has a large number of closely packed turns, N, each coil can be considered a single element containing a current

$$\frac{NIdz}{L} \quad \text{amps} \qquad \text{(A5)}$$

as illustrated in Figure 1.9.

Equation (A4) then expresses an element of the magnetic field dB made by the current in Statement (A5), which replaces the “I” of Equation (A4). Thus we have

$$dB = \frac{\mu N I R^2}{2L(R^2 + z^2)^{\frac{3}{2}}} dz$$

The total field along the axis of the solenoid is then found by integrating the contributions of all elemental loops from -L/2 to L/2 along the length of the coil, L. That is,

$$B = \int_{-\frac{L}{2}}^{\frac{L}{2}} dB$$

Substituting Equation (1.5) gives

$$B = \frac{\mu N I R^2}{2L} \int_{-L/2}^{L/2} \frac{dz}{(R^2+z^2)^{\frac{3}{2}}} \qquad \text{(A6)}$$

From standard integral tables we can find the relationship

$$\int \frac{dz}{(R^2+z^2)^{\frac{3}{2}}} = \frac{z}{R^2\sqrt{R^2+z^2}}$$

Evaluating this between the limits -L/2 to +L/2 yields,

$$\frac{\frac{L}{2}}{R^2\sqrt{R^2+\frac{L^2}{4}}} - \frac{-\frac{L}{2}}{R^2\sqrt{R^2+\frac{L^2}{4}}} = \frac{2L}{R^2\sqrt{4R^2+L^2}}$$

This result substituted into Equation (A6) gives

$$B = \frac{\mu N I}{\sqrt{4R^2+L^2}} \qquad \text{(A7)}$$

where R is the radius of the coil, L the length, N the number of turns, I the current and μ is the permeability. Equation (A7) calculates the magnetic field flux at the center of the solenoid.

Reference Appendix A

A1. Kraus, John D., Keith R. Carver. *Electromagnetics 2nd Edition.* New York: McGraw Hill, Inc. (1973) pp 147-148.

A2. *ibid.* pp 155-157.

APPENDIX B FOURIER TRANSFORM

The fourier transform arises from the Fourier Theorem. This theorem states that *a periodic function can be expressed as a series of harmonically related sinusoidal signals.* Mathematically this is stated as:

$$f(t) = a_0 + \sum_{n=1}^{N} a_n \cos n\omega_0 t + \sum_{n=1}^{N} b_n \sin n\omega_0 t \tag{B1}$$

Here n is an integer, N is the upper limit on the integers n, ω_0 is the fundamental radian frequency, t is time and a_n and b_n are unknown constants given by the following relationships.

$$a_0 = \frac{1}{T}\int_0^T f(t)\,dt$$

$$a_n = \frac{2}{T}\int_0^T f(t)\cos(n\omega_0 t)\,dt$$

$$b_n = \frac{2}{T}\int_0^T f(t)\sin(n\omega_0 t)\,dt$$

where T is the period of the periodic signal. Thus at any particular time, t, f is a function of

$$\omega = n\omega_0$$

which are harmonically related radian frequencies.

If the period of T is taken to be infinite (∞) one can show the Fourier Theorem implies that [B1]

$$f(t) = \frac{1}{2\pi}\int_{-\infty}^{\infty} F(\omega)e^{j\omega t}\,d\omega \tag{B2}$$

$$F(\omega) = \int_{-\infty}^{\infty} f(t)e^{-j\omega t}\,dt \tag{B3}$$

Here $F(\omega)$ is the fourier transform of f(t). Equation (B2) is a function of time alone, since the frequency is a running variable. We therefore say the function is in the time domain. Equation (B3)

expresses that function in the frequency domain, since it is a function of frequency alone. Equations (B2) and (B3) form a fourier transform pair, (B3) being the fourier transform, and (B2) being the inverse fourier transform.

The Fourier Transform of a Pulse

The pulse in Figure B1 is described mathematically as:

$$v(t) = A \quad when \quad |t| < \frac{T_D}{2}$$

$$= 0 \quad when \quad |t| > \frac{T_D}{2}$$

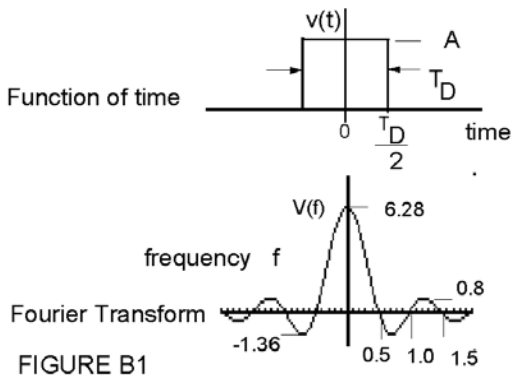

FIGURE B1

This inserted in Equation (B3) gives,

$$V(\omega) = A \int_{\frac{-T_D}{2}}^{\frac{T_D}{2}} e^{-j\omega t} dt \qquad \text{(B4)}$$

To solve this we need to recall two standard mathematical identities:

$$\int e^{ax} dx = \frac{e^{ax}}{a} \qquad \text{(B5)}$$

and

$$\frac{e^{jx} - e^{-jx}}{2j} = \sin x \qquad \text{(B6)}$$

Using Equation (B5) in (B4) we have

$V(\omega) = A\frac{e^{-j\omega t}}{-j\omega}$ evaluated between limits $-T_D/2$ and $T_D/2$ gives,

$$V(\omega) = A\left(\frac{e^{-j\omega\frac{T_D}{2}}}{-j\omega} - \frac{e^{-j\omega\frac{T_D}{2}}}{-j\omega}\right)$$

Equation (1.7) into this gives

$$V(\omega) = 2A\frac{\sin\omega\frac{T_D}{2}}{\omega}$$

And in terms of frequency f = $\omega/2\pi$, we this becomes,

$$V(f) = \frac{A}{\pi}\frac{\sin(\pi \quad f \quad T_D)}{f} \qquad \text{(B7)}$$

EXAMPLE B1
A voltage pulse of amplitude, A, 3.14 volts, and duration, T_D = 2 sec. Use a graphics calculator to plot the fourier transform of this pulse.
SOLUTION
On the TI-85 calculator set the Equation (B7) in the GRAPH mode, keystroke

y1 = (A*sin(π*x*TD))/(π*x)

where x is the running variable for frequency on the calculator.
Store the values:
3.14 STO A
2 STO TD
A resulting plot of the fourier transform V(f) is shown at the bottom of Figure B1.

The Inverse Fourier Transform of a Pulse

It is important to know what function of time will produce a band of frequencies of constant amplitude in the frequency domain in the operation of an MRI. This question is answered if we know what function in the time domain corresponds to the following in the frequency domain:

$$\begin{aligned} V(f) &= 0 \quad when \quad |f| > f_0 \\ &= B \quad when \quad |f| < f_0 \end{aligned} \qquad \text{(B8)}$$

where f is the frequency in Hertz (Hz) and B is a real constant. To find the answer we use the inverse Fourier transform, Equation (B2), and integrating as,

$$v(t) = \frac{1}{2\pi}\int_{-\omega_0}^{\omega_0} B e^{j\omega t} d\omega = \frac{B}{\pi t}\left|\frac{e^{j\omega t}}{2j}\right|_{-\omega_0}^{\omega_0}$$

Here ω_0 is finite, so v(t) only approximates the inverse Fourier transform, since in Equation (B2) the limits are infinite. The larger ω_0 the better the approximation will be. Evaluating the limits gives,

$$v(t) = \frac{B}{\pi t}\left|\frac{e^{j\omega_0 t} - e^{-j\omega_0 t}}{2j}\right| = \frac{B}{\pi}\frac{\sin(\omega_0 t)}{t} \qquad \text{(B9)}$$

This written in terms of frequency $f_0 = \omega_0/2\pi$ is

$$v(t) = \frac{B}{\pi}\frac{\sin(2\pi f_0 t)}{t} \qquad \text{(B10)}$$

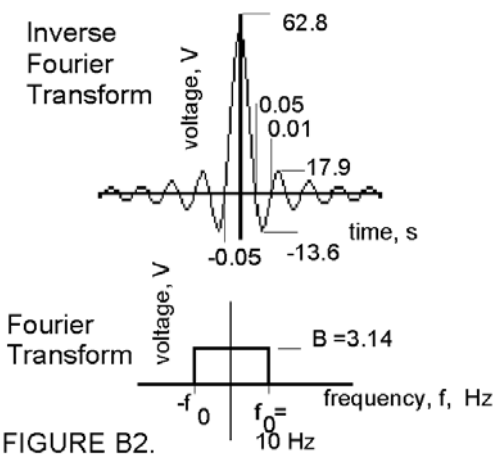

FIGURE B2.

EXAMPLE B2. A radio frequency (RF) voltage is modulated by a pulse of shape given in Equation (B10) of 10 Hz = f_0 and B = π. Find the corresponding fourier transform, V(f) in the frequency domain, and plot the two functions.

SOLUTION

To plot v(t) of Equation (B10) on a graphics calculator such as the TI-85, 86 or 89 operated in the y = editor, keystroke

Y2=(B*sin(2π*f0*x))/(π*x) (B11)

where x is a running variable representing time in the calculator. In this case store the following quantities:

π STO B

10 STO f0

A plot of Equation (B11) is given at the top of Figure B2.

Three Dimensional Fourier Transform[B2]

The Fourier transform extends into three dimensions as follows:

$$S(\vec{k}) = \int_{-\infty}^{\infty}\int_{-\infty}^{\infty}\int_{-\infty}^{\infty} s(\vec{r})\, e^{-2\pi i \vec{k}\cdot\vec{r}}\, d\vec{r} \qquad \text{(B12)}$$

The inverse Fourier transform is:

$$s(\vec{r}) = \int_{-\infty}^{\infty}\int_{-\infty}^{\infty}\int_{-\infty}^{\infty} S(\vec{k})\, e^{+2\pi i \vec{k}\cdot\vec{r}}\, d\vec{k} \tag{B13}$$

where i is the imaginary number operator and the vector multiplication is a dot product.

$$\vec{r} = \hat{x}\cdot x + \hat{y}\cdot y + \hat{z}\cdot z \tag{B14}$$

is a spatial vector, and

$$\vec{k} = \hat{x}\cdot k_x + \hat{y}\cdot k_y + \hat{z}\cdot k_z \tag{B15}$$

is a frequency vector, as expressed in rectangular coordinates. In one case r may have the dimension meters (m), and k the dimension m^{-1}. In another case r may represent time (t) and k have the dimension t^{-1}.

REFERENCES

B1. Papoulis, Athanasios. *The Fourier Integral and its Applications.* New York: McGraw-Hill Book Company, Inc. (1962) p7.

B2. Bracewell, R.N. *The Fourier Integral and Applications, First Edition.* New York: McGraw Hill (1978) p2

APPENDIX C 90° PHASE SHIFT CIRCUIT

Analyzing the circuit in Figure C1,

$$\frac{V_{OUT}}{V_{IN}} = A_V \frac{\frac{1}{j2\pi fC}}{R+\frac{1}{j2\pi fC}} = A_V \frac{1}{1+j2\pi fRC}$$

Under the condition

$$2\pi fRC \gg 1 \qquad \text{(C1)}$$

this becomes

$$\frac{V_{OUT}}{V_{IN}} = A_V \frac{1}{2\pi fRC} \angle -90^o$$

Then if

$$A_V = -2\pi fRC \qquad \text{(C2)}$$

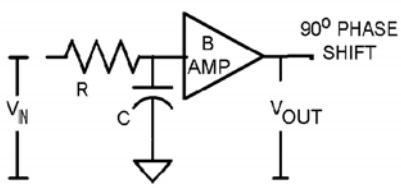

FIGURE C1

$$V_{OUT} = V_{IN} \angle 90^o \qquad \text{(C3)}$$

Thus the output leads the input voltage by 90°.

APPENDIX D

MRI FAST SCAN TECHNIQUE

One method of decreasing the scan time over the Spin Echo sequence is to eliminate the 180 degree pulse and replace the 90 degree excitation pulse with one that causes the tilt angle of the magnetization, θ, to be less to be less than 90 degrees. That this process works is indicated mathematically as follows: The Bloch equation, which gives the relationship between tissue magnetization, M and the applied magnetic field strength, B is modified for the existence of an inital magnetization caused when TR is less than the time constant of the FID as follows:

$$\frac{d\vec{M}}{dt} = \gamma \vec{M} \times \vec{B} - \frac{M_x \widehat{a_x} + M_y \widehat{a_y}}{T_2} - \frac{(M_z - M_z^0)\widehat{a_z}}{T_1} \quad \text{(D1)}$$

Where M^0_z is the magnetization in the z-direction at t = 0. The solution to this equation is [(D1)]

$$M_z(t) = M_0(1 - e^{-t/T_1}) + M_z^0 e^{-t/T_1}$$

(D2a)

$$M_x(t) = M_{xy}^0 \cos\ \omega_0 t\ e^{-t/T_2}$$

(D2b)

$$M_y(t) = -M_{xy}^0 \sin\ \omega t\ e^{-t/T_2} \quad \text{(D2c)}$$

The z-component is called the longitudinal component of the magnitization because it follows the MRI core axis, and the x and y-components are the transverse component. For the fast scan, the z-component, M_z (t), is measured by the RF loop and the x and y components are ignored. Following the derivation given by Scott Reeder[(D2)], M_n^b represents the magnetization just before the nth RF excitation pulse , and M_n^a represents the magnitization just after. After the first pulse the longitudinal magnetization is:

$$M_1^a = M_1^b \cos\ \theta = M_0 \cos\ \theta \quad \text{(D3)}$$

Where θ is the tip angle of the induced magnitization, as set by the size of the magnitization pulse given by Equation (1.4), and M_0 is the initial logitudinal magnitization. The next pulse occurs after a time TR and Equation (D2a) becomes:

$$M_2^b = M_0\left(1 - e^{-\frac{TR}{T1}}\right) + M_1^a e^{-\frac{TR}{T1}}$$

(D4)

Substituting the above equation yields,

$$M_2^b = M_0\left(1 - e^{-\frac{TR}{T1}}\right) + M_1^b \cos\ \theta e^{-\frac{TR}{T1}}$$

(D5)

Likewise after the third pulse,

$$M_3^b = M_0\left(1 - e^{-\frac{TR}{T1}}\right) + M_2^b \cos\ \theta e^{-\frac{TR}{T1}}$$

(D6)

Again after the fourth pulse,

$$M_4^b = M_0\left(1 - e^{-\frac{TR}{T1}}\right) + M_3^b \cos\ \theta e^{-\frac{TR}{T1}}$$

(D7)

Substutiting Equations (D6) and (D5) into (D7) gives,

$$M_4^b = M_0(1 - e^{-\frac{TR}{T1}}) + \left[M_0(1 - e^{-\frac{TR}{T1}}) + \left[M_0(1 - e^{-\frac{TR}{T1}}) + M_0 \cos\theta\, e^{-\frac{TR}{T1}}\right]\cos\theta\, e^{-\frac{TR}{T1}}\right]\cos\theta\, e^{-\frac{TR}{T1}}$$

(D8)

This rearranged is,

$$M_4^b = M_0(1 - e^{-\frac{TR}{T1}}) + M_0(1 - e^{-\frac{TR}{T1}})\cos\ \theta e^{-\frac{TR}{T1}} + M_0(1 - e^{-\frac{TR}{T1}})\cos^2\ \theta e^{-\frac{2TR}{T1}} + M_0 \cos^3 e^{-\frac{4TR}{T1}}$$

Rearranging again gives,

$$M_4^b = M_0(1 - e^{-\frac{TR}{T1}})\left(1 + \cos\theta\, e^{-\frac{TR}{T1}} + \cos^2\theta\, e^{-\frac{2TR}{T1}}\right) + M_0 \cos^3\theta\, e^{-\frac{4TR}{T1}} \qquad \text{(D9)}$$

Extending this in general, the magnitization before the n+1st pulse, where n is a summing integer, becomes,

$$M_{n+1}^b = M_0\left(1 - e^{-\frac{TR}{T1}}\right)\sum_{i=0}^{n+1}\left(\cos\theta\, e^{-\frac{TR}{T1}}\right)^i + M_0\left(\cos\theta\, e^{-\frac{TR}{T1}}\right)^n \qquad \text{(D10)}$$

Where i is a summing integer. A closed form for this is given by the geometric series equation,[D3]

$$\sum_{k=N_1}^{N_2} a^k = \frac{a^{N_1} - a^{N_2+1}}{1-a}, \qquad N_2 \geq N_1, \quad a > 1$$

(D11)

Applying this to the summation in Equation (D10) gives,

$$M_{n+1}^b = M_0\left(1 - e^{-\frac{TR}{T1}}\right)\frac{1-\left(\cos\theta\, e^{-\frac{TR}{T1}}\right)^n}{1-\cos\theta\, e^{-\frac{TR}{T1}}} + M_0\left(\cos\theta\, e^{-\frac{TR}{T1}}\right)^n \quad \text{D12)}$$

For large values of n, the second term of this equation can be neglected as

$(\cos\theta\, e^{-\frac{TR}{T1}})^n$ approaches zero, and we have,

$$M_{n+1}^{b} = M_0\left(1 - e^{-\frac{TR}{T1}}\right)\frac{1}{1-\cos\theta\, e^{-\frac{TR}{T1}}} \tag{D13}$$

Thus we have the magnitude of the magnitization vector, which is tilted at θ degrees. The magnitization projected into the x-y plane, M_{xy}^{0} is proportional to the sin θ, and it will decay with a time constant T2 up to the time it is measured TE. So from Equation (D13) we have

$$M_{xy}^{0} = M_0\left(1 - e^{-\frac{TR}{T1}}\right)\frac{\sin\theta\, e^{-\frac{TE}{T2*}}}{1-\cos\theta\, e^{-\frac{TR}{T1}}} \tag{D14}$$

Where $T2^*$ includes modifications of T2 due to equipment induced factors.
A plot of Equation (D14) for various values of TR << T1 shows a considerable measurable magnitization, thus yielding faster scans.

REFERENCES APPENDIX D

D1. Wright, Steven, “Nuclear Magnetic Resonance and Magnetic Resonance Imaging”, Chapter 16 in *Introduction to Biomedical Engineering* Ed. By J. Enderle, S. Blanchard & J. Bronzino. San Diego: Academic Press, p. 801 (2000).

D2 Reeder, Scott R., *Development of High Speed, High Resollution Magnetic Resonance Imaging and Tagging Techniques* Baltimore, MD: Johns Hopkins University, MS Thesis pp31-34 (1993). Accessed on the WEB, October 2004 at: Http://www.mri.jhu.edu/~sreeder/pdf_papers/mse_t~va.pdf

D3 Oppenheim, Alan V. & Ronald W. Shafer. *Discrete Time Signal Processing.* Englewood, NJ: Prentice Hall (1982).

Appendix E Fan Beam Projection

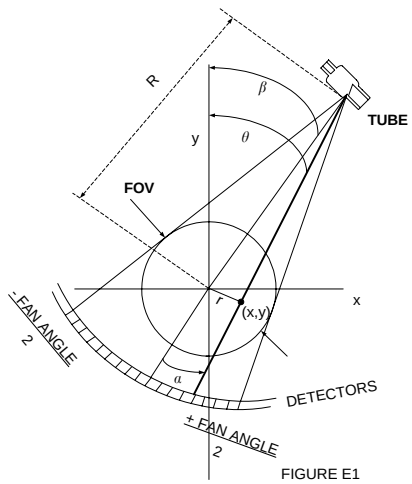

FIGURE E1

Given, the constructed, empirically measured Fourier Transform, P(k,θ), we can form the 2D inverse Fourier Transform (FT) as,

$$f(x,y) = \int_0^{\pi} \int_{-\infty}^{\infty} P(k,\theta)|k| e^{i2\pi k(x\ \cos\theta + y\ \sin\theta)} dk\ d\theta \qquad \text{(E1)}$$

The Fan Beam Projection formula given in Equation (E1) is modified to be calculable from easily measurable machine parameters shown in Figure E1: α, the angle between the center line of the field of view FOV and the ray from the tube to a particular detector; β, the angle between the center line of the FOV and the y-axis; and R, the distance from the tube to the center of the FOV. The derivation of this modified formula is as follows:

We break Equation (E1) into two parts as [E1]

$$f(x,y) = \int_0^{\pi} p^*(r,\theta)\ d\theta \qquad \text{(E2)}$$

where

$$r = x\cos\theta + y\sin\theta \qquad \text{(E3)}$$

And where

$$p^*(r,\theta) = \int_{-\infty}^{\infty} P(k,\theta)|k| e^{i2\pi k(r)} dk \qquad \text{(E4)}$$

Equation (E4) is the one dimensional transform of the product of two FTs; P(k,θ) and |k|.

By the projection theorem, [E2]

$$P(k,\theta) = \int_{-\infty}^{\infty} p(r,\theta) e^{-2\pi i k r} dr \qquad \text{(E5)}$$

This says P(k,θ) is the one dimensional FT of p(r,θ). Thus, p(r,θ) is the inverse FT of P(k,θ). We define q(r) as

$$q(r) = \int_{-\infty}^{\infty} |k| e^{i2\pi k r} dk \qquad \text{(E6)}$$

q(r) is the inverse FT of $|k|$.
The Convolution Theorem states[E3]

$$\Im^{-1}[\Im_1\{p(r,\theta\} \bullet |k|] = p(r,\theta) \divideontimes \Im^{-1}\{|k|\} \qquad \text{(E7)}$$

Which reads in words: The inverse Fourier Transform of the Fourier Transform of p times the magnitude of k equals the inverse Fourier Transform of the Fourier Transform of p convoluted with the inverse Fourier Transform of the magnitude of k.
Thus we may form

$$p^*(r,\theta) = \int_{-\infty}^{\infty} p(r',\theta)\, q(r - r')\, dr' \qquad \text{(E8)}$$

where r is given by Equation (E3).
Substitution of (E8) into Equation (E2) gives

$$f(x,y) = \int_{0}^{\pi} \int_{-\infty}^{\infty} p(r',\theta)\, q(r - r')\, dr' d\theta \qquad \text{(E9)}$$

Now we change the limits on θ to be from 0 to 2π and take half the integral. Then we limit the integration on r′ to the field of view (FOV). So Equation (E9) becomes

$$f(x,y) = \frac{1}{2} \int_{0}^{2\pi} \int_{\frac{-FOV}{2}}^{\frac{FOV}{2}} p(r',\theta)\, q(x \cos\theta + y \sin\theta - r')\, dr' d\theta \qquad \text{(E10)}$$

Also, from Figure E1, we observe new coordinates

$\theta = \alpha + \beta$

And $r = R \sin \alpha$ (E11)

Substituting this into Equation (E10) gives

$$f(x,y) = \frac{1}{2} \int_{0}^{2\pi} \int_{\frac{-Fan\ angle}{2}}^{\frac{Fan\ angle}{2}} p(\alpha,\beta)\, q(x \cos(\alpha+\beta) + y \sin(\alpha+\beta) - R \sin\alpha)\, R\cos\alpha\, d\alpha\, d\beta \qquad \text{(E12)}$$

Where q is given by Equation (E6). Finite limits are set on Equation (E6) by the Ram-Lax filter,[E4]

$$k_{MAX} = \frac{1}{\triangle s}$$

Equation (E6) becomes

$$q(r) = \int_{-k_{MAX}}^{k_{MAX}} |k| e^{i2\pi kr} dk \qquad \text{(E13)}$$

where r = x cos θ + y sin θ. Calculation of Equations (E13) and (E12) produce f(x,y) which can be coded in a gray scale to make the image.[E5]

References Appendix E

E1. Swindell, W., & S. Webb. "X-ray Transmission Computed Tomography, Chapter 4" in *The Physics of Medical Imaging* ed. By S. Webb, Philadelphia: Institute of Physics Publishing (1988) p. 113.

E2. Suetens, Paul. *Fundamentals of Medical Imaging* Cambridge: Cambridge University Press (2002) pp 75-76.

E3. Macovski, A., *Medical Imaging Systems,* Englewood Cliffs, NJ: Prentice Hall (1983) p 127.

E4. Ramachandran, G.N., & Lakshminarayanan, A. V., (1971) *Proc. National Academy of Science, USA, vol 68, pp 2236-2240.*

E5. Suetens, *op cit* p80.

ABOUT THE AUTHOR

Richard Aston has published three text books, two in medical instrumentation: *Principles of Biomedical Instrumentation and Measurement* published by Merrill Publishing Company in 1990, and *Medical Instrumentation for Nurses and Allied Health-Care Professionals* with Katherine K. Brown, published by Jones and Bartlett, Inc. in 1994. He taught medical instrumentation in several colleges over the past 20 years, most recently at East Tennessee State University in the biomedical engineering technology program for 10 years. He taught a medical imaging equipment course to undergraduate seniors about ten times. He was granted a Ph.D. by The Ohio State University in 1969, and is a registered professional engineer (P.E.) in Pennsylvania.

The book *Principles of Biomedical Instrumentation and Measurement* by Richard Aston is available from Prentice Hall at their web site:

Http://vig.prenhall.com/catalog/academic/product/0,1144,0675209439,00.html

ISBN: 0-675-20943-9